“Flow around faults of the West Netherlands Basin in the context of geothermal energy”

An MSc thesis by Natalia Allagianni[1,2]

Supervisors
Prof. Hans de Bresser[1]
Dr. Frans Aben[2]
Stefan Peeters MSc[2]

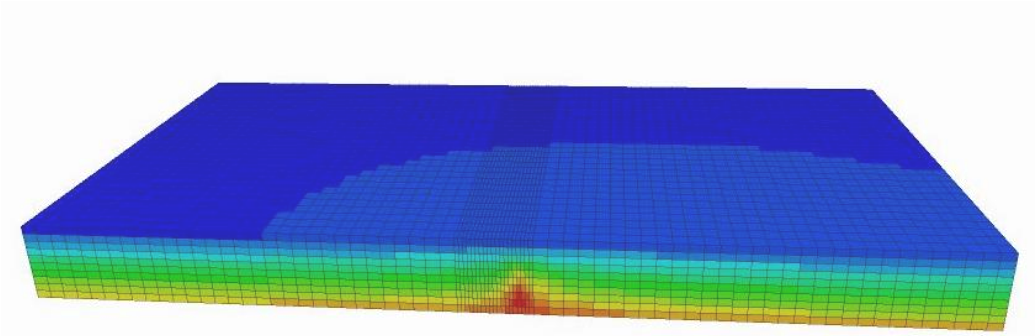

AUGUST 2024

[1]Utrecht University; Heidelberglaan 8, 3584 CS Utrecht, The Netherlands

[2]TNO; Princetonlaan 6, 3584 CB Utrecht, The Netherlands

Abstract

Over the past fifteen years, geothermal energy development has increased in the West Netherlands Basin (WNB), both onshore and offshore in the southwest of The Netherlands. Main target reservoirs here for geothermal energy are the Delft and Alblasserdam Members of the siliciclastic Nieuwerkerk Formation. The structural geology of the WNB is complex as it is characterized by extensive, generally NW-SE oriented fault systems, which formed during various deformation phases in the Mesozoic and Cenozoic eras, resulting in intra-basin fault networks like grabens, half-grabens, and pop-up structures.

Understanding these fault systems is crucial for the safe and profitable extraction of geothermal energy, as these faults have an affect both on fluid flow and potential seismic activity. Hence, a proper understanding of a fault's geometry, displacement, kinematic history and rock properties is of key importance.

This study aims to assess how faults with varying properties and offsetting the Nieuwerkerk Fm., affect fluid flow and stress distribution in the WNB. This was done by firstly performing a 3D kinematic analysis of faults for an area of interest within the WNB using 3D seismic interpretation. Subsequently, the shale gauge ratio (SGR%) (Yielding, 2002) and damage zone width was calculated for a specific fault of interest by using 3D seismic, and well log data from nearby wells. Lastly, numerical models were created by using FLAC3D-ToughREACT software (Taron et al., 2009), to simulate cold fluid injection under different fault's properties conditions, for a two-year period. By exploring various scenarios of shale content and damage zone width, the impact of different fault properties on fluid flow and temperature and stress distributions is assessed. Amongst others, it is found that a high but realistic shale gouge ratio results significant pressure compartmentalization. A permeability-decreasing damage zone has similar effects to a high shale gouge ratio and burdens the impact of SGR%, when high SGR% and decreased permeability damage zone coexist. However, a permeability-increasing damage zone alleviates the effect of a high shale gouge ratio. This underlines the relevance of understanding permeability evolution in fault damage zones. Time evolution analysis reveals the temperature changes have higher influence on the stress ratio changes, however, while pore pressure changes depend on temperature changes, the increase of the pore pressure by the convection circulation inside the reservoir is the key to the stress distribution along the fault.

In conclusion, this study highlights the importance of blending geological insights with advanced modelling to manage risks like induced seismicity and improve reservoir performance in geothermal projects.

Table of Contents

1 Introduction

Over the last 15 years, there has been a significant surge in geothermal energy development in the West Netherlands Basin (WNB), situated both onshore and offshore in the southwestern region of The Netherlands (Willems et al. 2020). Within this basin, potential geothermal reservoirs are found in the Upper Jurassic to Lower Cretaceous Nieuwerkerk formation, specifically in the Alblasserdam Member (Alblasserdam Mb.) and the Delft Sandstone Member (DSSM), which consist of shallow marine and terrestrial deposits.

The WNB is bordered by extensive, generally NW-SE oriented fault systems, which were formed by both normal, reverse and strike-slip movements during several Mesozoic and Cenozoic deformation phases. This has led to a complex network of intra-basinal fault systems, forming partially inverted grabens, half-grabens, and pop-up structures.

Understanding the configuration and movements of these intricate fault systems, along with their rock properties related to physics and fluid flow, is vital for ensuring the safe and economically feasible extraction of geothermal energy.

According to Buijze et al. (2019), different types of geothermal reservoirs and their host rocks have varying susceptibilities to induced seismicity. For instance, porous and permeable sedimentary rocks may respond differently to geothermal activities compared to crystalline or volcanic rocks. The characteristics of faults in the area, such as their orientation, stress state, and mechanical properties, play a crucial role in determining the likelihood and severity of induced seismic events. However, faults that are critically stressed or have a history of seismic activity may be more prone to reactivation. The local geological setting, including the stress regime, rock properties, and existing fault systems, significantly affects the risk of induced seismicity. These parameters can be calculated in models. Faulting in clean sandstones typically produces open cataclasites conducive to fluid flow (Yielding, 2002). Conversely, faulting through extensive clay beds often leads to clay smearing along the fault plane, potentially impeding fluid movement (Yielding, 2002).

In models at the reservoir scale, faults that are evident in seismic data are typically represented as 2D interfaces. These interfaces may function as obstacles to fault-normal fluid flow when clay smearing is present or remain open if they juxtapose clean sandstone (Yielding, 2002). However, real-world observations indicate that fault zones are intricate 3D structures characterized by one or more fault cores

(where the majority of slip occurs) surrounded by extensive zones of damaged host rock (Savage & Brodsky, 2011). These zones may contain secondary faults, fractures, and compaction bands. Due to these structural complexities, the damage zones may possess distinct properties and anisotropy compared to the intact host rock, consequently influencing fluid flow. This becomes particularly crucial in the context of geothermal energy, where fluid flow plays a significant role in cooling the host rock and potential stress accumulation on faults. Therefore, it is advisable to integrate these damage zones into reservoir-scale models.

The objective of this research project is to assess the impact of varying amounts of shale within the fault core and varying damage zone architectures on fluid flow during geothermal activity and stress build-up for a fault of interest (FOI) within the WNB. To achieve this goal, the following research questions are posed: What is the geological history and fault structure in the West Netherlands Basin? What the general kinematics of faults within the AOI within the WNB and can we estimate for a single key fault of interest, it's permeabilities by applying general scaling laws derived from literature? And ultimately: How do the faults in the WNB affect fluid flow during geothermal activity?

The first research question aims to enhance comprehension regarding the distribution of faults and their geological and geometric characteristics (e.g., fault displacement, arrangement of rock types) within the WNB. This geological data, derived from 3D seismic interpretation and well log data in Petrel, will facilitate understanding by: i) Establishing the kinematic and tectonic history of the WNB and calculate the offset and fault's geometrical characteristics, alongside established scaling laws for damage zone width (e.g., Savage & Brodsky, 2011), as also containing in the model realistic rock properties from well log data and structures from the seismic data analysis. This will delineate parameters like the width of damage zone of the fault of interest (FOI) in the WNB and the geometry of the model. ii) Recognizing how the host rock's composition (sand/clay ratio) influences fault's permeability.

The second research question aims to elucidate how fluid flow is affected by fault core permeability (in varying percentages) and damage zones, compared to flow scenarios without such damage zones. This will involve employing a generalized fault zone model in FLAC3D-ToughREACT, a thermo-hydro-mechanically coupled finite difference modelling software (Taron et al., 2009). The simulation concerns cold-water injection scenario for geothermal doublet. The exploration will encompass various damage zone geometries and properties representative of the WNB, derived from the 3D seismic study and existing data. This model is representative for relatively small faults within the area of interest.

In order to reach the main scope of this thesis, changes on different model scenarios of two basic properties on the setup and geometry of the model are going to be presented. These two properties are the fault core permeability and the presence or absence of a damage zone (geometry of the model) and its underlying properties. The main purpose of this study is the influence of the fault core permeability and the damage zone width. For this reason, all the scenarios will be differed from each other on their shale gouge ratio percentage (SGR%) as fault core permeability and the presence or absence of the damage zone (as changes in the scenarios' properties), based on the measured seismic data. The analysis following the results of the geological interpretation shall be the main link between the geology and the modelling part.

A schematic that summarizes the study conducted in this thesis is shown in Figure 1. This thesis analyzes the geological tectonic evolution, stratigraphy, and geothermal potential of the WNB. It covers fault structures, seismic interpretation methods, well log data (NLOG), and SGR percentage calculations (Yielding, 2002). The reader is introduced to FLAC3D-ToughREACT simulations (Taron et al., 2009), including model geometry, injection scenarios, and properties. Moreover, the link between geology and modelling will be presented in the results. Results include time-thickness maps and links between geology and modelling, leading to SGR% values, permeability, and damage zone geometry. The FLAC3D-ToughREACT model results are discussed in terms of temperature, pore pressure, and stress distribution along the fault of interest (FOI). Lastly, the thesis concludes with a discussion of results and conclusions.

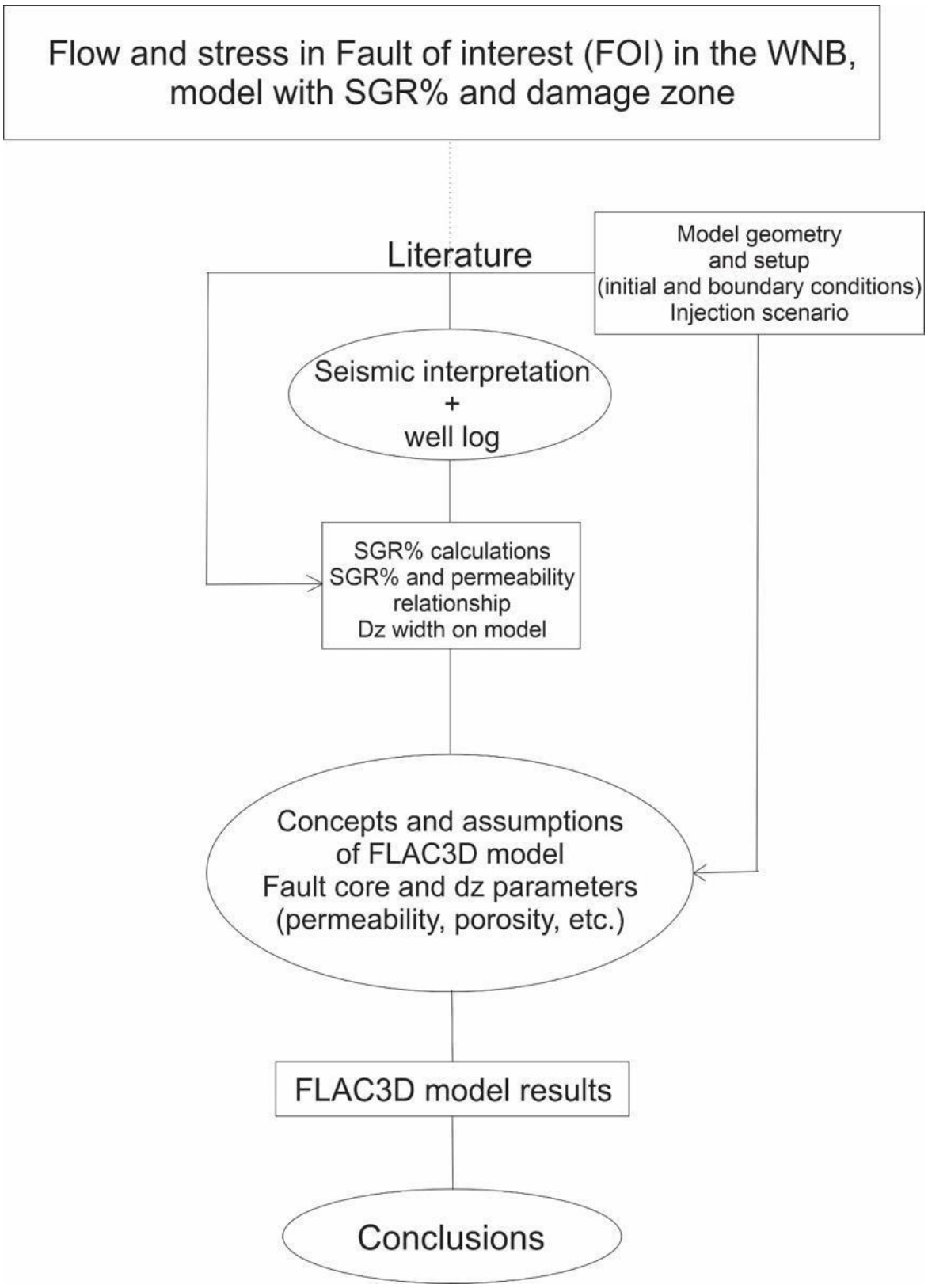

Figure 1. Flow chart of the current study.

2 Background Information

In this chapter, some general background information will be given regarding the geology of the area of interest, as part of the West Netherlands basin. A general description of the tectonic evolution of the area (2.1.1) will be presented. The stratigraphy of the West Netherlands basin (2.2) will follow with a focus on the Alblasserdam Mb. (2.2.1), DSSM (2.2.2.) and the Rodenrijs Claystone Member (2.2.3), as the main stratigraphic Members of interest, all of them part of Nieuwerkerk Formation. A brief history of the subsurface activities of the WNB will be described (2.3.) and additional information will be provided regarding the stratigraphy of the Nieuwerkerk Fm., including information about the target geothermal well (2.4.). Lastly, background information about the fault structure and scaling will be given (2.5.).

2.1 Tectonic history of the West Netherlands Basin

The WNB is a basin in the southwestern part of the Netherlands, stretching northwest to southeast and extending into the southern Dutch North Sea (Duin et al., 2006; Kombrink et al., 2012; Willems et al. 2020). It is bordered by the London–Brabant High to the southwest and the Zandvoort Ridge to the northeast (Fig. 2). The basin's formation began with extensional movements in the Middle Jurassic period, resulting in the creation of parallel half-grabens, as described by Bodenhausen & Ott (1981), Den Hartog Jager (1996) and Racero-Baena & Drake (1996), which were filled with terrestrial sediments. These sediments originated from the London-Brabant Massif to the south and the Roer Valley Graben to the southeast (Den Hartog Jager, 1996; Herngreen & Wong, 2007).

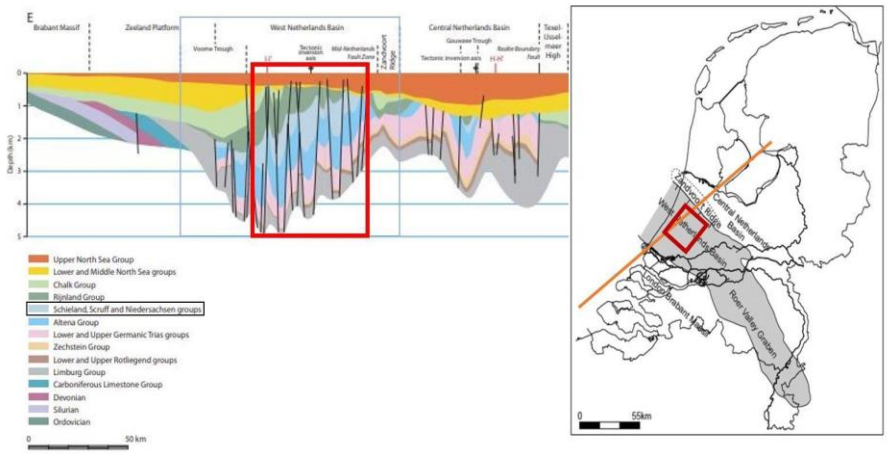

Figure 2. a) Cross – section from the study of Duin et al. (2006) with the tectonic structures and stratigraphic profile including the West Netherlands Basin. The red box highlights the location of the WNB. The light blue interval within the WNB marks the position of the Schieland Group in the cross – section, which includes the Nieuwerkerk Fm. b) Map with the West Netherlands Basin which is located within a geological framework bordered to the south by the London–Brabant Massif and to the north by the Zandvoort Ridge and the Central Netherlands Basin (adapted from Vondrak et al., 2018). The red box highlights the study area, which focuses on the main inversion axis in the WNB.

The entire period from Jurassic to lowermost Lower Cretaceous is referred to as the syn-rift phase. Unconformities within the Upper Jurassic to Lower Cretaceous interval suggest several tectonic events during this period (Devault & Jeremiah, 2002). Around the Hauterivian period, the basin underwent a phase of post-rift thermal sag, synchronized with a gradual rise in relative sea level (Duin et al., 2006). Consequently, the Upper Cretaceous sediment layers shows a relatively uniform thickness, gradually thinning toward the basin margins (Den Hartog Jager, 1996; Vondrak et al., 2018). During the Ryazanian period, the paleo-coastline was positioned at the northwest boundary of the West Netherlands Basin (WNB) but had shifted by the Hauterivian period to the northwest boundary of the Roer Valley Graben. This migration led to a gradual covering of the terrestrial syn – tectonic deposits with marine sediments (Den Hartog Jager, 1996; Herngreen and Wong, 2007; Jeremiah et al., 2010; Vejbbæk et al., 2010).

As part of the Late Cretaceous Laramide compressional phase, during the Palaeocene, a new phase of tectonic activity significantly altered the basin's structural configuration (Van Wijhe, 1987). Many of the Jurassic normal faults were reactivated, leading to reverse faulting and the formation of pop-up structures during this period of Alpine inversion. Additionally, the inversion and associated uplift led to significant erosion of Jurassic and Cretaceous sediments (Racero-Baena & Drake, 1996; Herngreen & Wong, 2007; Jeremiah et al., 2010).

The axes of maximum inversion are determined from the regional distribution and thickness of the Late Cretaceous (which in stratigraphic sequence corresponds to Chalk Group). The tectonic inversion phases appear to have been active simultaneously in most basins (Duin et al., 2006). Inversion of these basins seems to have occurred concurrently during the Subhercynian (Santonian-Campanian), Laramide (Paleocene), and Pyrenean (Eocene) phases of intraplate compression (Duin et al., 2006).

The Zandvoort Ridge, where both Jurassic and Cretaceous strata have been significantly eroded, is where uplift and erosion were most severe (Kombrink et al., 2012). The inversion altered the strata's geothermal potential by changing their current burial depth and, consequently, temperature. In addition, it produced the pop-up and horst structures that hydrocarbon wells were aiming for (Kombrink et al., 2012).

The basins in the southern offshore and onshore Netherlands during the Late Jurassic are governed by NW-SE trending fault systems, with WNW-ESE and NNW-SSE trending faults playing a subsidiary role. In the West Netherlands Basin, during the Late Jurassic period were deposited the Schieland, Scruff, and Niedersachsen Groups, with the Delft Sandstone and Alblasserdam Members to be contained in the Schieland Group.

Due to Late Cretaceous inversion, the Rijnland Group (Early Cretaceous) is locally absent or reduced in thickness, especially in the West Netherlands Basin (Duin et al., 2006). The depth maps reported by Duin (2006) indicate that inversion has also occurred in the Roer Valley Graben, Central Netherlands Basin, and Broad Fourteens Basin.

2.2 Stratigraphy of the West Netherlands Basin

The sedimentary deposition from the period of Late Jurassic to Early Cretaceous in the Dutch part of the North Sea basin exhibits a distinct stepped transgression, influenced by both eustatic sea level changes and tectonic activity (Donselaar et al. 2015). This transgression extending from the Central Graben and Sole Pit Basin in the northwest to the Lower Saxony Basin and Roer Valley Graben in the southeast (Van Adrichem Boogaert & Kouwe, 1997; Abbink et al., 2006; Jeremiah et al., 2010; Munsterman, 2012; Bouroullec et al., 2018; Verreussel et al., 2018).

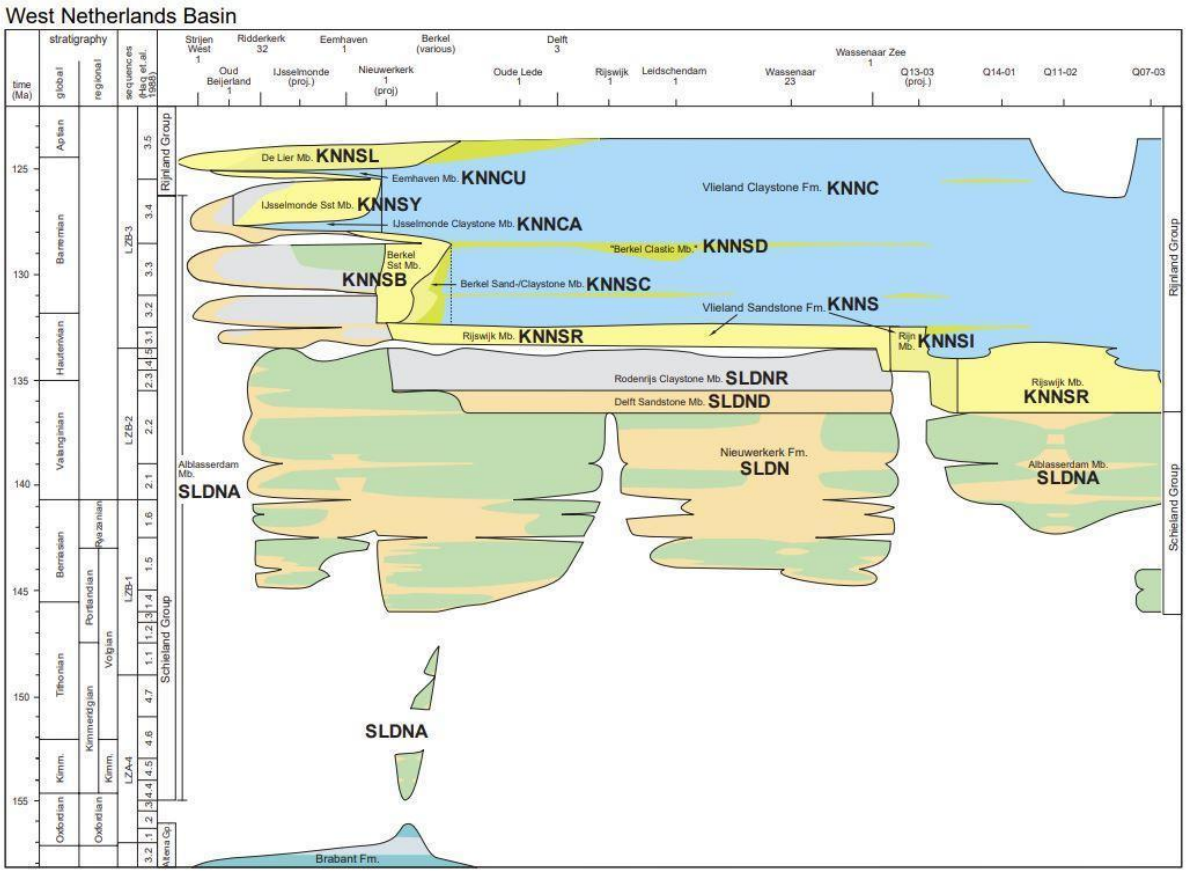

Figure 3. Stratigraphy of Upper Jurassic and Lower Cretaceous in the West Netherlands Basin from Boogaert & Kouwe (1993).

The Upper Jurassic to Lower Cretaceous sediments is classified into Groups, which in term are classified into Formations and lithostratigraphic members. The predominantly terrestrial deposits of the Upper

Jurassic and Lower Cretaceous are part of the Schieland Group. The predominantly marine deposits of the Lower Cretaceous are part of the Rijnland Group.

The Schieland Group includes the Nieuwerkerk Formation (Fig. 3) (Van Adrichem Boogaert & Kouwe, 1997). The Nieuwerkerk Formation is subdivided into three members based on their lithostratigraphy, more specifically, the presence of sandstone, the plentiful supply of coal and the occurrence of marine intercalations at different intervals (Van Adrichem Boogaert & Kouwe, 1997).

The Alblasserdam Member stands as the oldest among these units, distinguished by its characteristics as a syn-rift fluvial interval with a low net-to-gross ratio. It is situated unconformably above the Lower and Middle Jurassic Altena Group in graben fault blocks and the Lower Jurassic Aalburg Formation in some horst blocks (Devault & Jeremiah, 2002), exhibiting a varied gamma-ray (GR) log signature. The Alblasserdam Mb. is described in more detail in paragraph 2.2.1.

In the western and central onshore regions of the WNB (Fig. 4), the Alblasserdam Member is succeeded by the sandstones of the coastal-plain DSSM (Van Adrichem Boogaert and Kouwe, 1993; Donselaar et al. 2015). The DSSM is described in more detail in paragraph 2.2.2.

Typically, the DSSM is followed in a conformable manner within the lagoonal Rodenrijs Claystone, which is rich in organic material (Donselaar et al. 2015). The Rodenrijs Claystone Member is described in more detail in paragraph 2.2.3.

These members predominantly consist of fluvial successions, with a separating clay interval resulting from a marine transgression (Van Adrichem Boogaert and Kouwe 1993, Den Hartog Jager 1996). The primary direction of sediment transport for both the Delft Sandstone and Alblasserdam was from the southeast to the northwest, aligning with the principal fault trend prevalent in the region (Van Adrichem Boogaert and Kouwe 1993, Donselaar, et al. 2015). The individual members of the Nieuwerkerk Fm. will be described in the paragraphs 2.2.1, 2.2.2, and 2.2.3.

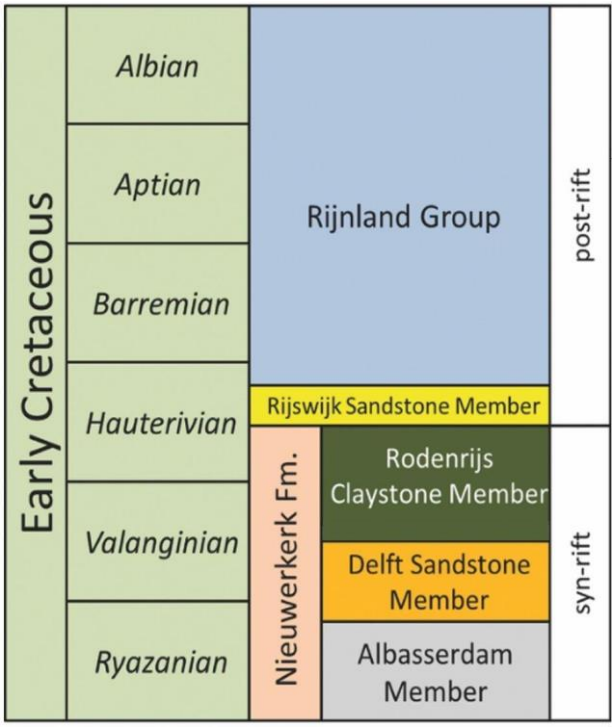

Figure 4. Stratigraphic column for the Early Cretaceous section in the WNB indicating tectonic activity during deposition of the Rijnland Group, the Nieuwerkerk Formation and the main geothermal aquifers in the WNB (Willems et al. 2018).

Interpreting the lithostratigraphy of a sandstone package below the Rodenrijs Claystone Member within the Delft or Alblasserdam Members without precise biostratigraphic control poses considerable challenges. Detailed seismic analysis suggests that, in some areas, a reflector near the base of the DSSM exhibits an angular truncation configuration (Verreussel & Peeters, 2024). Unconformities within the intra-Nieuwerkerk Formation have been observed (e.g., Devault & Jeremiah, 2002), but their validation through precise seismic-to-well correlations is still awaited.

The marine sediments of the Rijnland Group lie directly above the Nieuwerkerk Formation (Donselaar et al., 2015). The contact within the basin varies by location, exhibiting either a conformable relationship or a subtle angular unconformity characterized by erosional truncation. Sediments were laid down from the Late Ryazanian period in the northwestern part of the WNB until the Aptian period. The foundation consists of either claystones from the Vlieland Claystone Formation or sandstones from the Vlieland Sandstone Formation (Vlieland Sandstone Fm, Den Hartog Jager, 1996). Van Adrichem Boogaert & Kouwe (1997) identified several distinct members within the Vlieland Sandstone Fm that are specific to the WNB, which were formed as basal transgressive sands, coastal barrier complexes that prograded, or offshore shoal sands (Fig. 3). To the southeast, these marine sandstone members transition into continental claystone deposits known as the Alblasserdam Member (Van Adrichem Boogaert and Kouwe 1993, Den

Hartog Jager 1996). These marine and terrestrial deposits are lateral equivalents characterized by rapid changes in facies. The lack of sufficient well control and geological data leads to uncertainty regarding the lateral extent, thickness, and consequently the geothermal potential of the sandstone-dominated units.

Among the marine sandstone members of the Rijnland Group, the Rijswijk Member and the Berkel Sandstone Member are significant geothermal aquifer targets in the West Netherlands Basin (WNB) (e.g., Vis et al., 2010). The Rijswijk Member is primarily made up of basal transgressive and bioturbated sandstones, while the Berkel Sandstone Member was formed by a regressive coastal-barrier system advancing westward and northwestward (Racero-Baena & Drake, 1996). Today, 11 operational doublets extract heat from the DSSM, making it the primary geothermal target in the WNB.

2.2.1 Alblasserdam Member

In more detail, the Alblasserdam Member primarily comprises channel and fluvial plain deposits, with sand concentrations within the channels and crevasse splays (Van Adrichem Boogaert and Kouwe 1993, Donselaar et al., 2015). Floodplains hosted deposits of clays and peatbeds (Donselaar et al., 2015). The deposition of the Alblasserdam Member occurred during the Ryazanian (Upper Berriasian) and Valanginian stages, approximately 143-135 million years ago, coinciding with the main period of active rifting in the study area (Ziegler 1990, Van Adrichem Boogaert and Kouwe 1993). Consequently, notable differences in sediment thickness and grain size emerged, with the thickest and coarsest deposits primarily accumulating in the hanging wall of the subsiding fault blocks, where most channels were located (Den Hartog Jager 1996; Donselaar et al., 2015).

Biostratigraphic data, dominated by sporomorph-based continental assemblages, corroborate this understanding (DeVault and Jeremiah, 2002). While marine incursions are rare within the Alblasserdam Member, they are occasionally found in the northern part of the basin. The fluvial succession typically encompasses dark-grey to light-grey, red, and alternations of claystones, siltstones and fine to medium-grained sandstones with bed thicknesses ranging up to a few meters, and massive, thick-bedded, coarse-grained sandstones. Grey claystone intervals are associated with coal and lignite beds. Dispersed lignitic matter, siderite spherulites, and concretions are common. The sandstone geometry exhibits sheets, isolated, or stacked channels (Van Adrichem Boogaert and Kouwe, 1993). Den Hartog Jager (1996) suggested a braided-channel type based on high sandstone/shale ratios. Overbank settings within the Alblasserdam Member commonly feature red beds but lack coal. The succession is viewed as fluvial-plain deposits, where sandstone is mainly found in channels and crevasse splays, while deposits outside these

channels show different characteristics, such as swamps and soils which were developed on the floodplains.

The Alblasserdam Member lies unconformably above Middle Jurassic shallow-marine limestones (Brabant Formation) and shelf mudstones (Werkendam Formation). In some horst blocks, these formations are completely cut off, with the Alblasserdam Member sitting directly on top of the Lower Jurassic Aalburg Formation. (DeVault and Jeremiah, 2002).

2.2.2 Delft Sandstone Member

The Delft Sandstone Member (DSSM) representing a fluvial succession formed during and following a significant Early Cretaceous rifting phase within the WNB and serves as the focal point for a technology demonstration project exploring deep geothermal energy production (Donselaar et al., 2015). The rifting activity occurred intermittently from the Kimmeridgian (155 Ma) to the Barremian (130 Ma), characterized by multiple short-duration pulses. During this phase, the basin was actively filled with fluvial sediments in sync with tectonic movement. As the Hauterivian period (135 Ma) approached, the intensity of the active rifting declined, leading the basin into a post-rift sag phase (Donselaar et al., 2015). This transition facilitated marine transgressions, marking the deposition of most post-Hauterivian sediments within a marine setting (Donselaar et al., 2015). The basin continued its gradual subsidence until the onset of the Late Cretaceous Laramide compressional phase, initiating a period of inversion and uplift (Van Wijhe, 1987; Den Hartog Jager, 1996). Seismic data illustrates significant fault zones exhibiting reverse offsets, signaling the reactivation of older basin-bounding faults. This phase of uplift and compression, such as observed in structures like the pop-up formation housing the Pijnacker oilfield, contributed to the formation of many oil-bearing structures (Racero Baena and Drake, 1996).

The DSSM is divided from the Alblasserdam Member by an interval of shale, indicating a sequence boundary resulted from a marine transgression between these two members (Den Hartog Jager, 1996). Similar to the Alblasserdam Member, the DSSM comprises fluvial deposits. It was deposited during the late Valanginian stage (Den Hartog Jager 1996) and consists of sand that ranges from fine to coarse-grained, including gravelly sands, which indicate layered distributary channel systems in a lower coastal plain environment (Van Adrichem Boogaert and Kouwe 1993). Importantly, the DSSM typically has a higher proportion of coarser sand and less clay compared to the Alblasserdam Member, suggesting a more energetic depositional environment characterized by higher sedimentation velocities (Szklarz et al., 2022).

The sequence of lithofacies is mainly influenced by the balance between the rate of accommodation growth and the rate of sediment deposition during the synsedimentary tectonic movement along faults that separated the areas southwest of the Delft High and northeast of the Pijnacker High from the low area (Vrijenban Syncline) (Fig. 5) between the highs (Donselaar et al., 2015). Deposition of DSSM was controlled by differential movement along these faults in combination with a rising sea level, i.e., a high rate of accommodation increases which favoured the deposition of loosely-stacked, fluvial sandstone bodies with well-preserved fine-grained tops embedded in floodplain fines (Donselaar et al., 2015). This setting implies low connectivity of the fluvial sandstone bodies (Donselaar et al., 2015).

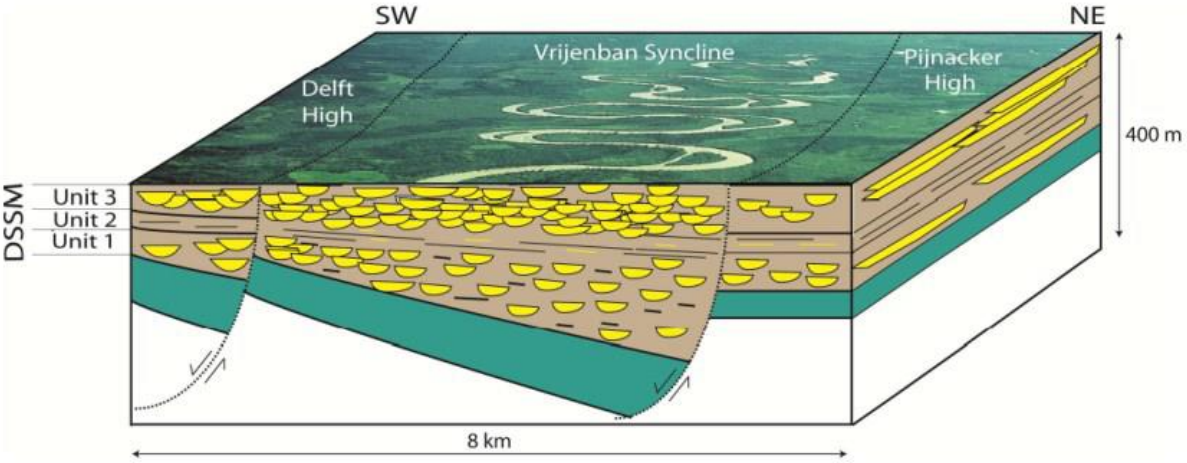

Figure 5. Depositional model for the DSSM in the study area based on analyses of well-logs, cuttings, cores, and on seismic interpretation of fault-conditioned thickness differentiation (Donselaar et al., 2015).

2.2.3 Rodenrijs Claystone Member

The Rodenrijs Claystone Member is composed of grey lignitic claystone, siltstone and sandstone, characterized by layered or distorted bedding along with lignite or coal layers that hold well-preserved plant fossils (Van Adrichem Bogaert and Kouwe, 1993). In some instances, mollusc shells can be found locally, and siderite spherulites and concretions are common occurrences (Donselaar et al., 2015). Fundamental information from the Rotterdam region indicates a sequence of fining-upward deposits that evolve from layered, cross-bedded fluvial channels' sandstone to flood-plain mudstone, occasionally with crevasse-splay deposits (Donselaar et al., 2015). The fining-upward sequence is often capped by coal or thin lacustrine strata. As the relative sea level continued to rise, lagoonal deposits formed (Donselaar et al., 2015). The geological records also indicate stacked fluvial channel systems with fining-upward sequences, where bases erode flood-plain deposits. The prevalence of poorly drained flood-plain deposits, crevasse splays, and minor stacked channel deposits suggests a meandering fluvial system (Den

Hartog Jager, 1996). Similar to the DSSM, the distribution of the Rodenrijs Claystone Member is limited to the western and central parts of the West Netherlands Basin (Donselaar et al., 2015). Based on sporomorph analysis, the Rodenrijs Claystone Member is dated to the Late Valanginian to Early Hauterivian period (Van Adrichem Boogaert and Kouwe, 1993). An inferred lower-coastal-plain to lagoonal depositional environment is indicated. The proximity to the sea suggests a close association between fining-upward sequences, consisting of stacked channel/overbank deposits, and relative sea level rise (Donselaar et al., 2015).

2.3. History of subsurface activities in the WNB

The West Netherlands Basin (WNB) is a rich area for oil and gas, corresponding to around 80 fields in the past (Willems et al., 2020). The pursuit of oil and gas has yielded an abundance of well and seismic data, with almost the entire WNB to be revealed by 3D – seismic surveys of varying ages, typically available in acceptable quality through public channels (Willems et al., 2020). This data can now be used to support geothermal exploration activities, making the area more appealing due to the availability of the information. The geothermal activities started to give solutions on greenhouses' energy demand and for house heating purposes.

The majority of the subsurface data originates from hydrocarbon fields found on the basin's pop-up and horst features.

Numerous preliminary geothermal studies were conducted from the mid-1990s until today, pinpointing Lower Cretaceous Sandstone beds as the primary geothermal targets in the WNB, leading to the conceptualization of the Delfland geothermal project (Dufour 1984). Presently, there are 12 doublets operational in the Upper Jurassic to Lower Cretaceous layers of the WNB. At first, the focus was on the marine sandstones found in the Vlieland Formation. However, interest soon shifted to the Delft Sandstone Member (DSSM) of the Nieuwerkerk Formation beneath it, owing to its favorable characteristics such as higher temperature, permeability, and thickness (Donselaar et al., 2015; Willems et al., 2017; Vondrak et al., 2018). Recently, exploration efforts have been directed toward the deeper Alblasserdam Member of the Nieuwerkerk Formation, with ongoing efforts aiming for the combined development of both stratigraphic intervals (Kombrink et al., 2012).

The target reservoirs within this study area comprise the Alblasserdam Sandstone Member and the DSSM, which are both part of the Nieuwerkerk Formation. The rock properties of the sandstone and the

claystone on the top of the Delft Sandstone member make this interval suitable for geothermal activities (Fig. 6).

Figure 6. The area of interest of this study lies near the village of Pijnacker, around 8 km southeast of The Hague. Image obtained from the Petrel database. The black box contains the area that was covered in the seismic data interpretation and the red box highlights the geothermal doublet of interest (with the white lines to represent the wells). The yellow line represents the position on the cross – section in later chapter that was analysed more detailed. The star is located in the approximate location of the fault of interest.

The Pijnacker geothermal doublets have their own license (https://www.nlog.nl/datacenter/lic-overview), with two of the geothermal systems, owned by glasshouse farmers, to have been operational since 2010, identified as wells PNA-GT-01 and PNA-GT-02 (Donselaar et al., 2015). Both systems extract water at a temperature of 70°C from the DSSM in the West-Netherlands Basin (WNB). Initial experiences with these systems highlight significant variability in their performance (Donselaar et al., 2015). Each geothermal doublet comprises a production well for hot water and a reinjection well for the cooled-down water. Both wells operate within the same aquifer, where the cooled-down water disperses from the

injection well, eventually returning to the production well. Understanding the reservoir connectivity between these production and injection wells within the aquifer is crucial (Donselaar et al., 2015).

2.4. Geothermal potential of the Nieuwerkerk Formation

The geothermal potential of the Nieuwerkerk Formation relies on factors such as the overall volume of potential reservoir sandstone, sandstone permeability, and the temperature of the formation water in the aquifer (Donselaar et al., 2015). In the wells of the DSSM, the average net sand content (N/G) is around 0.65. According to a contour map based on 3D seismic data (Fig. 7, Donselaar et al., 2015), the depth of the DSSM in the structural low ranges from 2000 m to 2300 m. Temperature readings from bottom-hole measurements in oil and gas wells in the region suggest a geothermal gradient of approximately 3°C/100m, resulting in an estimated temperature range of 65-75 °C for the formation water in the DSSM (Donselaar et al., 2015). This temperature range is suitable for applications in a low-temperature grid-heating network or a glasshouse heating system. The permeability of the aquifer plays a crucial role in determining production and re-injection flow rates (Donselaar et al., 2015). Hydrocarbon appraisal drilling in and around the target area has indicated promising reservoir qualities in the DSSM, characterized by high porosity and permeability (Donselaar et al., 2015). Further insights into spatial and vertical variability were gained from analyses of core samples and cuttings from wells MKP-11 in the Moerkapelle oil field (10 km to the northeast) and well DEL-03. These analyses revealed that the three identified units in the DSSM exhibit distinct porosity and permeability values (Donselaar et al. 2015).

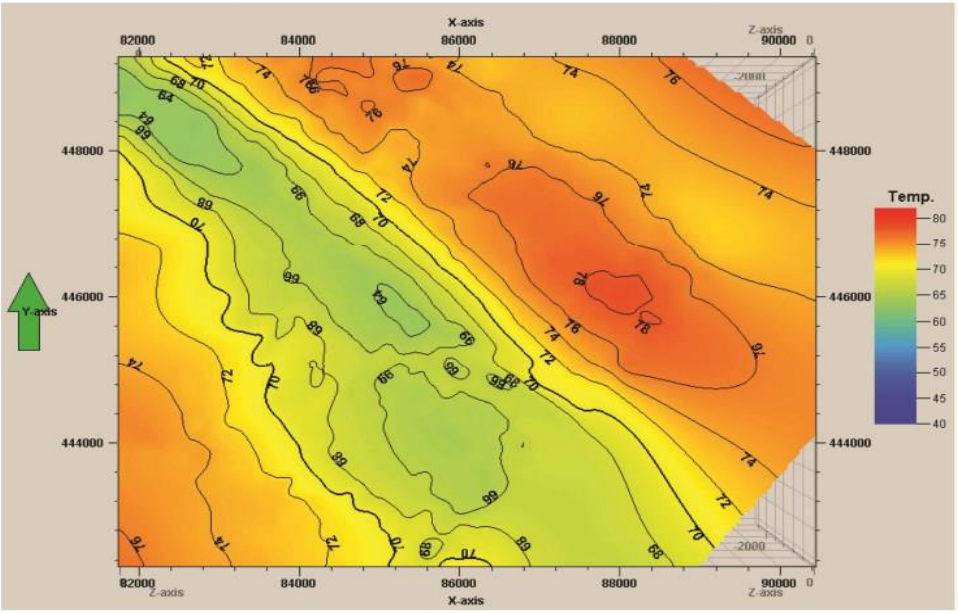

Figure 7. Temperature map of the top DSSM. Temperature in °C. Map constructed from interpreted seismic horizon top DSSM and applying the local thermal gradient of 3.11 °C per 100 m (Donselaar et al. 2015).

2.5. Fault Structure and scaling

In this subsection, literature relevant to generic faults, not specifically those of the WNB, will be reviewed, considering them not only as structures but also by including their effect in mechanical and hydraulic rock properties.

Some fault geometries, especially the damage zone width, can be obtained from scaling relations for the model geometry of the study. The faults' displacement relationship with the distance from the fault is the main relationship that will be used for the scaling, as described by Savage and Brodsky (2011), which in later chapters will link the geology measurements with the setup and geometry of the FLAC3D-ToughREACT model (Taron et al., 2009). The Scaling of the structures will be mentioned too, as these data are not available from the seismic interpretation or the well log due to their lack of high resolution needed for these measurements.

In crustal fault zones, dynamic rupture and fault slip typically occur within a narrow fault core surrounded by a fracture damage zone extending up to hundreds of meters in width (e.g., Savage and Brodsky, 2011). This damage results from a combination of aseismic/quasi-static and coseismic processes. Fractured rock within the damage zone exhibits distinct mechanical and hydraulic properties compared to intact rock, influencing crustal fluid flow, fault mechanics, and earthquake dynamics. Damaged fault rocks have generally different properties than intact rocks, playing a crucial role in fluid migration and mineral precipitation in and around fault zones. Different properties as referred before could be the mechanical properties, such as elastic moduli, cohesion, and yield strength, the hydrological properties such as permeability and porosity, and changes in wave velocity.

Fundamental studies on fault zone damage relied on detailed qualitative structural geology techniques (Crider and Peacock, 2004; Price and Cosgrove, 1990), identifying three broad zones of damage—tip, wall, and interaction damage—based on the type, intensity, and extent of fracturing (Kim et al., 2000, 2003, 2004; Peacock et al., 2016) (Fig. 8, Ostermeijer et al., 2020). Quantitative approaches to damage analysis (Mitchell and Faulkner, 2009; Johri et al., 2014; O'Hara et al., 2017; Savage and Brodsky, 2011; Choi et al., 2016) have aimed to address fundamental questions about the seismic cycle, fault strength, fluid flow properties, and rupture dynamics. These approaches involve simplifying the complex off-fault damage to derive usable mathematical expressions describing its spatial and temporal distribution.

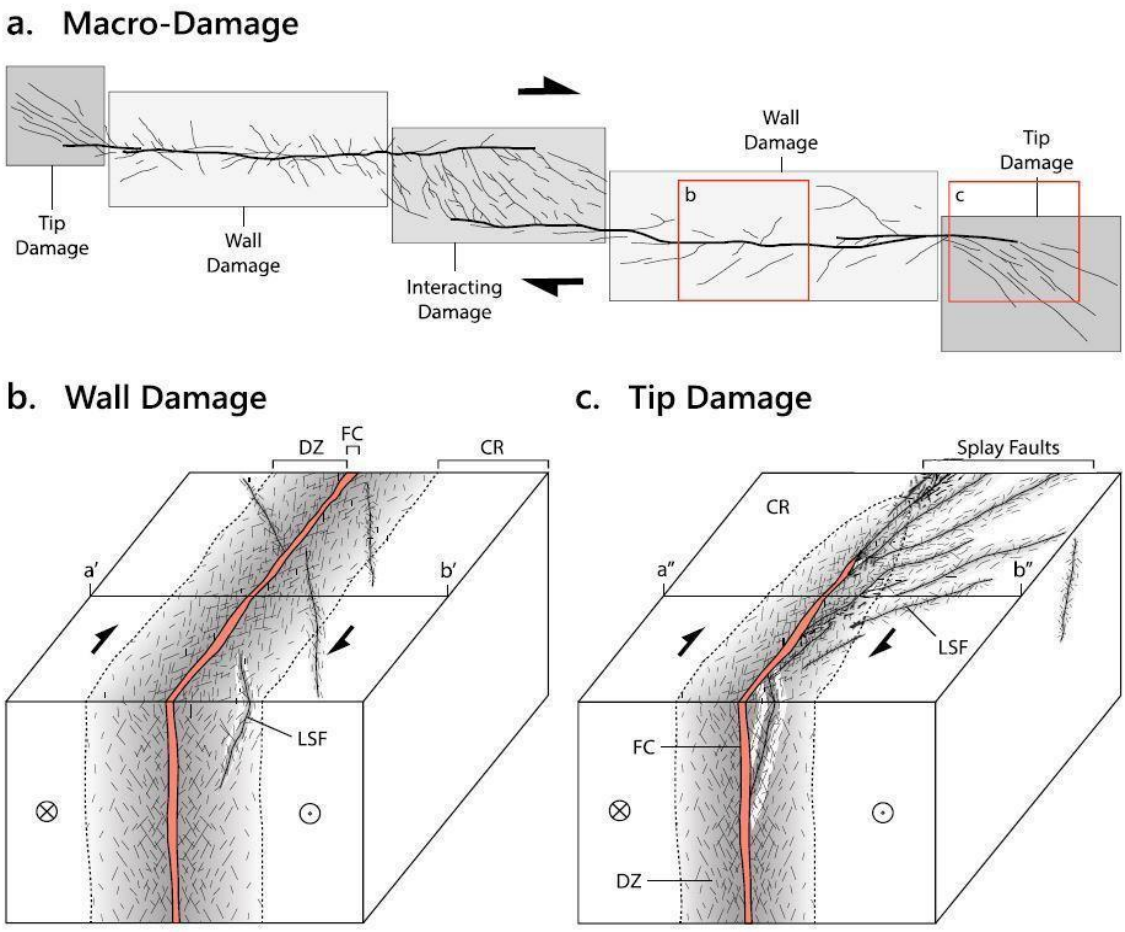

Figure 8. Representation of the damage distribution around the fault as macro-damage (a.) and meso-scale damage (b., c.) around a large fault core. Also, it is visible that the width scaling with displacement is by far more intense closest to the fault (Ostermeijer et al., 2020).

Results from studies measuring micro- and meso-fracture densities on fault perpendicular transects indicate that across-fault 1-D damage profiles can be simplified to fit either an exponential decay model (log-normal linear regression) (Mitchell and Faulkner, 2009) or a power-law decay model (log-log linear regression) (Savage and Brodsky, 2011). In the current study it will be implied as a damage zone, a 1D plane of damage (normal fault) with a decay of damage with distance from the fault, by implementing an inner and outer damage zone.

Structural elements typically found in the process zone include fractures and deformation bands, and previous work has demonstrated that such structures may affect fluid flow in a reservoir (Rotevatn & Fossen, 2011).

Single faults typically exhibit a gradual increase in displacement from the tip-line towards a central point (Fig. 9).

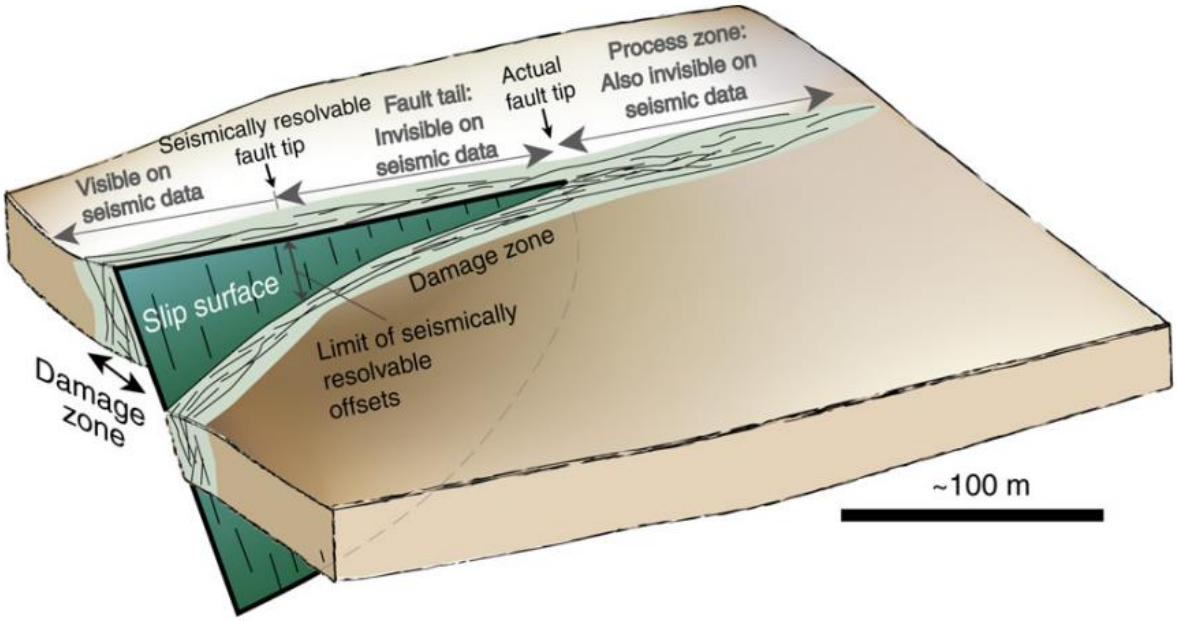

Figure 9. Schematic fault architecture showing the fault plane and the damage- and process zones enveloping the fault (Rotevatn & Fossen, 2011).

Often, faults have contrasting effects on fluid flow, acting as baffles or seals to cross-fault flow while being conduits for along-fault flow (Rotevatn & Fossen, 2011). The properties of faults as barriers/conduits for flow are controlled by several factors. These can be split into two main categories: 1) juxtaposition and 2) the properties of the fault itself. Juxtaposition of reservoir beds against low- or non-permeable units represents efficient seals (Rotevatn & Fossen, 2011).

In instances of an extremely low-permeability process zone with deformation bands, significant compartmentalization occurs (Rotevatn & Fossen, 2011). This can lead into creating two distinct pressure compartments on each side of the fault process zone. In examples with a lower permeability contrast, pressure drops are more gradual, and the compartmentalization is less significant (Rotevatn & Fossen, 2011). As the fault core permeability affects the compartmentalization of a damage zone, the shale gouge ratio percentages will lower the permeability of the fault core to simulate the idea of Rotevatn and Fossen (2011).

For faults with total displacements of less than ~150 m, damage decays approximately inversely with distance from the fault, and fault zone thickness grows with displacement (Savage and Brodsky, 2011) (Fig. 10). This observation is crucial for this study as it was used to build the geometry of the model. Beyond ~150 m of fault slip, the apparent decay becomes more gradual (Fig. 11), and fault zone thickness

exhibits less growth with displacement. The nucleation of secondary strands may occur when a sufficient number of fractures coalesce into shear planes.

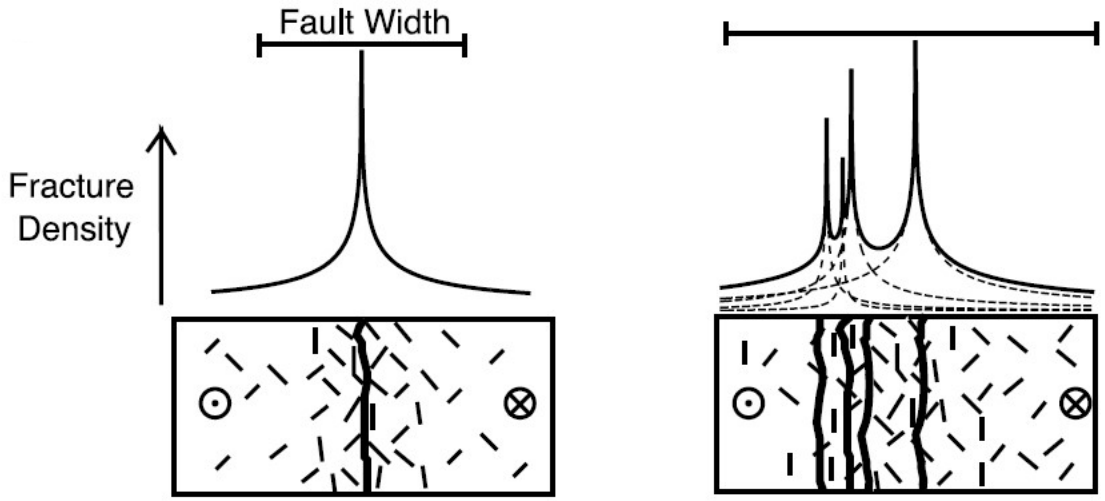

Figure 10. Schematic representation of a fault core fault and distributed slip surfaces from Savage and Brodsky (2011).

Following the method of Ostermeijer et al. (2020) for 1D meso-fracture faults, this study supports that fracture density within the damage zone's fracture density is increasing closer to the fault core. Ostermeijer et al. (2020, with the Borrego Fault example, Fig. 11) implemented a power-law decay model instead of the exponential decay model. This observation leads to the assumption that the fractures' density and their exponential decay strongly affects the rocks' permeability and porosity which differ based on the rock's distance from the fault core. The increase or decrease of porosity and permeability caused by the fractures is discussed later (Chapter 4.2.4).

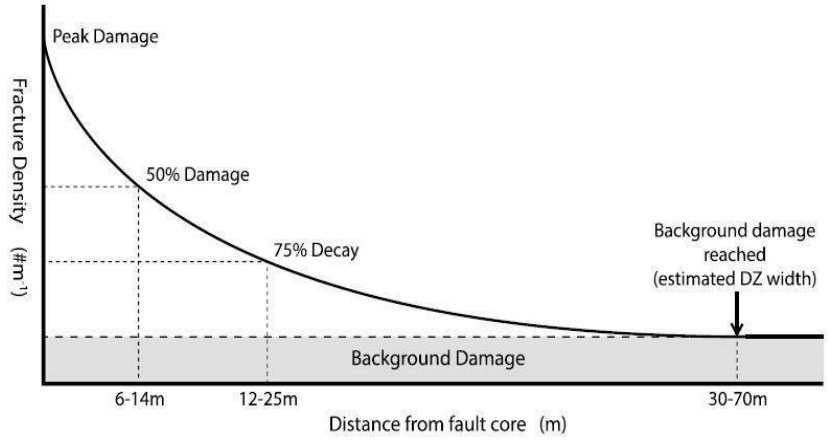

Figure 11. Example of decay trend of a damaged profile in the fault's footwall which illustrates the displacement – damage zone width scaling relationship from the Borrego Fault (Ostermeijer et al., 2020).

Cowie and Scholz (1992) predicted that the fault damage zone width should scale linearly with the fault length. Based on Faulkner et al. (2011), a clear positive relationship between displacement and fault damage zone width can be observed, which is shown by a halo zone of microfracture damage surrounding the fault core. The intercept of this relationship is approximately through the origin. This study implies that fault damage zone width increases with fault displacement.

3 Methods

This chapter will cover the different sets of methods that were used to achieve the aims of this research. For the geology methods, a general kinematic analysis was performed for several faults within a case study area of the WNB by using seismic data (chapters 3.1.1 & 3.1.2.). Secondly, lithologies were derived from nearby well log data to be able to estimate the volume of shale present in the host rock (chapter 3.1.3). The shale volume in the host rock was subsequently used to estimate the amount of shale present in the fault zone (chapter 3.1.4). For the modelling purposes, the hydromechanical model methodology will be explained too. In chapter 3.2.1 the FLAC3D-ToughREACT simulator will be introduced with the simulation logic at chapter 3.2.2.

3.1 Geology methods

A 3D seismic interpretation was conducted on a case study area within the West Netherlands Basin to gain insight into the general tectonic history and fault kinematics. The seismic interpretation was performed by using the Donkersloot seismic dataset (L3NAM2012AR), which is a dataset that was created in 2012 by reprocessing and merging several vintage seismic datasets (Merrifield, 2012; nlog-mapviewer). The Donkersloot seismic dataset adheres to the non-SEG convection, meaning that a rise in acoustic impedance is shown as a blue through and a decrease in acoustic impedance is displayed as a red peak (Chapter 3.1.1.). The following surfaces were mapped in “Petrel” software for this study:

- Top of Chalk Group
- Base of Chalk Group
- Base Rodenrijs Claystone Mb.

The following surfaces were used from previous studies:

- Base Upper Holland Marl Mb. (Vis & de Haan, 2021)
- Base Lower Holland Marl Mb. (Vis & de Haan, 2021)
- Base Rijnland Group (Verreussel & Peeters, 2023)
- Base Delft Sandstone Mb. (Verreussel & Peeters, 2023)
- Base Alblasserdam Mb. (Verreussel & Peeters, 2023)
- Base Altena Group (GDN – V5)

The surfaces were used to construct isopach maps.

The main methodology comprises two primary steps. Firstly, there's the well log analysis, which involves tying the well data to the seismic data by generating synthetic seismograms and aligning the major events. This is achieved by utilizing functions like stretch and squeeze within the software used. After the well tie is completed by integrating well and seismic data, the second step involves conventional seismic interpretation. Subsequently, sequence boundaries of interest are identified, typically based on the newly obtained synthetic seismogram, seismic facies, reflection terminations, and shapes of other well log curves. Seismic facies, representing genetically related deposited units and their boundaries, are then classified. Additionally, fault sticks observed in the available seismic sections are traced to establish the structural framework.

3.1.1 Seismic data fundamentals

To link the seismic data (in ms TWT) to the well data (in m depth), a seismic-to-well tie must be performed. Within a seismic-to-well tie, density and velocity data is used to calculate the acoustic impedance of lithological contrast. The acoustic impedance is defined as:

$$Z = density * v_{P-wave}$$

The velocity data is usually obtained from either a sonic log or checkshot data. The density is derived from a density log if available or directly from the sonic log (Gardner et al., 1974). Both the density and the velocity are then utilized to construct a synthetic seismic trace. This trace closely mirrors a seismic line passing near the well from which the logs were acquired. Subsequently, the synthetic trace is correlated with both the seismic data and the corresponding well log, facilitating a comprehensive understanding of the main lithological transitions in the subsurface.

The difference in acoustic impedance is illustrated in the seismic datasets in different ways. A decrease in acoustic impedance over an interface is depicted as peak and an increase is depicted as a through (Stefan Peeters MSc thesis). To describe how much of the wave is reflected over an acoustic impedance interface, the relationship of reflection coefficient is generally being used.

As described by Sheriff and Geldart (1984), reflection coefficient for a rock contact at normal incidence represents "the ratio of the amplitude of the displacement of a reflected wave to that of the incident wave." Mathematically, the reflection coefficient (R) can be defined as:

$$R = \frac{\rho_2 v_2 - \rho_1 v_1}{\rho_2 v_2 + \rho_1 v_1}$$

where: ρ = rock density, v = P-wave propagation velocity, Subscript "1" represents parameters above the interface, Subscript "2" represents parameters below the interface.

The resolution of the data, based on the study of Verreussel & Peeters (2024), is approximately 30 m.

Isopach maps are contour maps which represent geologic map of subsurface which can be seen isopaches in a plan view for a particular geographic area (Oxford Reference). For the needs of the tectonic analysis of this study, isopach maps were constructed. The contour maps displaying equal values of seismic travel time between two distinct events (Al-Masgari et al. 2021). The isopach maps illustrate the variation in time between two seismic reflections which aim to derive thickness information from seismic data (Al-Masgari et al. 2021). For example, for this study, seismic reflections below a horizon and above another horizon were used in “Petrel” software to estimate the thickness between these two horizons (true stratigraphic thickness). Isopach maps are commonly employed for interpreting thickness variations between interpreted horizons.

3.1.2 Seismic interpretation

The Seismic interpretation with Petrel on a small case study area to get familiar with fault architecture in West Netherlands Basin gave the results for the following chapters.

The seismic sequence analysis is an important “tool” for the identification of the stratigraphic components, the depositional sequences, that are sediments which conformably lay to another genetically and create strata. The upper and lower borders of these depositional units are recognized due to unconformities. These identifications make clearer characteristics such as toplaps, downlaps, onlaps and erosional truncations, reflection terminations that can be observed through the 2D and 3D seismic data of the depositional sequences (Al-Masgari, 2021).

In depositional sequences transgressive-regressive cycles are common in progradational deposits which overlain and underlain down-dip locations and are formed by regression of the shoreline. Onlaps are due to loading of sediments and compaction of them with the effect of the sea level changes while (Christie-Blick, 1991). Generally, onlaps formed when low-angle younger rock strata terminate progressively against an initially older inclined surface during sea level rise. Often, the older rock layer undergoes an erosional process, and the surface is represented by an unconformity. Onlap and (erosional) truncation unconformities surface often impose with each other in space while forming. Both can be caused and co-exist by uplifting, transition and uplifting, as well as propagation of the deposition center (Dengfa, 2018). Toplap is a term used in identifying the situation of inclined sedimentary strata occurring below the

horizontal layers which normally represents a nondeposition hiatus (Hamzah, 2016). Toplap can be identified as strata against an overlying surface mainly because of nondeposition (sedimentary bypassing) with perhaps only minor erosion (Mitchum Jr., 1977).

For this study, the 3D seismic data of the marked area from Figure 6 (black box), were interpreted in order to establish the stratigraphy, in combination with the well log data of the well which overlaps with the seismic cross – section (yellow line for cross – section and red box for the geothermal doublet in Fig. 6).

3.1.3 Well log data

For the analysis of the stratigraphic layers and the shale gouge ratio calculations were used the well log for Boring PIJNACKER-GT-03-SIDETRACK2 from the NLOG Datacenter (Fig. 12). In order to define the fluvial facies of the formations of interest and more specifically the sand/clay ratio of the stratigraphic layers, were used the Gamma – Ray (GR) cut – off log data of the same boring. The stratigraphical sequence of the log as also the correlation of the well log with the seismic data were of crucial importance for the accuracy of the data (values) which were used in the model.

Gamma rays are a type of electromagnetic radiation characterized by their extremely short wavelengths and high frequencies within the electromagnetic spectrum. They are generated by the decay of atomic nuclei in processes such as radioactive decay, nuclear reactions, and certain types of high-energy particle interactions. (Russel, 1944). Gamma rays have very high energy, which allows them to penetrate most materials, making them useful in the field of geophysics and petrophysics, providing valuable insights into the composition and characteristics of subsurface rock formations. Gamma ray logs are a type of well-logging technique that measures the natural gamma radiation emitted by rocks (Katahara,1995). Clays are characterized by a relatively high GR response.

In the current study, the clay – rich deposits defined by GR > 60 gAPI, while sand-rich deposits defined by GR < 60 gAPI. (Szklarz et al., 2022).

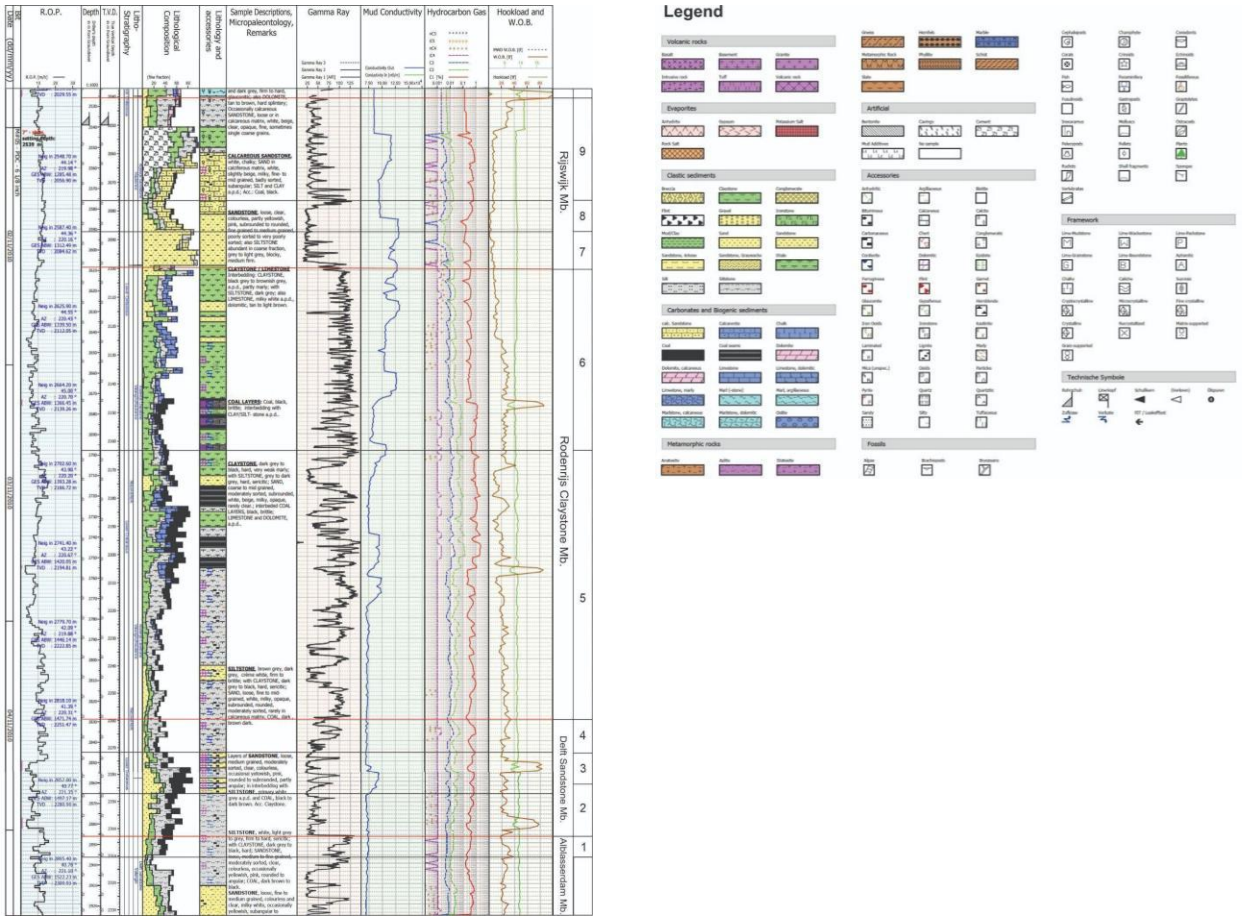

Figure 12. The well log for the Boring PIJNACKER-GT-03-SIDETRACK2 that has been used in the study from the NLOG datacentre.

3.1.4 Deriving SGR - offset calculations

For the analysis of the fault characteristics was used the open source well log from the well next to the fault (NLOG) and the seismic data for the measurement in meters of the juxtaposition. The depth of the formations that were used in the current study are calculated by the log depth in the TVD column and can be seen in Table 1.

Table 1. The depth of the formations from the well log data (TVD column).

Members	*Depth (m)*	*until Depth (m)*
Rodenrijs Claystone Mb. (Δz5)	*2163,2*	*2259,6*
Delft Sandstone Mb. (Δz4)	*2259,6*	*2271,8*
Delft Sandstone Mb. (Δz3)	*2271,8*	*2287*
Delft Sandstone Mb. (Δz2)	*2287*	*2302,9*
Alblasserdam Mb. (Δz1)	*2302,9*	*2310,4*

Based on the well log data, a sand/clay percentage from the Gamma ray data of the log was used to calculate the volume of shale (Vsh).

Seismic data interpretation is the primary method for identifying and mapping faults in the subsurface. Fault detection relies on the presence of mappable seismic reflectors. Discontinuous reflectors indicate fault locations, and the dip separation is estimated by correlating seismic reflectors across the fault. The thickness of the stratigraphic layers was measured in Petrel software in order to calculate the fault offset.

The main idea for the fault gauge calculations is based on the study of Yielding, (2002). The main goal is to estimate the volume of shale present within the fault zone. The shale Gouge ratio arises from the overall composition of the surrounding rocks that have been moved past a specific location on the fault plane and can be calculated by dividing the Vshale over a particular interval by the throw of the fault plane (Fig. 13).

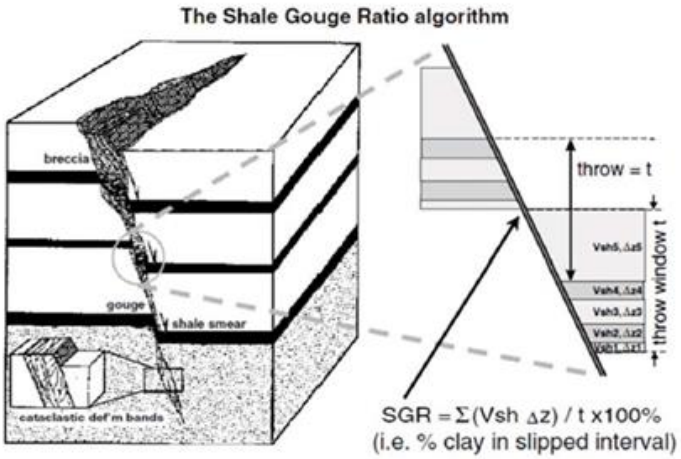

Figure 13. Figure shows an example of the lower sandy part of the Alblasserdam Member and the Shale Gouge ratio algorithm that was used for the calculations, as it was presented in the WarmingUp report of 2022.

The calculations for the shale – gouge ratio are based on the relationship from S.P. Szklarz et al. (2022) & Yielding (2002):

$$SGR = \frac{\Sigma(Vsh\ \Delta z)}{t} * \ 100\%$$

(i.e. % clay in slipped interval)

3.1.5 Expansion index

The construction of the expansion index was based on Fossen's book (2016). Faults that reach the surface create a relief that impacts the depositional pattern of sediments. When sediments are deposited over

the entire fault structure, not just in the hanging wall, the layers on the hanging-wall side will be thicker. This thickness difference varies along syndepositional faults and indicates variations in fault activity over time. This variation is quantified using the expansion index, which is a simple measure of the difference in thickness across the fault for any given stratigraphic unit:

Expansion index = t_{HW}/t_{FW}

During periods of fault activity, the expansion index is greater than 1, and it is largest for the layer deposited when the fault was most active. When the fault is completely post-depositional, the index is 1. For syndepositional reverse faults, the footwall layers expand, resulting in an expansion index of less than 1 during syndepositional faulting.

For the input values were used the sediments' thickness from both sides of the FOI as they measured in the seismic cross – section.

3.2 Hydromechanical model methodology

3.2.1 FLAC3D-ToughREACT: A coupled Thermo-Hydro-Mechanical-Chemical simulator

The scope of the current study is to model the changes in stress, strain, fluid pressure, and temperature during a cold-water injection scenario. To do so, the coupled THMC (Thermo-Hydro-Mechanical-Chemical) simulator FLAC3D – ToughREACT is used. This simulator consists of two separate commercial software packages: FLAC3D for the mechanical framework, and ToughREACT as the flow simulator. ToughREACT uses multiphase, multi-component, non-isothermal thermodynamics, reactive transport, and chemical precipitation/dissolution equations. However, the chemical precipitation/dissolution component is not used in this study. Both software packages communicate through the FLAC – ToughREACT coupling code by Taron et al. (2009). This methodology enables the calculation of short-term build-up in fluid pressures in FLAC3D, resulting from an instantaneous change in stress.

The two software packages are coupled cyclically with the coupling cycle following a loose coupling (communicate through well-defined interfaces or contracts but they do not rely heavily on each other's internal workings, Fig. 14). The simulation initiates with the equilibration of temperature and pore fluid pressure in ToughREACT which then interpolates to corner node information as input to FLAC3D. Constitutive relationships within the interpolation module convert these outputs into fluid bulk modulus, obtained from IAPWS steam table equations, and permeability changes due to mineral behaviour.

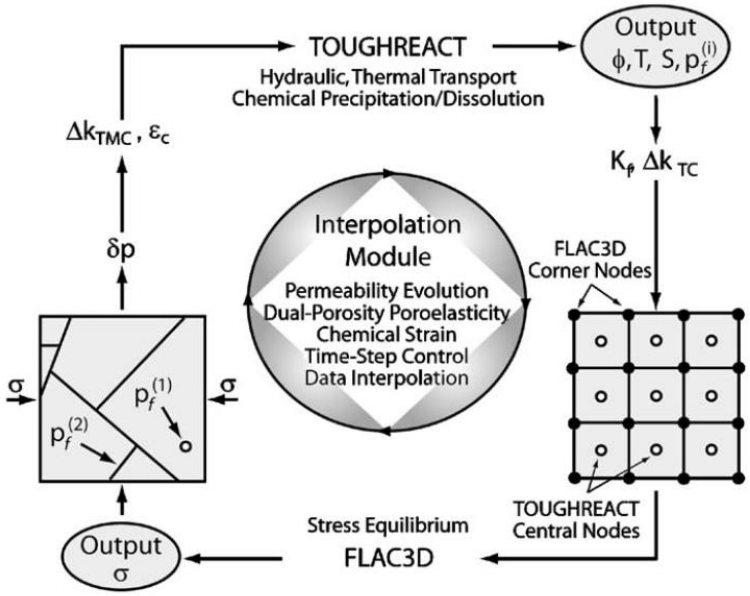

Figure 14. Relationship between ToughREACT and FLAC3D (Taron et al. 2009).

For the modelling, properties that was necessary to be defined filled are: permeabilities for the intact reservoirs (PanTerra report, 2019), porosity (PanTerra report, 2019), initial pore pressure (calculated), initial temperature of the reservoir (PanTerra report, 2020), solid density for each layer (Willems and Nick, 2019), specific heat of both of the reservoirs (Willems et al., 2020) and the fault core (Crooijmans et al., 2016), thermal expansion (Soustelle et al., Warming Up, TNO, 2022), heat conductivity (calculated), biot coefficient (PanTerra report, 2019), bulk modulus (Soustelle et al., Warming Up, TNO, 2022) and Poisson's ratio (Soustelle et al., Warming Up, TNO, 2022).

For the permeability values of the fault, three permeability values are required (one for each direction axis).

3.2.2 Model Geometry

The model dimensions are 2000 m long on the x-axis, starting from -1000 (left hand side) to +1000 (right hand side). The y-axis is 1000 m long, starting at 0 m to +1000m. The fault is parallel to the y-axis and runs from (x=0, y=0) to (x=0, y=1000). The depth of the reservoir along the z-axis is between -2250 m and -2420 m. The top of the overburden is located at -1700 m and the bottom of the underburden is located at -2600 m. A schematic of the geological interpretation used for setting the model in FLAC3D-ToughREACT is shown in Figure 15.

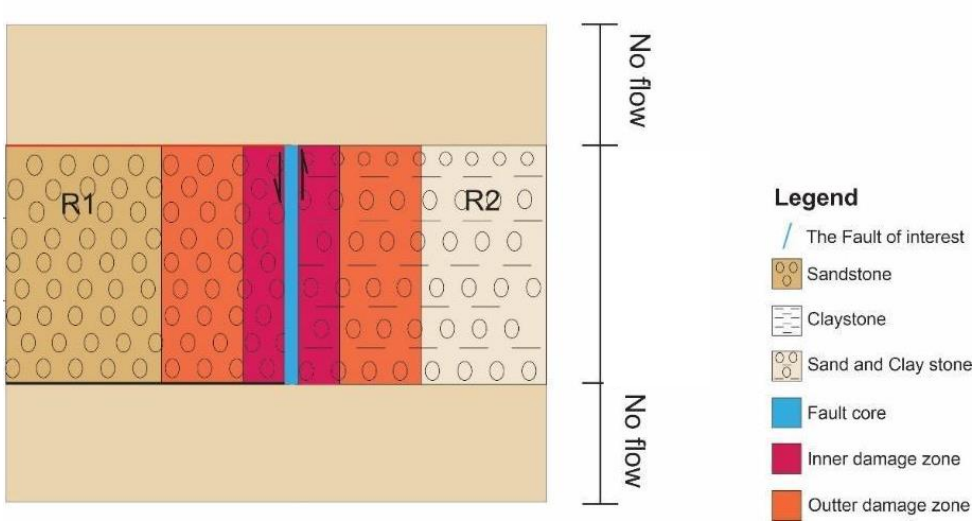

Figure 15. Conceptualization and simplification of the geological interpretation, which is used for setting up the THM – coupled model in FLAC3D – ToughREACT.

The fault core, when present, is modelled as a volume of elements, 1 single element wide. One single element width is the smallest width possible to represent a fault core in the model, which in comparison with reality, a fault core should be some cm or mm. As 1 single element represents 8 m width, scaling relationships will be applied.

For filling the different SGR percentages, it is needed to create first a fault core zone that corresponds to the scale of the model (scaling from reality values to the model's geometry). For this zone it was necessary to scale the real fault's width to match with the width of a single plane of elements. An estimation of 8 cm was used as the realistic number (fault real) for the scaling. The width of the model element is 8 m, a zone too big to be used as the realistic fault width.

As the flow rate Q of a Darcy-type flow is in a given direction and constant on the model, the fault scaling for the model can be calculated by using only the x – axis length of element (L). The permeability on the y and z axes is also necessary to change while the surface area perpendicular to L is different in the axes y and z. Other property that scaled was the porosity of the fault core. For the scaling were used the relationships:

For x-axis permeability in the fault:

$$\kappa_{yy,zz}^{\text{model}} = \frac{L_{\text{true}}}{L_{\text{model}}} \kappa_{yy,zz}^{\text{true}}. \quad (1)$$

For y- and z-axes permeabilities in the fault:

$$\kappa_{yy,zz}^{\text{model}} = \frac{L_{\text{true}}}{L_{\text{model}}} \kappa_{yy,zz}^{\text{true}}. \quad (2)$$

3.2.3 Injection scenario

As the main scope of this study is to determine the effect of geothermal activity close to the fault of interest, an injection scenario was based on a real geothermal injection scenario used at the Kwintsheul geothermal doublet located in the WNB. The injection well in the model was implemented as a number of injection dummy elements in the flow model. In the base case model, without a damage zone, the injection location was 50 meters away from the fault. The position of the injector in the model with damage zone is at 55 meters away from the fault, since there is no element centred at 50 m from the fault.

About 70 kg/second of water is injected at this site. In the model, cold water injection occurred along a vertical line consisting of 6 elements. This means that per element 5.79 kg of water per second was injected, while at x=0, the model was developed to create symmetric plumes on the two sides of xx' axis. Injection was constant for the entire simulation time. The temperature of the injected fluid was 30°C.

3.2.4 Stable parameters on the model

For the base case, the damage zone width equal to 0 m was decided. The Base case scenario model was created to represent the two reservoirs directly juxtaposed, without a fault impacting fluid flow. For this base case model, the SGR = 0% and its combination with the damage zone width equal to 0 m will give a basic model which results in a base for open discussion. The influence of the shale gouge ratio and the Damage zone width correspond to the main purpose of this study. For this reason, all the scenarios that will differ from each other on their shale gouge ratio percentage (SGR%) as fault core permeability and the presence or absence of the damage zone (as changes in the scenarios' properties), as they measured from the seismic data.

Several parameters were obtained from literature for the modelling. The values that FLAC3D model was based on are the temperature of the reservoir, equal to 71°C (PanTerra report, 2020; see Appendix 8.1), the solid density equal to 2650 kg/m^3 for both reservoirs (Willems and Nick, 2019; Appendix). For the Biot

coefficient was used the value 0,75 which was found in PanTerra report (2019). The effective pressure = 31 MPa calculations can be seen in the Appendix (8.1).

For the intact parts of Alblasserdam Mb. and Delft Sandstone Mb. formations, the permeability and porosity remain stable to all the model scenarios. These values are changing on the reservoirs of the model scenarios with damage zone, on the damage zone part. Both intact parts of the reservoirs stay stable in all the scenarios. The permeability changes for fault core which varies as different shale-gouge ratio percentages in different model scenarios and the inner and outer damage zone, where permeability values are changing also when decreasing or increasing.

The value which was used for the permeability of the Alblasserdam for the model was from the results of the PanTerra report (2019) study. Based on this study the porosity for transition zone[1] of Alblasserdam Mb. and Delft Mb is 25.3% for Alblasserdam Mb. (0.253 in the model) and 27.7 % Delft Sandstone Mb. (0.277 in the model).

Values for three orthogonal permeability are required because the model is 3D and the calculations are corresponding to the axes x, y and z.

The Alblasserdam Member sand parts are less porous and are therefore less permeable, based on the literature overview (PanTerra report, 2019) but also the gamma-ray data of the existing well log data. The Horizontal permeability (kh) (yy direction) for Alblasserdam Mb. was based on the depth of the layer of interest.

For Alblasserdam Mb., for the one horizontal direction of permeability was chosen the value 2.96 x 10^{-13} m^2 (PanTerra report, 2019) and as second horizontal direction of permeability, the value 1.49 x 10^{-13} m^2 (PanTerra report, 2019).

The Vertical permeability (kv) for Alblasserdam Mb was calculated from the anisotropy of the reservoir ratio kh/kv ~ 3.8 (PanTerra report, 2020). For the horizontal permeability (kh) was used kh = 1.49 x 10^{-13} m^2 which leads to the vertical permeability equal to kv = 0,39 x 10^{-13} m^2.

[1] *the broken or/and weathered zone between one stratigraphic layer (subsoil) to another (unaltered bedrock). Can be caused from chemical weathering or physical processes or both. Stratigraphic layers of transition zone can differ to their hydraulic properties; Geological Survey of Ireland - Transition Zone (gsi.ie)). For this case is the zone that the rock formation gradually changes from Alblasserdam Mb. characteristics to Delft Sandstone Mb. characteristics.*

For the Delft Sandstone Member were empirically estimated values for permeable sandstones. The empirically chosen values for the three directions of permeability are 7.00 x 10^{-13} m^2 and 6.00 x 10^{-13} m^2 for horizontal permeabilities and 1.80 x 10^{-13} m^2 for vertical permeability.

From the elastic moduli were used the bulk modulus and the Poisson's ratio (Soustelle et al., Warming Up, 2022; see Appendix 8.4). The values for bulk modulus of the two reservoirs are 3,7 GPa for Alblasserdam Mb. And 6 GPa for Delft Sandstone Mb. The values for Poisson's ratio of the reservoirs are 0,187 for Alblasserdam Mb. and 0,154 for Delft Sandstone Mb.

With the values of this chapter was created the model that was used for the base case model scenario (Table 2). The model is filled with the values of the reservoirs, the fault values are the average of the reservoirs' values. No damage zone exists.

Table 2. The values for various mechanical, hydraulic, and thermal properties used in the base case model scenario.

	Fault core			***Reservoir 1 (Alblasserdam Mb.)***			***Reservoir 2 (Delft SSt Mb.)***		
Initial Pore Pressure	*23 MPa*								
Initial Temperature	*71 °C*								
Porosity	*5%*			*25,3%*			*27,7%*		
Bulk modulus	*5 GPa*			*3,7 GPa*			*6 GPa*		
Poisson ratio	*0,165*			*0,187*			*0,154*		
Solid density	*2650 kg/m3*			*2.650 kg/m^3*			*2.650 kg/m^3*		
Thermal expansion	*8,75 x 10^{-5} °C*			*8,2 x 10^{-5} °C*			*9,3 x 10^{-5} °C*		
Heat conductivity	*4,5 Wm−1 K−1*			*4,5 Wm−1 K−1*			*4,5 Wm−1 K−1*		
Specific Heat	*730 J kg^{-1} K^{-1}*			*730 J kg^{-1} K^{-1}*			*730 J kg^{-1} K^{-1}*		
Initial Permeability	*5,00 x 10^{-13} m^2*	*3,75 x 10^{-13} m^2*	*1,00 x 10^{-13} m^2*	*1.49 x 10^{-13} m^2*	*2.96 x 10^{-13} m^2*	*0,39 x 10^{-13} m^2*	*7.00 x 10^{-13} m^2*	*6.00 x 10^{-13} m^2*	*1.80 x 10^{-13} m^2*

4 Results

In the chapter of results will be evaluated both the geology results and the model results. Also, the link between the geology interpretation results and the FLAC3D-ToughREACT model simulation will be explained.

4.1 Geology Results

In this chapter the results from the geological analyses will be described. Paragraph 4.1.1. describes the results from the seismic mapping and fault kinematic analysis from the cross-section with the geothermal well of interest. In paragraph 4.1.2 the seismic facies analysis and the offset calculations are presented. Paragraph 4.1.3 describes the results of the shale – gauge ratio estimations.

4.1.1 Results from seismic data

The Seismic interpretation on a small case study area to get familiar with fault architecture in West Netherlands Basin gave the results for the following chapters. Within this chapter, first the results of the 3D seismic mapping are described via the time surface maps (4.1.1.1), which were created for the intervals of interest (see also chapter 3.1), via the isopach maps (4.1.1.2) and via the interpreted seismic cross-sections (4.1.1.3).

4.1.1.1 Time surface map of the Reservoir of interest

Three surface maps were created in this study, being: Top of the Chalk Group, base of the chalk Group and the base of the Rodenrijs Claystone Mb. (Corresponding to the top of the Delft Sandstone Mb.) (see also chapter 3.1). In Figure 16, the time surface map of the top of the Delft Sandstone Mb is shown. The red color corresponds to the shallowest parts. Normal faults of NW – SE direction cut the surface of Delft Sandstone Mb. The top of the Delft interval ranges in TWT position (and hence in depth between 1000 ms TWT and 2200 ms TWT). Because of this are observed alternations of horsts (areas with red star/ Fig. 16) and halfgrabens (areas with blue star in Fig. 16). The Fault A in Figure 16 offsets the reservoir close to the well of interest.

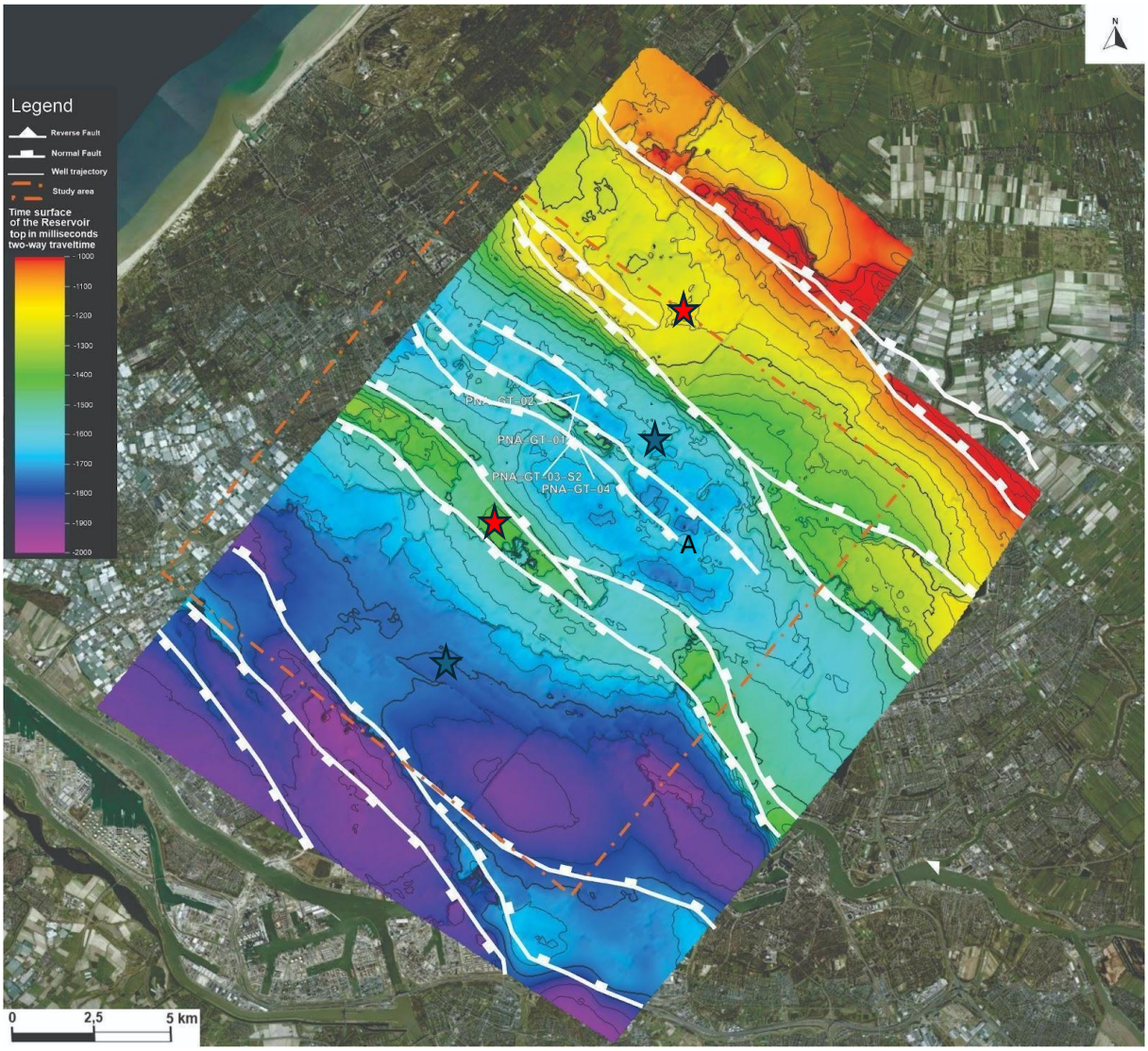

Figure 16. The time surface map of the top of the Delft Sandstone Mb, which is the main reservoir of interest for geothermal energy within the area of interest.

4.1.1.2 Time thickness maps

Based on the age of the Stratigraphic Group or Member they represent; the time thickness maps are presented below.

Thickness map of Early Jurassic

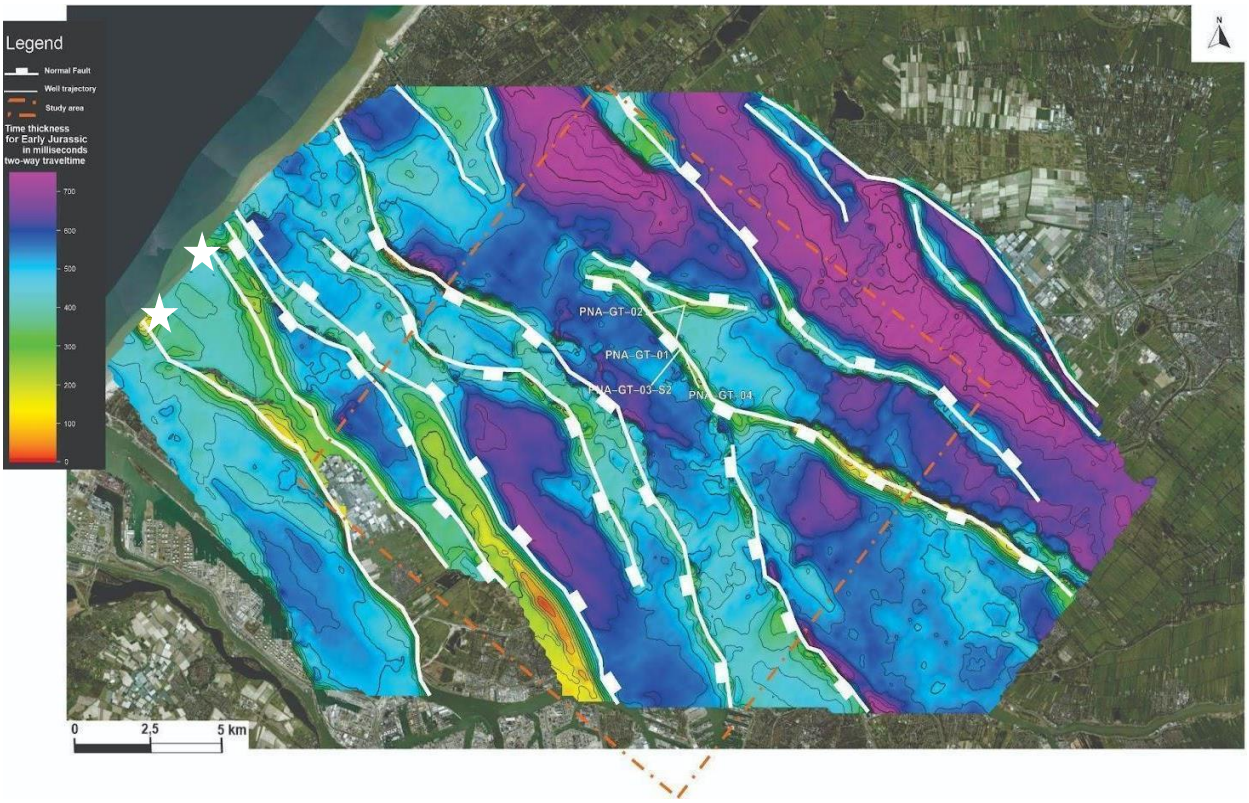

Figure 17. Time thickness map of the Early Jurassic. The thickness map was constructed from the intervals of Altena Group (base interval) and Alblasserdam Member (top interval).

The main observations on the Early Jurassic thickness map (Fig. 17) are the normal faults of NW – SE direction. The uninterpreted faults on the West side of the map were not investigated because of their complexity (Fig. 17/ faults with white stars). In the seismic line, these faults seem to be reversed even if it is clear that they are tilted faults which were originally normal. Their complex kinematic elements were decided to not be presented on the thickness map as it is not necessary. For this time thickness map, the depositional pathways between the normal faults (higher thicknesses, yellow/ orange parts) can be attributed to the later inversion which slightly affected the thickness of the sediments of the Early Jurassic. This can lead to the false interpretation of the normal faults as inverse, making crucial the understanding of the effect of the faults and tectonic events in a specific geological time frame but, at the same time, placing them as a part in geological history of the area, holistically.

Thickness map of Late Jurassic

The Late Jurassic sedimentation contains the Delft Sandstone Member, the Alblasserdam Member and the Rodenrijs Claystone Member.

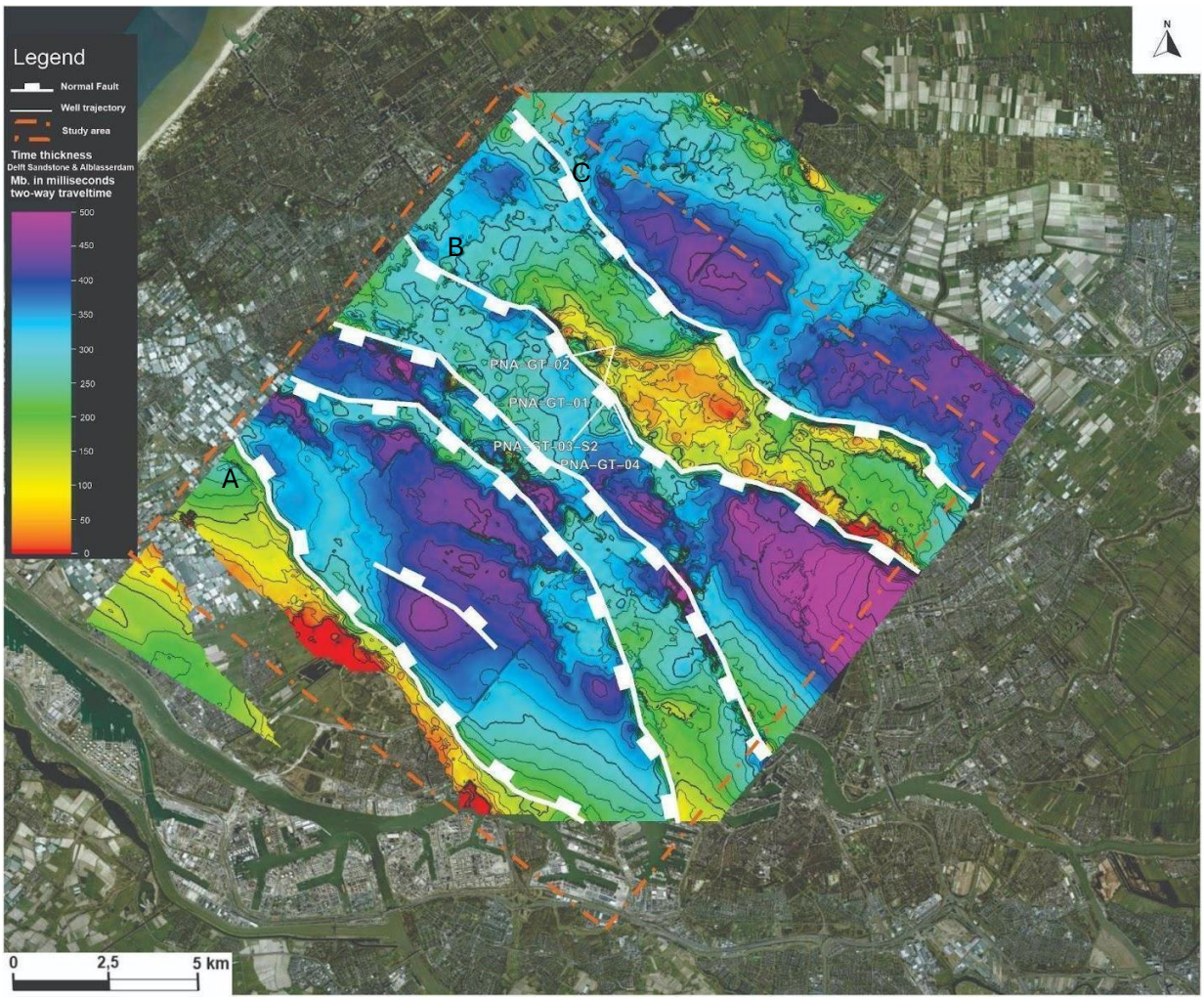

Figure 18. Time thickness map of the Delft Sandstone Member and the Alblasserdam Member which contains the reservoir of interest. The A, B and C faults cause the main thickness differences on the map.

The time thickness map of the Delft and Alblasserdam Mb. (Fig. 18) is characterized by significant differences in TWT thickness. Faults often mark major transitions in TWT thickness, separating horsts from (half)grabens (faults A, B, C/Fig. 18). The thickest accumulations of this interval are found in the hanging walls of the major NW-SE oriented faults (indicated in white in Fig. 18). Also note the concentric shape of the depocenters within the half(grabens).

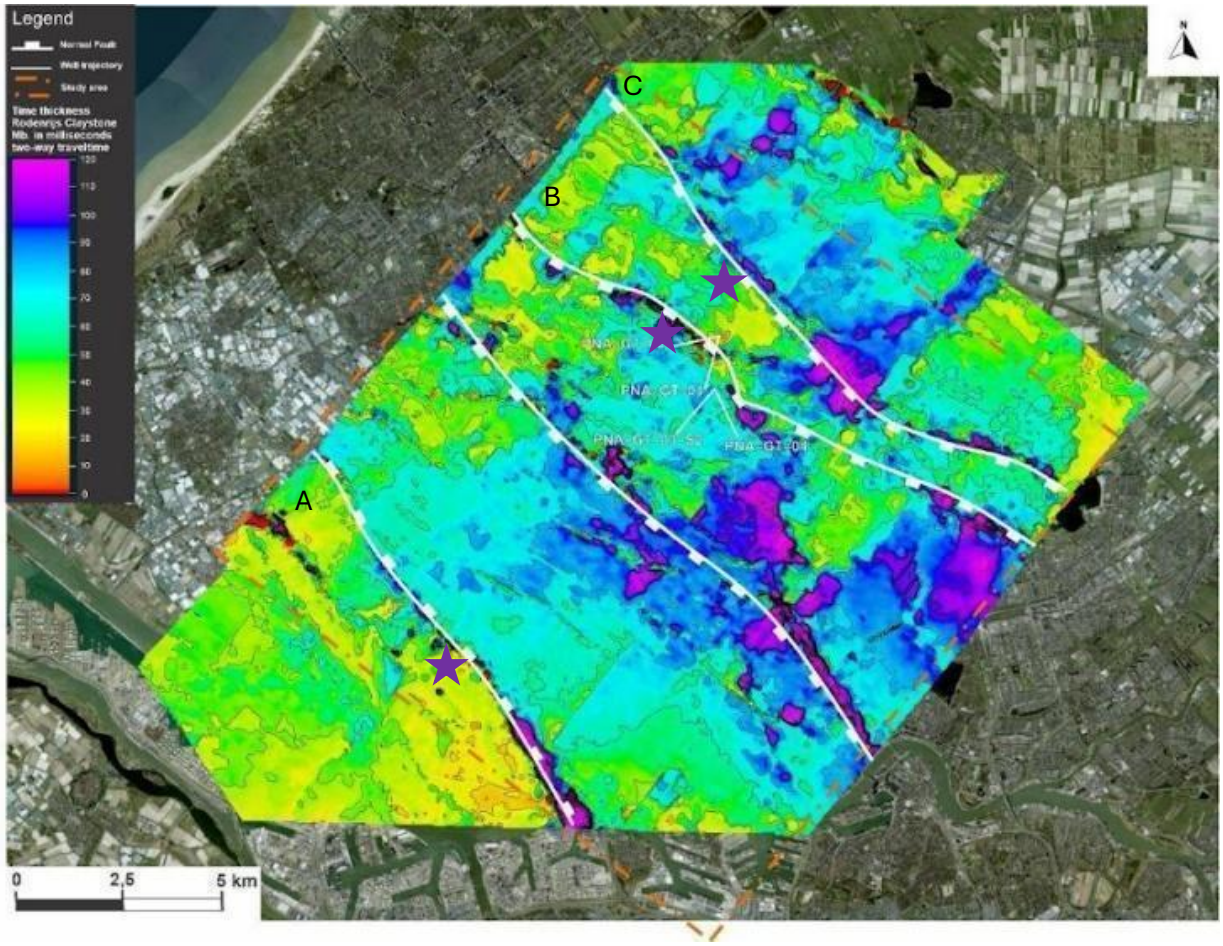

Figure 19. Time thickness map of the Rodenrijs Claystone Member. Purple stars point out the thickness differences. A, B and C labelled faults cause these thickness differences.

For the Late Jurassic was identified the Rodenrijs Claystone Member (Fig. 19) with the thickness differences to be way less than the Delft-Alblasserdam Members thickness map but they still exist (purple stars/ Fig. 19). The position of the faults that caused the topographic differences on this map (faults A, B, C/ Fig. 19) seem to match the faults that were observed in the previous map (Fig. 18) causing the thickness differences. The normal faults that are observed are the faults that are visible in the cross – section until the surface of the horizon (top interval), as the previous maps.

Thickness map of Early Cretaceous

The early Cretaceous corresponds to the Vlieland Formation, deposited during the earlier part of Early Cretaceous (Fig. 20), and the Holland Formation (Upper and Lower Holland Formations), deposited during the later part of Early Cretaceous (Fig. 21). These two formations together constitute the Rijnland Group (Early Cretaceous).

In the Early Cretaceous' time thickness map, it is visible that the faults' direction stills NW – SE as before, with more faults interpreted as the time thickness map of Rodenrijs Claystone Member. Faults continued or created as normal movement in the post – rift phase, however, in the time – thickness map they interpreted as reverse faults (Fig. 20).

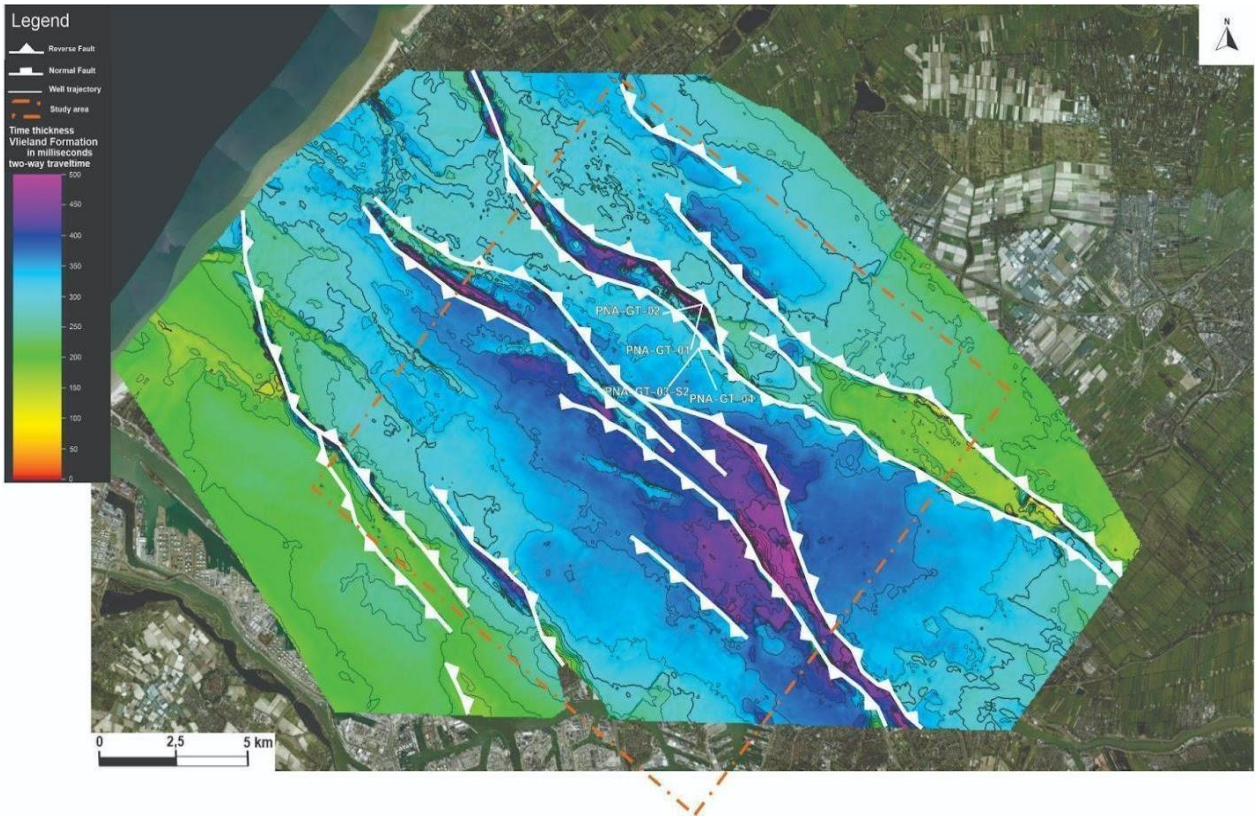

Figure 20. Time thickness map of the Vlieland Formation (Early part of Early Cretaceous), part of Rijnland Group of Early Cretaceous.

The direction of the formed faults continues in the later age of Holland Formations, giving, however, a more linear impression (Fig. 21). It is important in this study that the faults are followed and interpreted to as many geological ages as possible in order to understand the evolutionary stages of the faults.

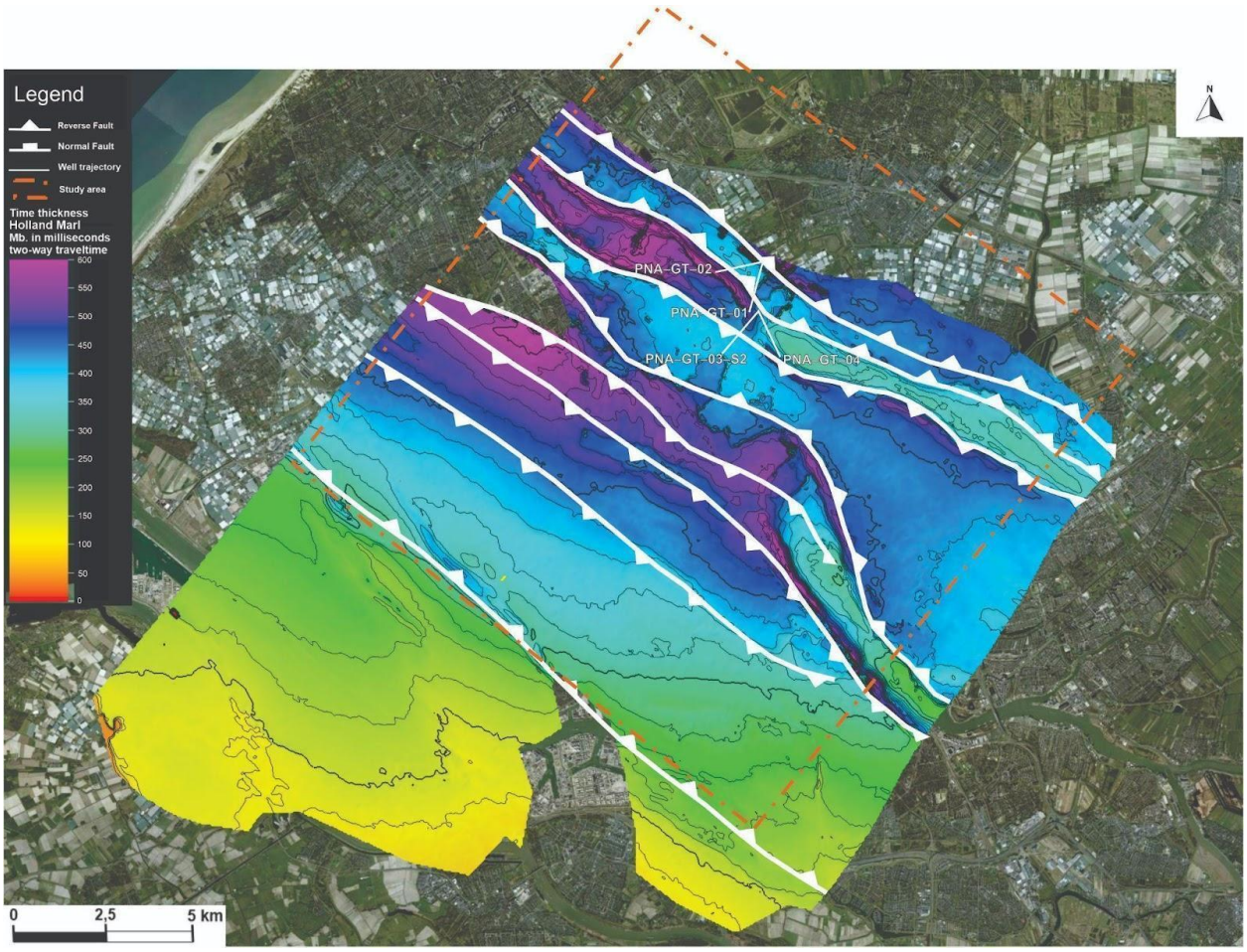

Figure 21. Time thickness map of the Holland Formation (Upper and Lower Holland Formations, Late part of Early Cretaceous), part of Rijnland Group of Early Cretaceous.

Thickness map of Late Cretaceous

In the time thickness map of Chalk Group which was created in the reverse phase of Late Cretaceous, are visible the main tectonic structures of the inversion (Fig. 22). In the same direction, NW – SE reverse faults replace the depocenters with thick layers of sediments caused by the inversion. The normal faults of Holland Formations (Fig. 21) can be seen as inversed and slightly altered or combined in the time thickness map of Late Cretaceous (Fig. 22).

Chalk Group is partially absent within the study area. This is a result of inversion, which caused uplift and subsequent erosion (absent area with blue arrows in Fig. 22). The erosion of Chalk Group is also visible in the seismic line (Fig. 22/ cross-section) with later sedimentation above the eroded part.

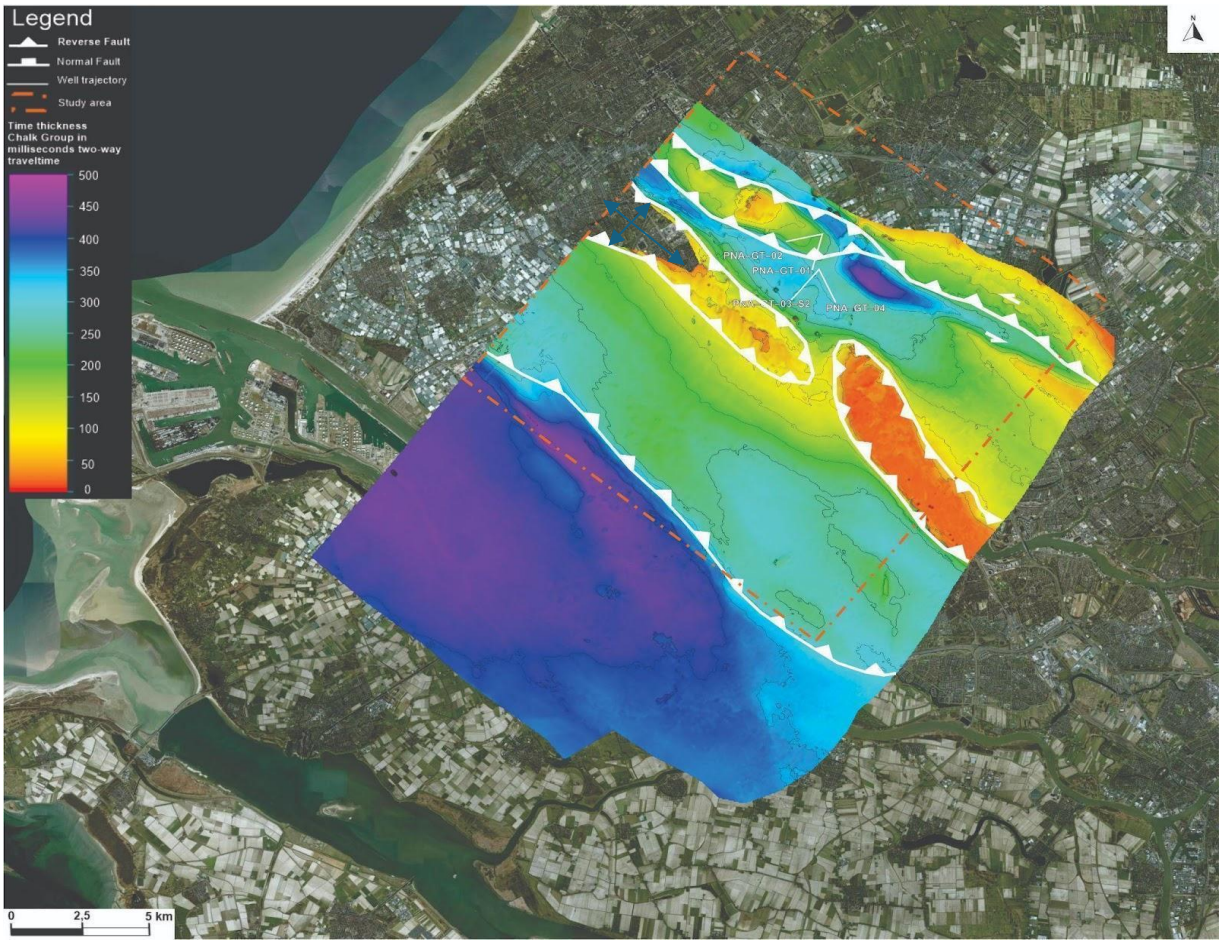

Figure 22. Time thickness map of Chalk Group, formation of the Late Cretaceous. The blue arrows correspond to the position of the eroded part of the Chalk Group.

4.1.1.3 Seismic cross – section analysis

A NW-SE seismic cross section is shown in Figure 23 to illustrate the major phases in the tectonic evolution of the study area. Based on the seismic interpretation, many normal faults reactivated as reversed and marked as red to be distinguished (Fig. 23b).

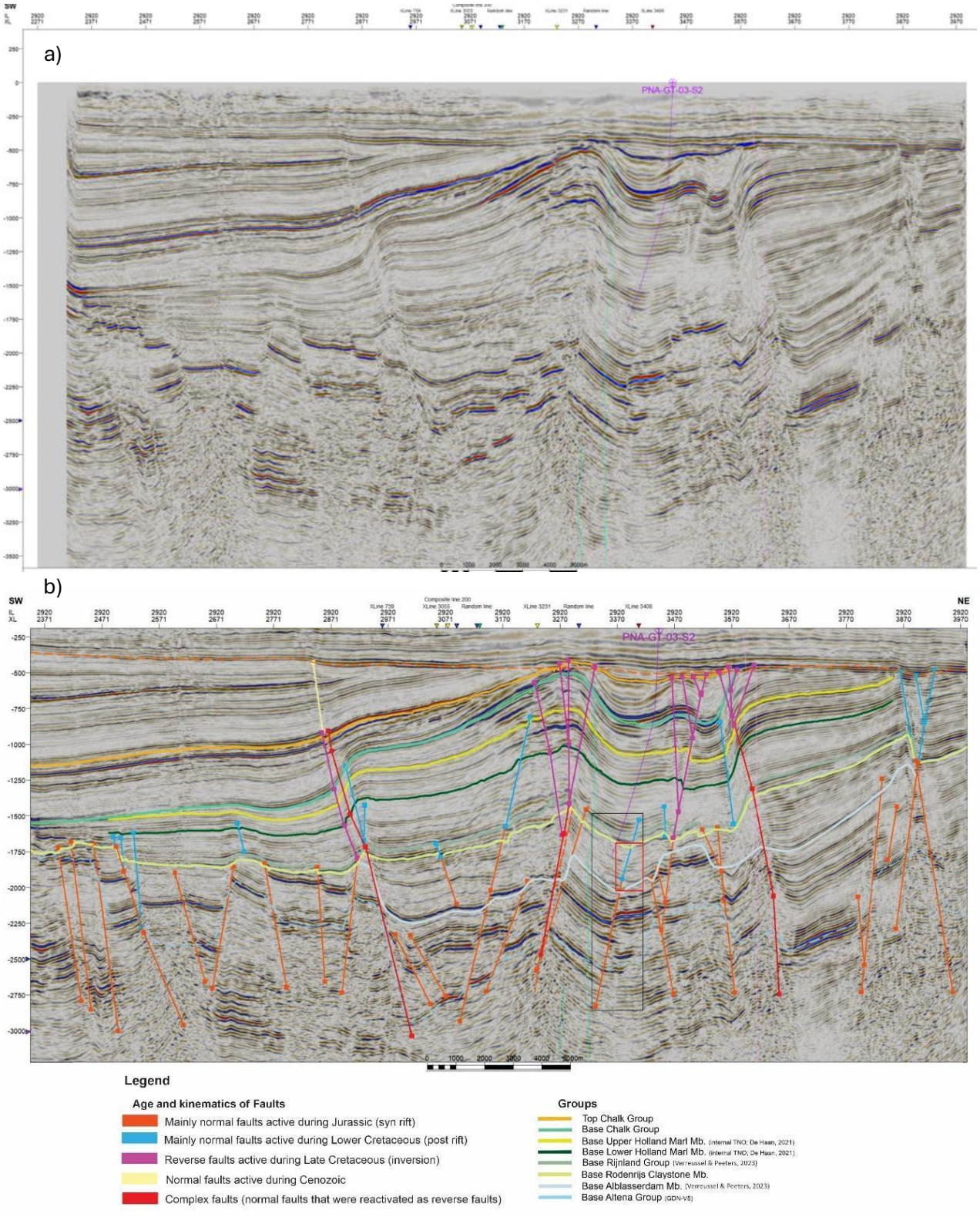

Figure 23. a) SW – NE 2D seismic cross – section before the seismic interpretation with the geothermal well of interest. The exact position of the seismic cross – section can be seen in Fig. 23. b) The same seismic cross – section but interpreted, with the faults grouped by age and their kinematic activity and the stratigraphic groups.

Analyzing the interpreted cross – section of Figure 23a, intervals which were defined in this study or previous study give a clearer impression of discontinuities and other tectonic characteristics. In the SW – NE seismic cross – section, the faults were grouped by age and activity as the main faults correspond to an event that in this care takes place in a specific age frame. It can be safely assumed that many of the faults, especially of the age Lower Cretaceous, are synsedimentary faults. Analysing the fault of interest in a later chapter, its expansion index proves its synsedimentary nature (Chapter 4.1.3). As it can been observed in the Fig. 23b, normal faults were active mostly during Jurassic, caused by the extension of the syn – rift tectonic phase, with the post – rift normal faults taking place during Lower Cretaceous. The analyzed horizons and the image of the previously existed normal faults are all of them clearly affected by the Late Cretaceous' inversion, with the purple faults giving the kinematic sense in flower structures (around the well) and, apparently, create the uplifts. The anticlines (uplifts) and synclines are strong indicators of the inversion. The toplaps of intra-chalk seismic reflectors against the base of the North Sea Group (black arrows) and the much thinner Chalk Group above the pop-ups, which is also partly absent (as can be seen from the Chalk Group/ Late Cretaceous thickness map), are all results of erosion after the inversion (Fig. 23b).

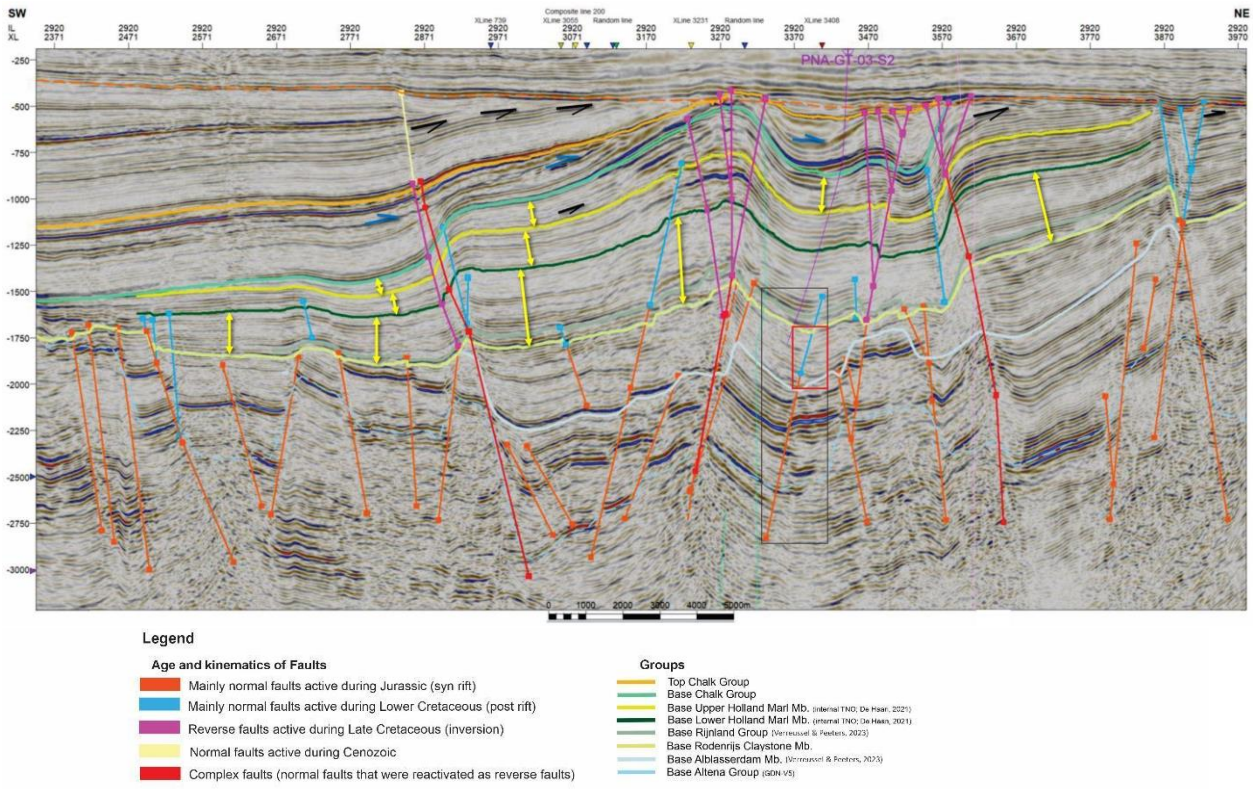

Figure 24. Thickness differences, onlaps and toplaps observed in the seismic cross – section of Figure 23.

The thickness differences (yellow arrows, Fig. 24) are also a very important observation which indicates sedimentation during active tectonics. The thickness differences reveal the syn-tectonic nature of the sediments, although it is important to consider that the sediments' actual thickness was deformed by the reverse phase of Late Cretaceous.

The observed onlaps (blue arrows), erosional truncations and toplaps (black arrows) of Figure 24, complete the tectonic history by indicating the complexity of the study area such as basin infill, synsedimentary faults and erosion. The toplaps and the erosional truncations relate to the eroded parts of the Cenozoic sediments, and partly of the Chalk Group. The onlaps relate to the infill of the basin which existed in the Lower Cretaceous, in the post – rift phase.

4.1.2 Results for the Seismic Facies Analysis and offset calculations

The nature of the fault is syndepositional, based on the cross – section's observations of chapter 4.1.1.3 and the construction of the expansion index of the sediments as measured in the seismic cross – section (Fig. 23b). The expansion index here represents the sedimentation difference during the syn – tectonic deposition of the FOI.

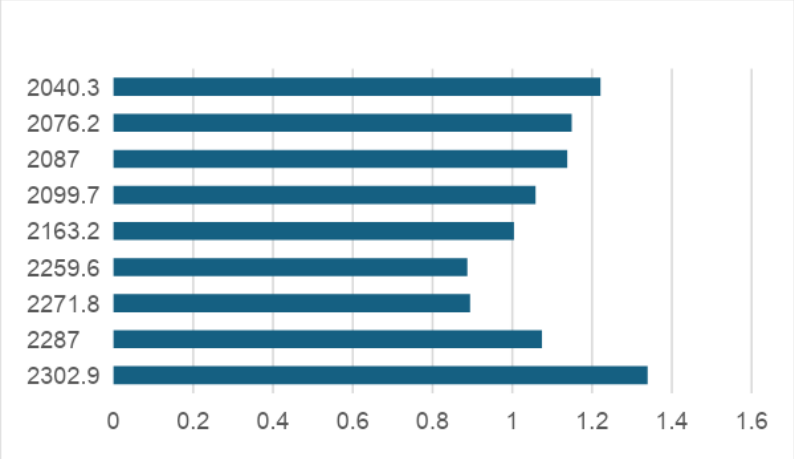

Figure 25. Expansion Index of the syndepositional fault that will be modelled. In the x axis are the ratio results and in the y axis are presented the depths (TVD) in m.

In Figure 25 is visible the gradual change of the sedimentation difference through the thickness ratio between the layers on the two sides of the fault. In a depth axis, the smallest ratio corresponds to smaller difference and as it can be observed, the deposition environment around the fault changes with time and consequently with depth. On the x-axis the results of the calculated expansion ratio are presented, as it was explained in the methods section. The ratio never becomes zero (0) which leads to the conclusion

that the fault was active during all the sedimentation in Early Cretaceous (post – rift phase) until it was completely buried.

4.1.3 Results of the shale gauge ratio estimations

The calculations are based on the 2D measurements of the seismic – cross section (Fig. 23b), even knowing from the analysis of the 3D data set that the characteristics of the fault (and the shale gouge ratio) vary also horizontally. The throw measurements of the fault are calculated, which is illustrated in Figure 26. The construction of the fault window was made based on the combination of the well log data and the seismic data.

The points on the fault correspond to the throw of each stratigraphic layer.

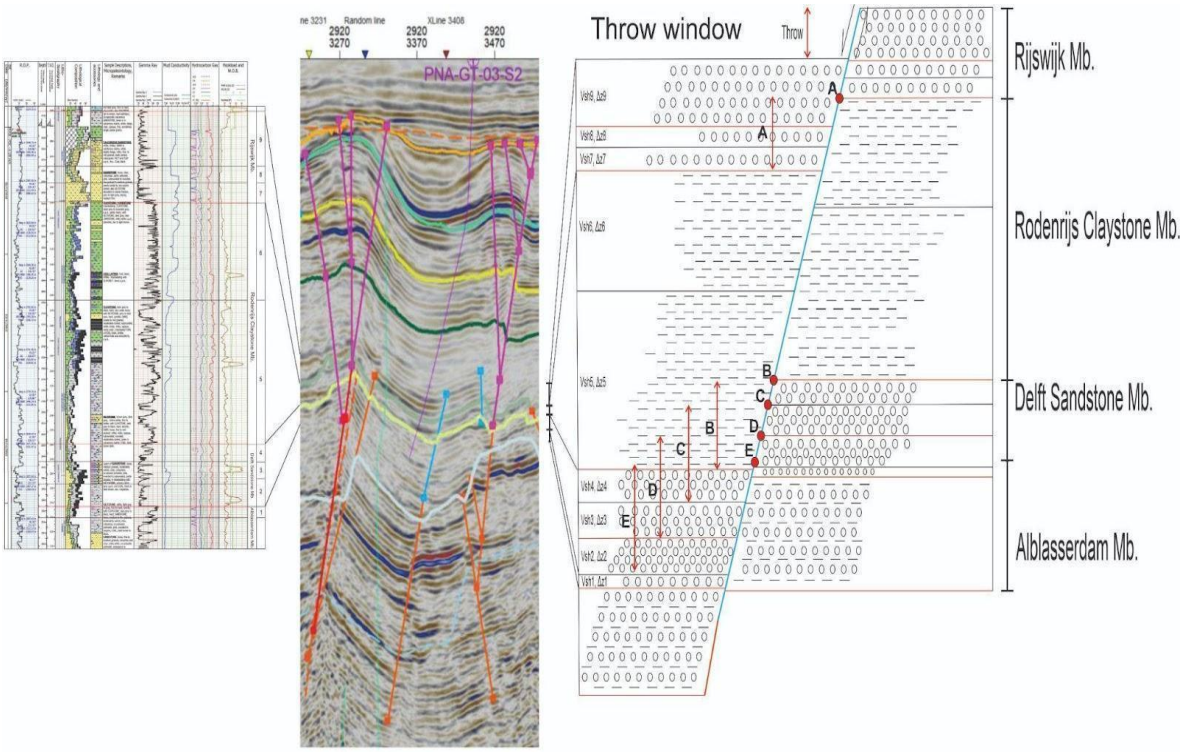

Figure 26. Correlation of the well log with the seismic cross – section and the construction of the throw window through these data.

Table 3 was constructed to explain the calculations based the shale gouge ratio equation of Yielding, G. (2002) (3.1.5 on method section). The shale gouge ratio calculations provide important information to understand the mechanical and fluid flow behaviour of the fault. Additional information for the properties of the fault is crucial for its modelling. The overall composition of the surrounding rocks that have been moved past a specific point on the fault plane and can be calculated by dividing the Vshale over a particular

interval by the throw of the fault plane. Gamma ray data of the log was used for the volume of shale (Vsh) input.

Table 3. Calculations of the Shale Gouge ratio.

Point	Number	Name	Sediment	Thickness*	Vshale	Vshale*Thickness	Throw (t)	Shale Gouge Ratio (%)
Point A	9	Rijswijk Mb.	sand/clay	15,625 m	0,55	8,6	41,9 m	31,83 %
	8	Rijswijk Mb.	sand	10,8 m	0,38	4,104		
	7	Rijswijk Mb.	sand	12,8 m	0,05	0,64		
Point B	5	Rodenrijs Claystone Mb.	claystone	49,425 m	0,72	35,586	50,6 m	70,33 %
Point C	5	Rodenrijs Claystone Mb.	claystone	35,625 m	0,72	25,65	55,77 m	56,5 %
	4	Delft Sandstone Mb.	sand	12,2 m	0,48	5,856		
Point D	5	Rodenrijs Claystone Mb.	claystone	18,625 m	0,72	13,41	55,77 m	46,8 %
	4	Delft Sandstone Mb.	sand	12,2 m	0,48	5,856		
	3	Delft Sandstone Mb.	sand	15,2 m	0,45	6,84		
Point E	5	Rodenrijs Claystone Mb.	claystone	3,1 m	0,72	2,23	55,77 m	39,8 %
	4	Delft Sandstone Mb.	sand	12,2 m	0,48	5,856		
	3	Delft Sandstone Mb.	sand	15,2 m	0,45	6,84		
	2	Delft Sandstone Mb.	sand	18,15 m	0,4	7,26		

** Thickness of the part of the layer that is included to the throw*

V = volume, measured as percentage of shale in the Gamma ray data of the well

This step is important both for the offset calculation and the shale gouge calculation. The throw at the base of Rijswijk Member is 40m, the throw at the base Rodenrijs Claystone Mb. is 50 m and the throw at the base of the Delft Sandstone Mb. is 55m (Fig. 26). Based on this information was constructed also the NE side of the fault (right part) which less was known. The construction of the throw window followed the study of Yielding, G. (2002).

Based on Table 3, the highest shale gouge ratio (hence; highest fraction of clay) is found when most of the slipped interval is composed of clay (see point B, table 3). Specifically, the calculations which contain the Rodenrijs Claystone Mb. have the highest value of throw, while shale affects and enhances the slip of the fault. As observed also to the schematic cross – section (Fig. 26), the point B, which corresponds to the

juxtaposition of the claystone layer, has a shale gouge ratio of 70,33%, which quantifies the difference of mainly shale and sand in the slipped intervals, since after point B the throw increases.

4.2 FLAC3D model setup from the geological interpretation

In this chapter will be analyzed the link between the geological interpretation and the setup of the model FLAC3D. The step-by-step analysis contains the conceptualization of the geological outcome of the previous chapters and the simplifications that were necessary to be made (4.3.1.), such as the explanation of the parameters' change for different model scenarios (4.3.2.), the permeability of fault core (4.3.3.) and damage zone scenarios (4.3.4.).

4.2.1 Conceptualization and simplification of the geological interpretation for the FLAC3D model setup

As already mentioned, the scenarios are categorized based on Shale gouge ratio of the fault (SGR %) and the damage zone width.

Table 4. Table of the selected scenarios.

Models	Permeability (K) of the fault core for SGR (s/c%) = 0	Permeability (K) of the fault core for SGR (s/c%) = 60 % (Point C)	Permeability (K) of the fault core for SGR (s/c%) = 50 % (Point D)	Permeability (K) of the fault core for SGR (s/c%) = 40 % (Point E)
Damage zone width= 0	✓	✓	✓	✓
Damage zone Width = 55 m Decreased permeability	✓	✓	✓	✓
Damage zone Width = 55 m Increased permeability	✓	✓	✓	✓

The main decision to model only the throw points C, D and E is based on the position of these points and their relation to the reservoir (Table 4). These are the three points that are referred to the juxtaposition of Delft Sandstone Mb. reservoir. All of them are thrown 55 m, the representative number for the damage

zone width as they measured in the seismic data. The Rodenrijs Claystone Mb. is placed as caprock because of the rock's nature which was modelled as overburden, but it did not participate in the flow simulator. The claystone Mb. was not modelled because it requires revision of the reservoir flow model, which is outside of the scope of this study.

In Figure 27 can be observed the conceptualization and simplification of the model, starting from the throw window measurements until the simplifications from the seismic interpretation and how the model will capture the concept.

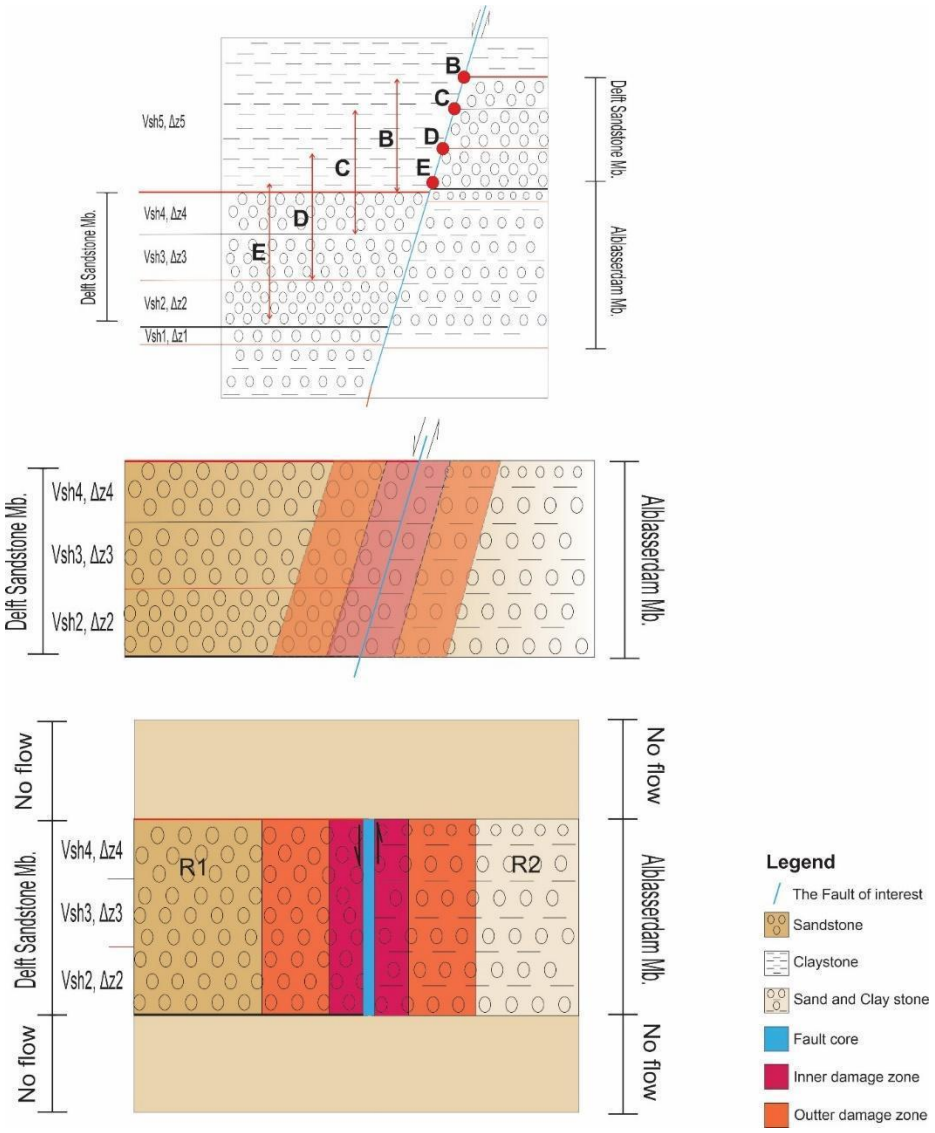

Figure 27. Conceptualization and simplification of the geological interpretation, which is used for setting up the THM – coupled model in FLAC3D – ToughREACT.

The only modelled part will be the two sides of the fault, Delft Sandstone Mb. reservoir (R2) and Alblasserdam Mb. reservoir (R1). The properties of Rodenrijs Claystone Mb. were filled when required in the overburden layer (bulk overburden = 13 x 10^9 Pa, shear overburden = 9.3 x 10^9 Pa; Soustelle et al., Warming Up, 2022). The caprock (claystone) is representing a high impermeable layer which in this study does not facilitate fluid flow. The underburden layer's rock properties correspond to Alblasserdam Mb. as is the underburden stratigraphic layer in the reality (bulk underburden = 3.7 x 10^9, shear underburden = 2.15 x 10^9). Also, the underburden layer does not facilitate fluid flow. Important to remember that there is a line of model symmetry at x=0.

Important to be mentioned that for practical reasons the reservoirs in the modeling are mirrored, i.e., the Delft Sandstone member in the model is located on the right-hand side of the fault whereas on the seismic cross-section it is located on the left-hand side.

4.2.2 Parameters that changed for the fault core.

The thermal expansion corresponds to 8,2 x 10^{-5} °C for Alblasserdam Mb and 9,3 x 10^{-5} °C for Delft Sandstone Mb. (WarmingUp, 2022; Appendix 8.3) for the base case and the heat conductivity and the specific heat are equal to 4,5 Wm^{-1} K^{-1} and 730 J kg^{-1} K^{-1} respectively (Willems et al. 2020).

For the different scenario models the previous values changed for the fault core only as the shale percentage increases in comparison with the reservoirs. The value that was used for the fault core is equal to 950 J kg^{-1} K^{-1} (Crooijmans et al., 2016).

For porosity of the fault core was used the average of the reservoirs' values. The average of the reservoirs' values was used also for the bulk modulus (5 GPa) and the Poisson's ratio value (0,165). For the thermal expansion's value was used the average value of the two reservoirs' values (Soustelle et al., Warming Up, 2022) equal to 8,75 x 10^{-5} °C and for specific heat value equal to 730 J kg^{-1} K^{-1} (Willems et al. 2020).

4.2.3 Permeability of the fault core

The shale gouges' permeabilities in the fault core differ strongly from the surrounding reservoirs. In the case of an increasing shale-gouge ratio percentage all permeabilities were changed to the same value that was interpolated from Crawford (2008) (Fig. 28). The permeabilities from Crawford (2008) were measured fault perpendicular, but in this study, they were applied to all directions. Values for three axes of permeability were filled and the calculations are corresponding to the axes x, y and z.

In the study of Crawford (2008), which was used as an analogue for this study for its experimental work on fault's clay content, for the experiments with clay/quartz rocks Kaolinite was used as a clay mineral. Reuver (1992) in his study makes clear that the clay mineral which coexists with the quartz sandstone (quartz psammites or quartz wackes) in the Delft Sandstone Mb. the reservoir is mostly kaolinite. The Alblasserdam Member, based on the PanTerra report of 2019, is rich to Illite. According to Supandi et al. (2019), for the way Illite and Kaolinite respond in different mechanical experiments, their mechanical properties are slightly different, but this does not affect the results as permeability is not a mechanical property.

The permeability (K) changes of the fault core were based on the shale – gouge ratio values as they calculated in section 4.2.3. (Table 3). For the Delft/Alblasserdam FLAC3D model the values for shale – gouge ratio of the fault core in Delft Sandstone reservoir (R2) are SGR = 60% for point C (measured 56,5 %), SGR = 50% for point D (measured 46,8 %) and SGR = 40% for point E (measured as 39,8 %). Each of them corresponds to a different model scenario.

The grey lines in Figure 28 are corresponding to the percentage of clay material in a "fault core" based on the experiments of the study of Crawford (2008) and their relationship with the effective pressure. The red lines are connecting the calculated effective pressure of this study with the shale – gouge ratio percentages as clay content to find the permeability for the different model scenarios. The 40% and 60% shale – gouge ratio values exist as clay content (red) lines but for the permeability value of 50% clay content will be used the average of 40% and 60% clay content for 31 MPa.

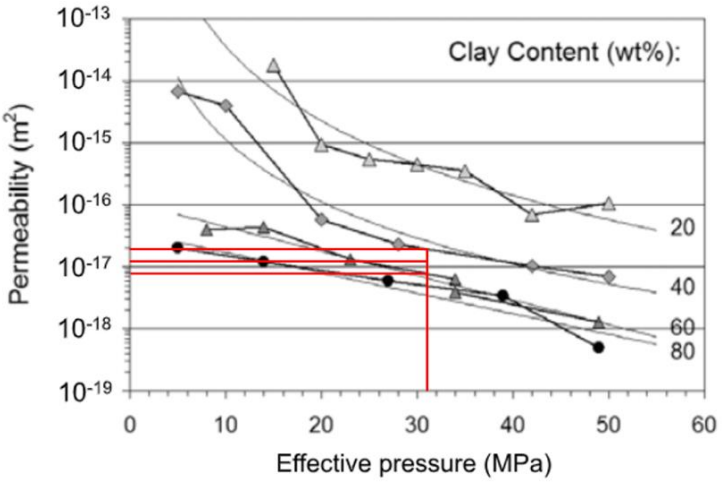

Figure 28. The permeability – effective pressure relationship, graph from the study of Crawford (2008), which was used for calculating the Shale Gouge Ratio (horizontal) permeability.

4.2.4 Damage zones model scenarios

The main property that distinguishes the damage zone from the intact reservoir is the permeability and porosity. However, a lot of studies have different opinions about how the permeability and the porosity of the damage zone changes with respect to the intact host rock. An increasing damage zone permeability was described for granites in Scholz's book (2002), yet, in the study of Evans et. al (1997) are depicted by experimental results as the intensely fractured damaged zone and the increase in permeability (acting as fluid flow channel) in comparison with the lower permeability within the fault core which tends to impede fluid flow across the fault. In the current study it is assumed that the damage zone affects the permeability of the sandstones but is not creating secondary permeability (to enhance the rock's original permeability due to intense fracturing, faults or cavities from dissolution). Specifically for the sandstone rock type, increasing permeability within damage zones is supported (Bossennec et al., 2018) as the damage multiply the cracks, contrasted to decreasing permeabilities results due to the fracturing/compression (Meng et al., 2021) while the high percentage of clay could cement the cracks and decrease the permeability importantly (Schmatz et al., 2010).

For this reason, every model scenario with damage zone width will be modelled two times, one with increased permeability by a factor from the permeability which corresponds to the measured shale – gouge ratio percentage and one with decreased the same way. The chosen factors were based on rough estimations.

Permeability decreases and increases by a factor of 10 in the inner damage zone and by the factor of 3 in the outer damage zone. The different multiplication factors for the inner and outer damage zone were based on the gradient of damage with distance from the fault (Fig. 11/ Chapter 2.5.). Both factors are based on a conservative estimation for sandstones which could range since it depends on rocks properties. The factors could be even higher since the deformation's results are unknown, prohibiting an accurate estimate.

Similarly to the scaling ratio introduced in the literature review chapter 2.5. (Fig. 10), the damage zone (dz) width that will be used is 55 m and it is based on the measured fault offset as explained in the section 4.1.3. (Table 3). The models with dz = 55 m have the fault core values in the center and 55 m damage zone width for each side with 27,5 m inner damage zone and 27,5 m outer damage zone.

In order to determine values for the porosity of Delft and Alblasserdam Members was used the porosity – permeability relationship graph (Fig. 29, PanTerra report, 2019). The calculated increased and decreased permeability values were used to find the porosity from the line of the graph.

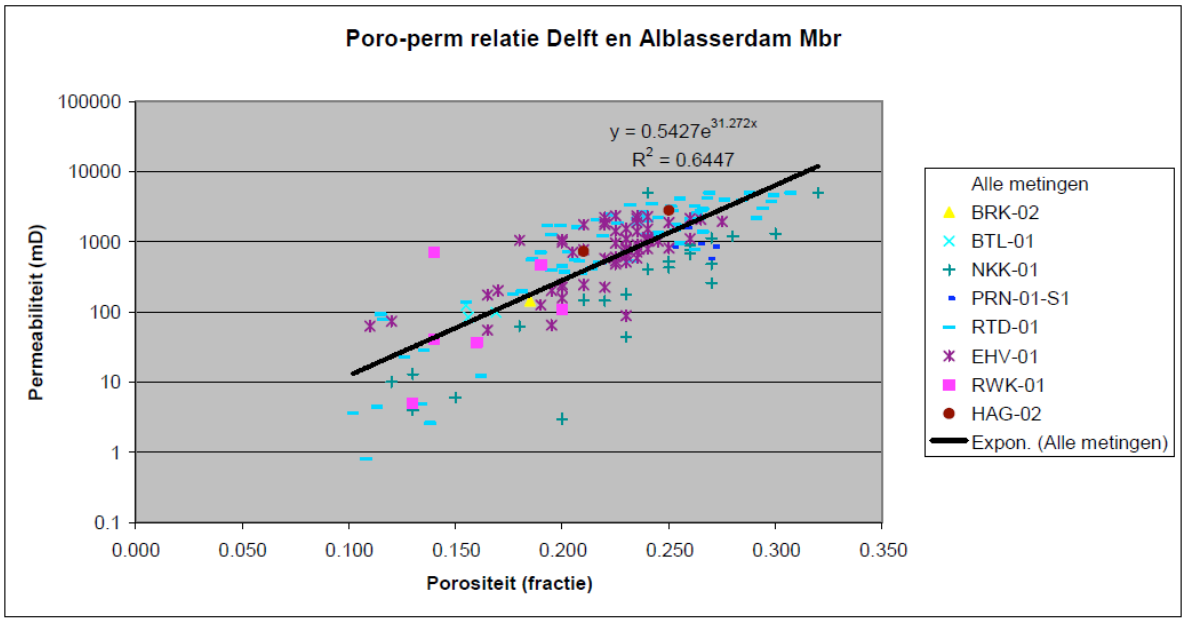

Figure 29. The Porosity – permeability relationship for the Delft and Alblasserdam Members, specifically for the area of interest (PanTerra report, 2019).

Based on the porosity – permeability relationship graph of Figure 29, the porosity values are shown in the following table:

Table 5. Changes in the Permeability for the models with the increased porosity in damage zone and decreased porosity in damage zone.

	Initial Porosity from the base case	Porosity for damage zone (decreased permeability)	Porosity for damage zone (increased permeability)
Fault core	5%	5%	5%
Inner damage zones	-	15%	32%
Outer damage zones	-	20%	29%
Delft Sandstone Mb.	27,7%	27,7%	27,7%
Alblasserdam Mb.	25,3%	25,3%	25,3%

The values of Table 6 are not changing for any of the scenario models with damage zone width and shale – gouge ratio percentage, so it can be used as a reference table for the models' scenarios properties with

width damage zone. For every model scenario of Table 4 exists a different table that can be found in the Appendix section (8.5).

Table 6. Reference table for all the model scenario values for the models with damage zone width and SGR%, except the permeability (for the permeability values see Table 7).

	Initial Pore Pressure	Initial Temperature	Bulk modulus	Poisson ratio	Solid density	Thermal expansion	Heat conductivity	Specific Heat
Fault core	23 MPa	71 °C	5 GPa	0,165	2650 kg/m^3	5 x 10^{-6} °C^{-1}	2.5 W m^{-1} K^{-1}	950 J kg^{-1} K^{-1} (3) (9,5)
Damage zone Alblasserdam Mb. inner			3,7 GPa	0,187		8,2 x 10^{-5} °C^{-1}	4,5 Wm^{-1} K^{-1} (3)	730 J kg^{-1} K^{-1}(3)
Damage zone Alblasserdam Mb. outer			3,7 GPa	0,187		9,3 x 10^{-5} °C^{-1}	4,5 Wm^{-1} K^{-1} (3)	730 J kg^{-1} K^{-1}(3)
Damage zone Delft SSt Mb. inner			6 GPa	0,154		9,3 x 10^{-5} °C^{-1}	4,5 Wm^{-1} K^{-1} (3)	730 J kg^{-1} K^{-1}(3)
Damage zone Delft SSt Mb. outer			6 GPa	0,154		9,3 x 10^{-5} °C^{-1}	4,5 Wm^{-1} K^{-1} (3)	730 J kg^{-1} K^{-1}(3)
Reservoir 1 (Alblasserdam Mb.)			3,7 GPa	0,187		8,2 x 10^{-5} °C^{-1}	4,5 Wm^{-1} K^{-1} (3)	730 J kg^{-1} K^{-1}(3)
Reservoir 2 (Delft SSt Mb.)			6 GPa	0,154		9,3 x 10^{-5} °C^{-1}	4,5 Wm^{-1} K^{-1} (3)	730 J kg^{-1} K^{-1}(3)

When a fault core with a shale gouge ratio is present, for that fault core were used the values presented are results of calculated permeabilities by the scaling factors of 10 for the inner damage zone and 3 of the outer damage zones. These permeability values, with all the model scenarios' permeabilities are visible in Table 7.

Table 7. The permeability values which were used in the model scenarios with damage zone width and SGR%.

		Initial permeability	Decrease for Damage zone 55 m	Increase for Damage zone 55 m
0% SGR	0% SGR Fault Core	5,00 x 10^{-13} m^2 (x) 3,75 x 10^{-13} m^2 (y) 1,00 x 10^{-13} m^2 (z)	5.00 x 10^{-14} m^2 3.75 x 10^{-14} m^2 1.00 x 10^{-14} m^2	5,00 x 10^{-12} m^2 3,75 x 10^{-12} m^2 1,00 x 10^{-12} m^2
	0% SGR Inner dz Delft SSt Mb.	7.00 x 10^{-13} m^2 6.00 x 10^{-13} m^2 1.80 x 10^{-13} m^2	7.00 x 10^{-14} m^2 6.00 x 10^{-14} m^2 1.80 x 10^{-14} m^2	7,00 x 10^{-12} m^2 6,00 x 10^{-12} m^2 1,80 x 10^{-12} m^2
	0% SGR Outer dz Delft SSt Mb.	7.00 x 10^{-13} m^2 6.00 x 10^{-13} m^2 1.80 x 10^{-13} m^2	2.33 x 10^{-13} m^2 2.00 x 10^{-13} m^2 0.60 x 10^{-13} m^2	2,10 x 10^{-12} m^2 1,80 x 10^{-12} m^2 5,40 x 10^{-13} m^2
	0% SGR Inner dz Alblasserdam Mb.	1.49 x 10^{-13} m^2 2.96 x 10^{-13} m^2 0,39 x 10^{-13} m^2	1.49 x 10^{-14} m^2 2.96 x 10^{-14} m^2 0,39 x 10^{-14} m^2	1,49 x 10^{-12} m^2 2,96 x 10^{-12} m^2 0,39 x 10^{-12} m^2
	0% SGR Outer dz Alblasserdam Mb.	1.49 x 10^{-13} m^2 2.96 x 10^{-13} m^2 0,39 x 10^{-13} m^2	4.97 x 10^{-14} m^2 9.87 x 10^{-14} m^2 0,13 x 10^{-13} m^2	4,47 x 10^{-13} m^2 8,88 x 10^{-13} m^2 1,17 x 10^{-13} m^2
40% SGR	40% SGR Fault Core	1,90 x 10^{-15} m^2 1,90 x 10^{-19} m^2 1,90 x 10^{-19} m^2	1,90 x 10^{-16} m^2 1,90 x 10^{-20} m^2 1,90 x 10^{-20} m^2	1,90 x 10^{-14} m^2 1,90 x 10^{-18} m^2 1,90 x 10^{-18} m^2
	40% SGR Inner dz Delft SSt Mb.	7.00 x 10^{-13} m^2 6.00 x 10^{-13} m^2 1.80 x 10^{-13} m^2	7.00 x 10^{-14} m^2 6.00 x 10^{-14} m^2 1.80 x 10^{-14} m^2	7,00 x 10^{-12} m^2 6,00 x 10^{-12} m^2 1,80 x 10^{-12} m^2
	40% SGR Outer dz Delft SSt Mb.	7.00 x 10^{-13} m^2	2.33 x 10^{-13} m^2	2,10 x 10^{-12} m^2

		6.00×10^{-13} m^2 1.80×10^{-13} m^2	2.00×10^{-13} m^2 0.60×10^{-13} m^2	$1,80 \times 10^{-12}$ m^2 $5,40 \times 10^{-13}$ m^2
	40% SGR Inner dz Alblasserdam Mb.	1.49×10^{-13} m^2 2.96×10^{-13} m^2 $0,39 \times 10^{-13}$ m^2	1.49×10^{-14} m^2 2.96×10^{-14} m^2 $0,39 \times 10^{-14}$ m^2	$1,49 \times 10^{-12}$ m^2 $2,96 \times 10^{-12}$ m^2 $0,39 \times 10^{-12}$ m^2
	40% SGR Outer dz Alblasserdam Mb.	1.49×10^{-13} m^2 2.96×10^{-13} m^2 $0,39 \times 10^{-13}$ m^2	4.97×10^{-14} m^2 9.87×10^{-14} m^2 $0,13 \times 10^{-13}$ m^2	$4,47 \times 10^{-13}$ m^2 $8,88 \times 10^{-13}$ m^2 $1,17 \times 10^{-13}$ m^2
50% SGR	***50% SGR Fault Core***	$1,30 \times 10^{-15}$ m^2 $1,30 \times 10^{-19}$ m^2 $1,30 \times 10^{-19}$ m^2	$1,30 \times 10^{-16}$ m^2 $1,30 \times 10^{-20}$ m^2 $1,30 \times 10^{-20}$ m^2	$1,30 \times 10^{-14}$ m^2 $1,30 \times 10^{-18}$ m^2 $1,30 \times 10^{-18}$ m^2
	50% SGR Inner dz Delft SSt Mb.	7.00×10^{-13} m^2 6.00×10^{-13} m^2 1.80×10^{-13} m^2	7.00×10^{-14} m^2 6.00×10^{-14} m^2 1.80×10^{-14} m^2	$7,00 \times 10^{-12}$ m^2 $6,00 \times 10^{-12}$ m^2 $1,80 \times 10^{-12}$ m^2
	50% SGR Outer dz Delft SSt Mb.	7.00×10^{-13} m^2 6.00×10^{-13} m^2 1.80×10^{-13} m^2	2.33×10^{-13} m^2 2.00×10^{-13} m^2 0.60×10^{-13} m^2	$2,10 \times 10^{-12}$ m^2 $1,80 \times 10^{-12}$ m^2 $5,40 \times 10^{-13}$ m^2
	50% SGR Inner dz Alblasserdam Mb.	1.49×10^{-13} m^2 2.96×10^{-13} m^2 $0,39 \times 10^{-13}$ m^2	1.49×10^{-14} m^2 2.96×10^{-14} m^2 $0,39 \times 10^{-14}$ m^2	$1,49 \times 10^{-12}$ m^2 $2,96 \times 10^{-12}$ m^2 $0,39 \times 10^{-12}$ m^2
	50% SGR Outer dz Alblasserdam Mb.	1.49×10^{-13} m^2 2.96×10^{-13} m^2 $0,39 \times 10^{-13}$ m^2	4.97×10^{-14} m^2 9.87×10^{-14} m^2 $0,13 \times 10^{-13}$ m^2	$4,47 \times 10^{-13}$ m^2 $8,88 \times 10^{-13}$ m^2 $1,17 \times 10^{-13}$ m^2
60% SGR	***60% SGR Fault Core***	$7,00 \times 10^{-16}$ m^2 $7,00 \times 10^{-20}$ m^2 $7,00 \times 10^{-20}$ m^2	$7,00 \times 10^{-17}$ m^2 $7,00 \times 10^{-21}$ m^2 $7,00 \times 10^{-21}$ m^2	$7,00 \times 10^{-15}$ m^2 $7,00 \times 10^{-19}$ m^2 $7,00 \times 10^{-19}$ m^2
	60% SGR Inner dz Delft SSt Mb.	7.00×10^{-13} m^2 6.00×10^{-13} m^2 1.80×10^{-13} m^2	7.00×10^{-14} m^2 6.00×10^{-14} m^2 1.80×10^{-14} m^2	$7,00 \times 10^{-12}$ m^2 $6,00 \times 10^{-12}$ m^2 $1,80 \times 10^{-12}$ m^2
	60% SGR Outer dz Delft SSt Mb.	7.00×10^{-13} m^2 6.00×10^{-13} m^2 1.80×10^{-13} m^2	2.33×10^{-13} m^2 2.00×10^{-13} m^2 0.60×10^{-13} m^2	$2,10 \times 10^{-12}$ m^2 $1,80 \times 10^{-12}$ m^2 $5,40 \times 10^{-13}$ m^2
	60% SGR Inner dz Alblasserdam Mb.	1.49×10^{-13} m^2 2.96×10^{-13} m^2 $0,39 \times 10^{-13}$ m^2	1.49×10^{-14} m^2 2.96×10^{-14} m^2 $0,39 \times 10^{-14}$ m^2	$1,49 \times 10^{-12}$ m^2 $2,96 \times 10^{-12}$ m^2 $0,39 \times 10^{-12}$ m^2
	60% SGR Outer dz Alblasserdam Mb.	1.49×10^{-13} m^2 2.96×10^{-13} m^2 $0,39 \times 10^{-13}$ m^2	4.97×10^{-14} m^2 9.87×10^{-14} m^2 $0,13 \times 10^{-13}$ m^2	$4,47 \times 10^{-13}$ m^2 $8,88 \times 10^{-13}$ m^2 $1,17 \times 10^{-13}$ m^2

4.3.1. 3D spatial distributions of P and T, after 2 years of injection

In this chapter the FLAC3D-ToughREACT model results will be presented. The presented model results concern the effect on temperature and pore pressure at the end of the injection of cold water.

The results of this chapter correspond to the end of the injection time. Here, are going to be analysed only the 0% SGR and 60% SGR as the extreme cases. The results for 40% and 50% SGR are shown in the Appendix (8.6). The 0% and 60% SGR model scenarios include the scenarios for no damage zone, damage zone with increased permeability and damage zone with decreased permeability.

The effect on temperature at the end of the injection for 0% SGR and 60% SGR with no damage zone is visible in Figure 30. Even without damage zone width, the SGR% has a strong effect on the temperature distribution which is almost symmetric and a fault core open to flow. In the 0% SGR result can be seen also the effect of the different rock properties on the reservoirs' rock (Alblasserdam sandstone in contrast with the Delft Sandstone Member with higher concentration in sand). However, the 60% SGR works as a

barrier for the temperature on the reservoir while temperature is “blocked” by the fault core on the reservoir’s side.

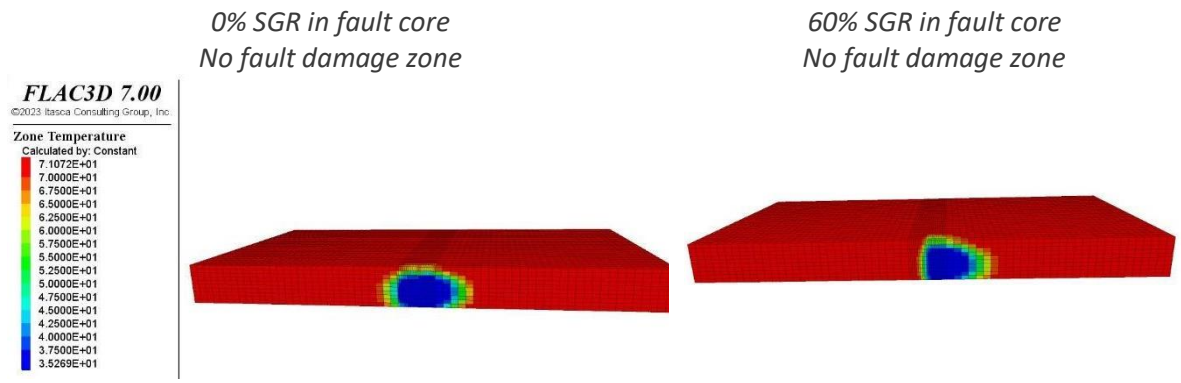

Figure 30. FLAC3D model results which compare the effect on the temperature of the reservoir on the base case (0% SGR, no fault damage zone) with the 60% SGR model scenario without damage zone.

According to the results shown in Fig. 31, for the 60% SGR the flow remains “blocked”, with cooling to be concentrated close to the injector. On the increased permeability for both 0% SGR and 60% SGR, the flow/cooling is distributed along the fault.

The large thermal changes (~ 35^{o}C), especially the extreme cooling of the caprock can cause the failure of the caprock, as the extreme cooling increases the stresses. However, the stresses in the caprock have not been studied. For this, the model needs to be adapted (by allowing flow in the caprock formation).

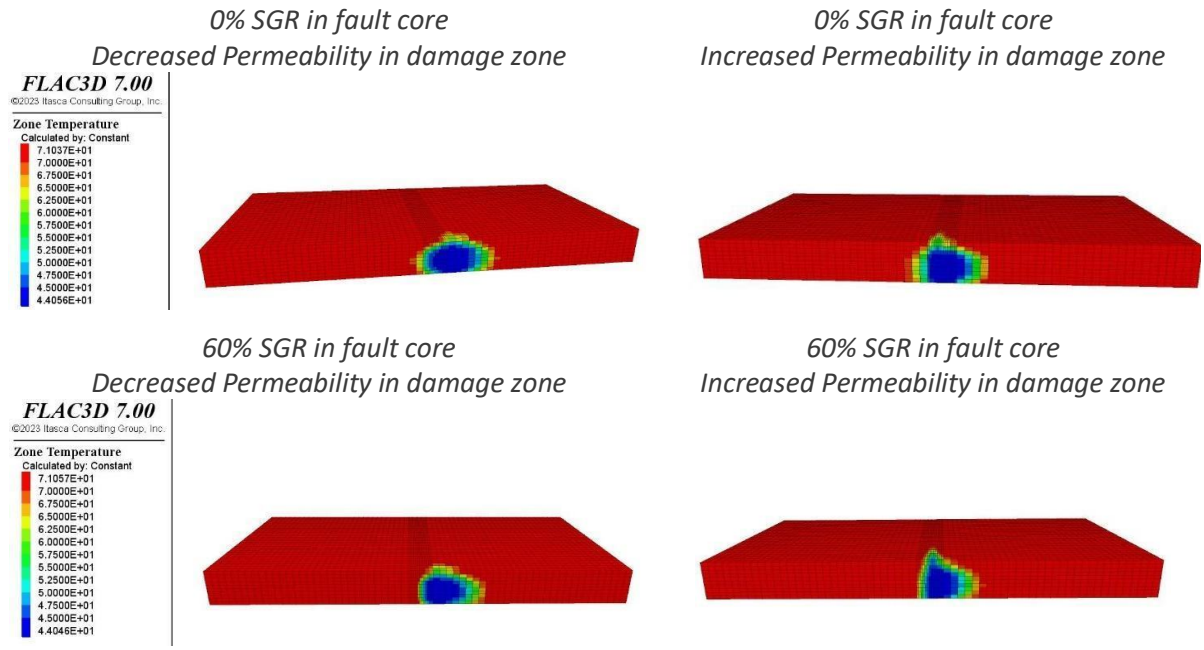

Figure 31. FLAC3D model results which compare the effect on the temperature of the reservoir on the base case (0% SGR) with the 60% SGR model scenario with decreasing and increasing permeability in the damage zone.

Temperature results (Fig. 30 & 31) are in agreement as can be seen in the results shown in Figures 32 & 33. The patterns on the pore pressure follow the temperature pattern and the increase is closer to the position of the injector, as expected. The pore pressure difference in Figure 32 confirms the huge effect of the shale inside the fault core. In the 0% SGR pore pressure result, which corresponds to the base case, is visible the effect of the different rock properties on the reservoirs' rock (as in Figure 30). The different rock types differentiate in the reservoirs' properties and results in relatively different pore pressure among the two reservoirs. For 60% SGR, the pressure is isolated on the side of the injector by the 60% SGR fault core (similarly to the temperature in Figure 30).

If we compare the simulations of the 0% SGR with the 60% SGR, then it is observed that the SGR percentage even without damage zone has a significant effect on the pressure that is concentrated in the reservoir of interest.

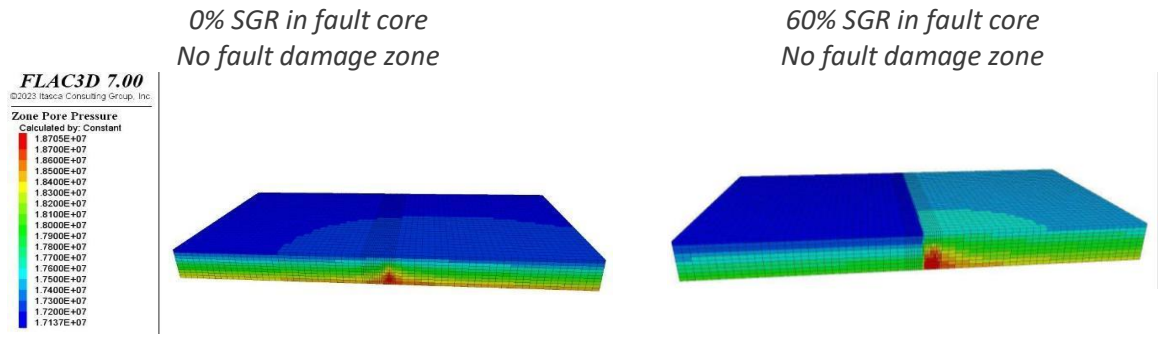

Figure 32. FLAC3D model results which compare the effect on the pore pressure of the reservoir on the base case (0% SGR, no fault damage zone) with the 60% SGR model scenario without damage zone.

Diving deeper into the results with a damage zone, the spatial distributions are becoming more complex (Fig. 33). The decrease in the permeability in the damage zone (Fig. 33) concentrates the pressure in the reservoir even if the SGR% in the fault core does not exist and decreased permeability damage zones burden the effect of SGR% fault core on pressure. For the 60% SGR, with decreased damage zone's permeability, the pore pressure inside the reservoir with the injector is rather high. On the other hand, the increased permeability in the damage zone scenarios, for both 0% and 60% SGR, "relaxes" significantly the pore pressure in the reservoir (Fig. 33). The increase in the permeability inside the damage zone seem to barely increase the pore pressure inside the reservoir and mitigates the effect of SGR% fault core for both 0% and 60% model scenarios. The pore pressure is relatively uniformed distributed compared to the decreased permeability damage zones, that even in the case of 60% SGR the system seems to have lower pressure than the 0% SGR with decreased permeability in the damage zone. However, the 60% SGR with

increasing permeability in the damage zone has more distinct fault core than the 0% SGR with decreased permeability.

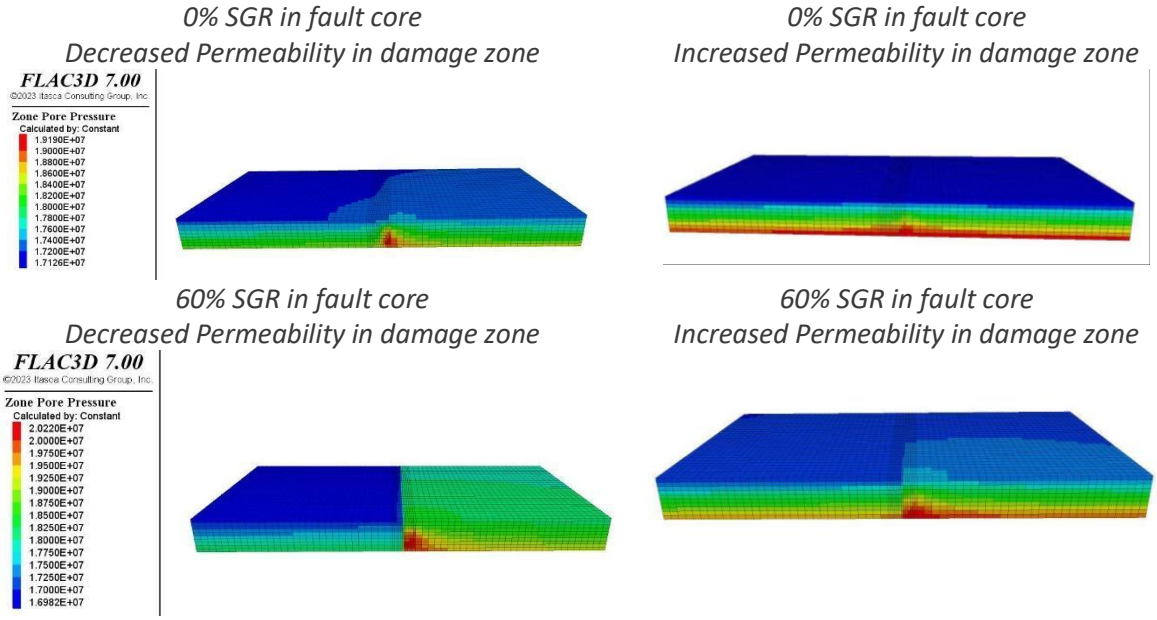

Figure 33. FLAC3D model results which compare the effect on the pore pressure of the reservoir on the base case (0% SGR) with the 60% SGR model scenario with decreasing and increasing permeability in the damage zone.

4.3.2. Temperature, pressure and stress distribution along the fault

In the current sub-chapter will be analysed the temperature (T), pressure (P) and stress distributions along the fault. Python was used to calculate the stresses and visualize the P, T and stress distributions along the fault, after 2 years of injection.

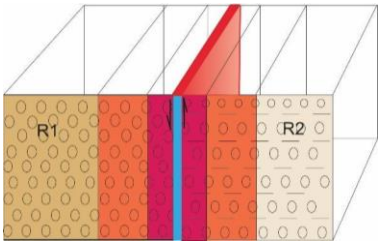

Figure 34. Schematic representation of the plane x=0, which corresponds to the fault plane. The x=0 is the position of the obtained results.

For the stress interpretation, we used the ratio of the maximum principle shear stress to the normal effective stress acting on the plane of the maximum principle shear stress. These stress measures were derived from the simulated stress tens, or and pore pressure. To do so, the stress tensor for each mesh cell in the model was rotated to obtain the principal stress tensor. The maximum principal shear stress was then given as half the difference between the largest and smallest principal stresses, and the effective normal stress as half the sum of the largest and smallest principal stresses minus the pore pressure. To discuss the effect on temperature, pore pressure and stresses (Shear stress/Normal stress ratio) in the end of injection along the fault, the results from the FLAC3D-ToughREACT model were studied from the position x=0 along the y-axis. This corresponds to the fault plane (Fig. 34). For this reason, the start of the

presented results' graph (x=0, y=0) is the closest point to the injector, while the injecting occurs along a line segment that goes from (x=0, y=0, z=z_1) to (x=0, y=0, z=z_2). For all the SGR% results in two different planes, where a plane running parallel to the y-axis, intersecting the x-axis at x=0, and similarly for x-axis intersecting the y-axis at y=0 (see Appendix 8.6).

In Figure 35, the temperature distribution in comparison with the pore pressure along the fault have the same spatial trend. The main changes are closer to y=0, while this is the position of the injector. For the 60% SGR, the temperature change is distributed over a large area along the fault, while the shale acts as a barrier to fluid flow and consequently blocks the temperature distribution (Fig. 30). By comparing the two extreme cases (0% and 60% SGR, Fig. 35), for the 60% SGR the stress ratio's spatial distribution seems to be closer to the injector. For the base case, the stress change is distributed in a larger area than the 60% SGR.

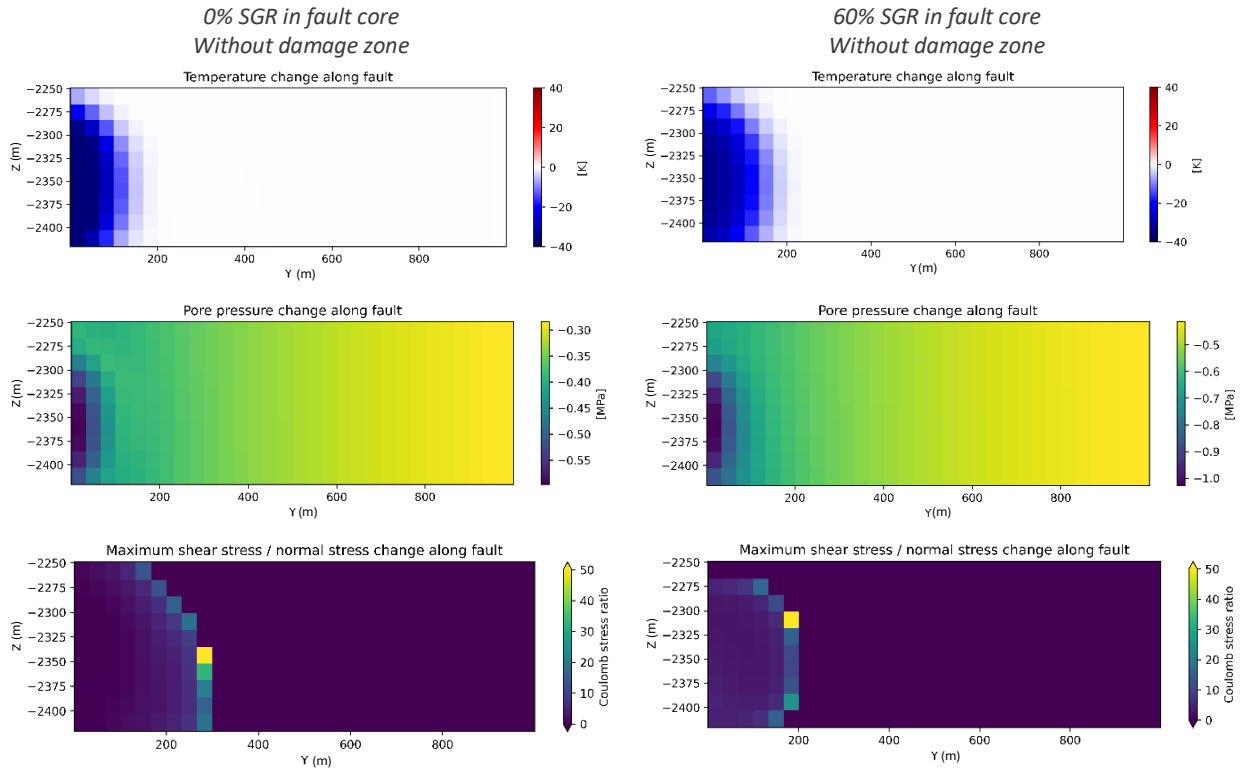

Figure 35. Comparison of 0% SGR (base case) and 60% SGR without damage zone cases on temperature, pore pressure and stress distribution along the fault.

The increase or decrease of the permeability inside the damage zone seem to change the spatial distribution even for model scenarios without shale in the fault core (Fig. 36). Along the fault, the decreased permeability concentrates the spatial distribution of temperature and pore pressure changes closer to the injector in comparison to the increased permeability. This distribution leads to higher stress

build up close to the injector (200 m from the injector, Fig. 36). For the increased permeability in the damage zone, the stress ratio is observed further on the plane but follows the pattern of the temperature and pore pressure changes.

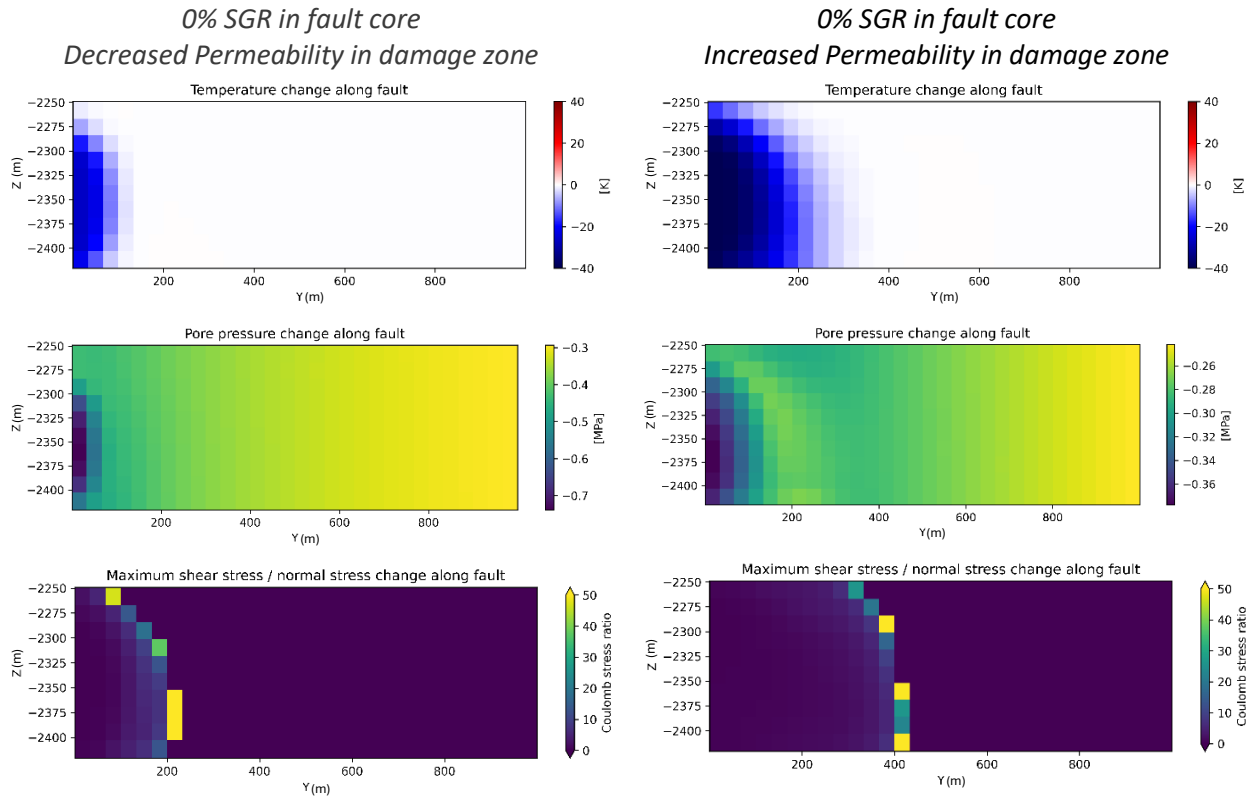

Figure 36. Comparison decreased and increased permeability inside the damage zone cases in 0% SGR in the fault core on temperature, pore pressure and stress distribution along the fault.

The 60% SGR model scenario in comparison to 0% model scenario (Fig. 36), in the decreased permeability damage zone, the spatial distribution is way closer to the injector while for the increased permeability damage zone, temperature, pore pressure and stress ratio changes distributed in larger area along the fault (Fig. 37). Comparing the decreased and increased permeability scenarios for 60% SGR, in the increased permeability damage zone, the temperature, pore pressure and stress changes are distributed further from the injector along the fault (Fig. 37). Meanwhile, the decreased permeability damage zone concentrates the temperature, the pore pressure and the stress ratio change even closer to the injector than the 0% SGR model scenario (Fig. 36 & 37). This concentration in the decreased permeability damage zone leads to high stress build up close to the injector (~100 m away from the injector, Fig. 37).

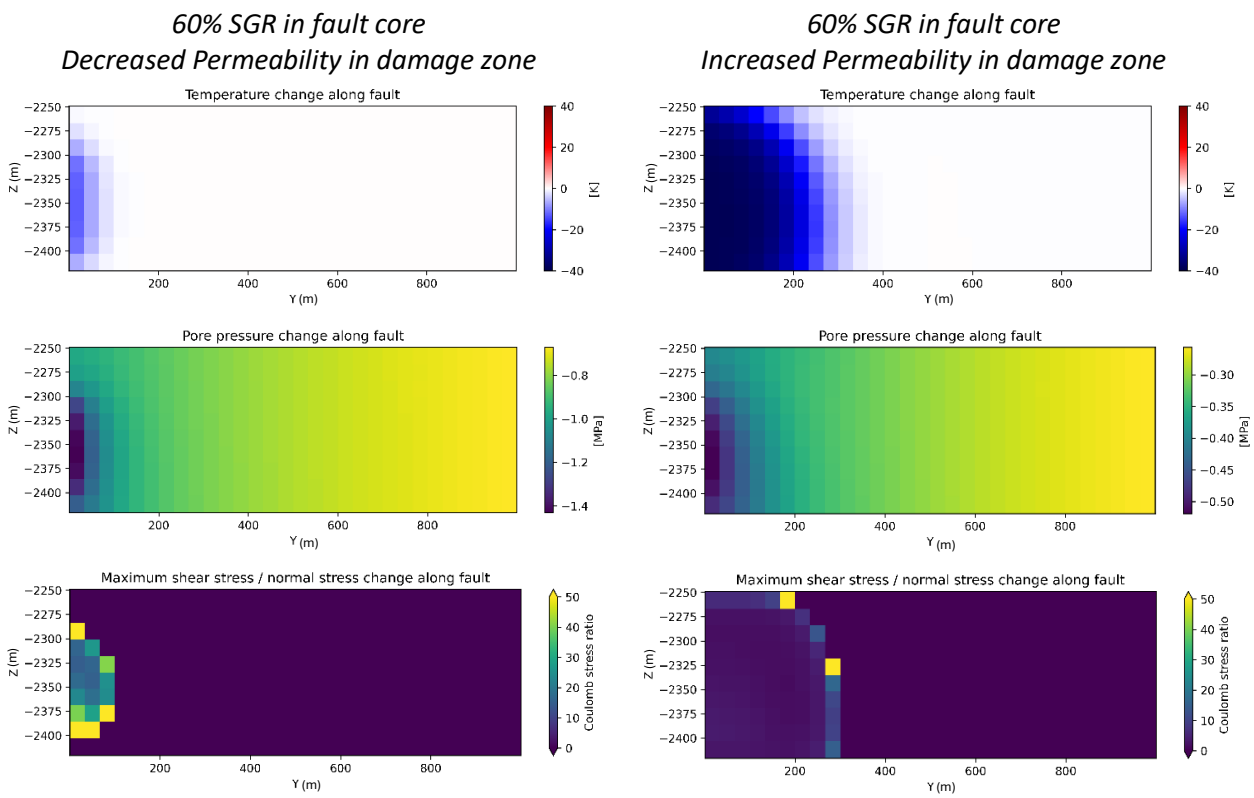

Figure 37. Comparison decreased and increased permeability inside the damage zone cases in 60% SGR in the fault core on temperature, pore pressure and stress distribution along the fault.

4.3.3. Temporal evolution of P and T on the fault

Results of time evolution for the two extreme scenarios of the base case and the 60% SGR/damage zone model scenario will be presented too.

Time evolution results give an insight about the temperature and pore pressure evolution over time. In Figure 36 are presented the results of two locations, y = 50 m and y = 200 m away from the injector, with the curves corresponding to different model scenarios (i.e. blue presents always the base case in Fig. 38). The cooling seems to move further with time (difference in y = 50 m and y = 200m) while comparing the two positions, the temperature of y = 50 m stabilized around 1. 50 years when the y = 200 m remains ~70^{o}C and cooling starts after ~ 1.25 years, except for the 60% SGR with increased permeability damage zone model scenario (Fig. 38). The flat trend corresponds to the stabilization of temperature in the model, and the 0% SGR without damage zone seems to be stabilized faster in time, compared to the 60% SGR without damage zone scenario model. For the scenarios with a damage zone, either with increasing or decreasing permeability, we observe similar trends to scenarios without damage zone, but with different time periods to reach stabilization: A decrease in damage zone permeability leads to slower cooling than the base case (Fig. 38) while the increasing permeability damage zone follows the base case trend but

cooling faster. The same occurs for the decreasing/ increasing permeability of damage zone for the 60% SGR model scenarios. However, on the y = 200 m position it seems that the decreased permeability damage zone model scenario remains stable and the base case too, while the increasing permeability scenario getting cooler faster.

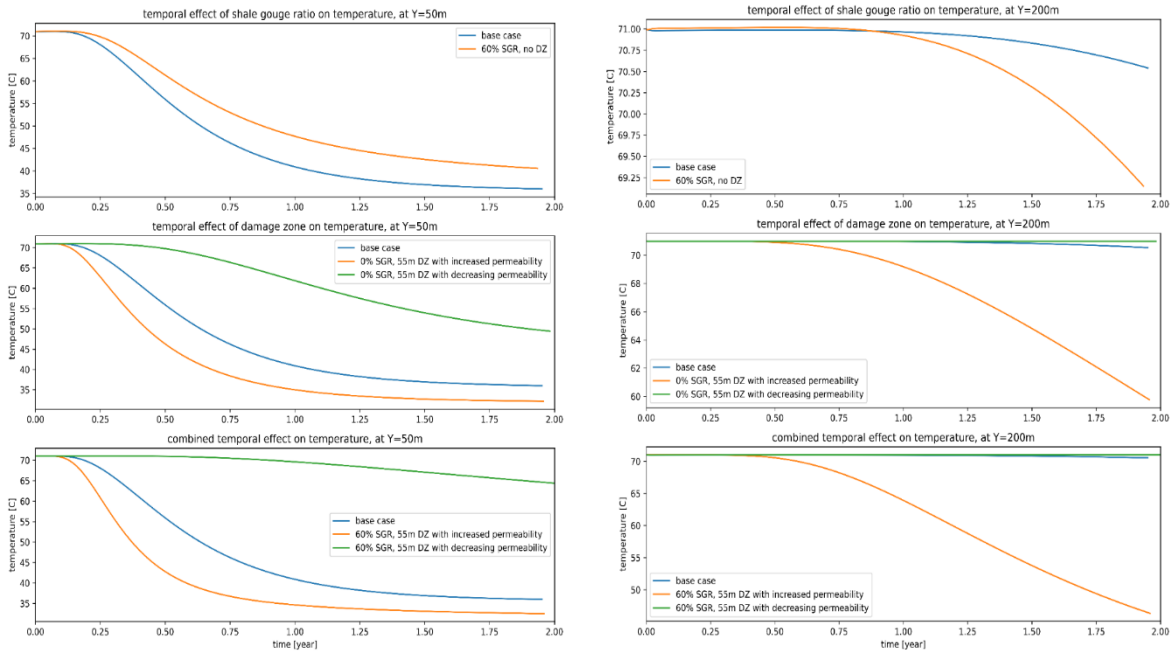

Figure 38. Time evolution the SGR% effect on temperature results for the y=50m position (50 m far from the injector) and y=200m (200 m far from the injector). The graphs are for no damage zone (first line), for increased and decreased permeability inside the damage zone for 0% SGR in the fault core (second line) and for the increased and decreased permeability inside the damage zone for 60% SGR in the fault core (third line).

Figure 39 displays the pore pressure over time along the fault for the positions 50 m, 100 m, 200 m, 300 m and 500 m away from the injector. The 0% SGR (base case) and 60% SGR model scenarios are compared, both without damage zones. Minor differences are observed from 0% SGR to 60% SGR. For both cases, the pressure stabilizes quickly. In the middle panels of Figure 39, a zoom-in at 1.2 months is shown, to show the stabilization moment.

For both cases, the pressure stabilized very fast and remained stable, even from the first ~13 days (0.035 yrs), with minor differences from 0% SGR to 60% SGR.

Base case *60% SGR*

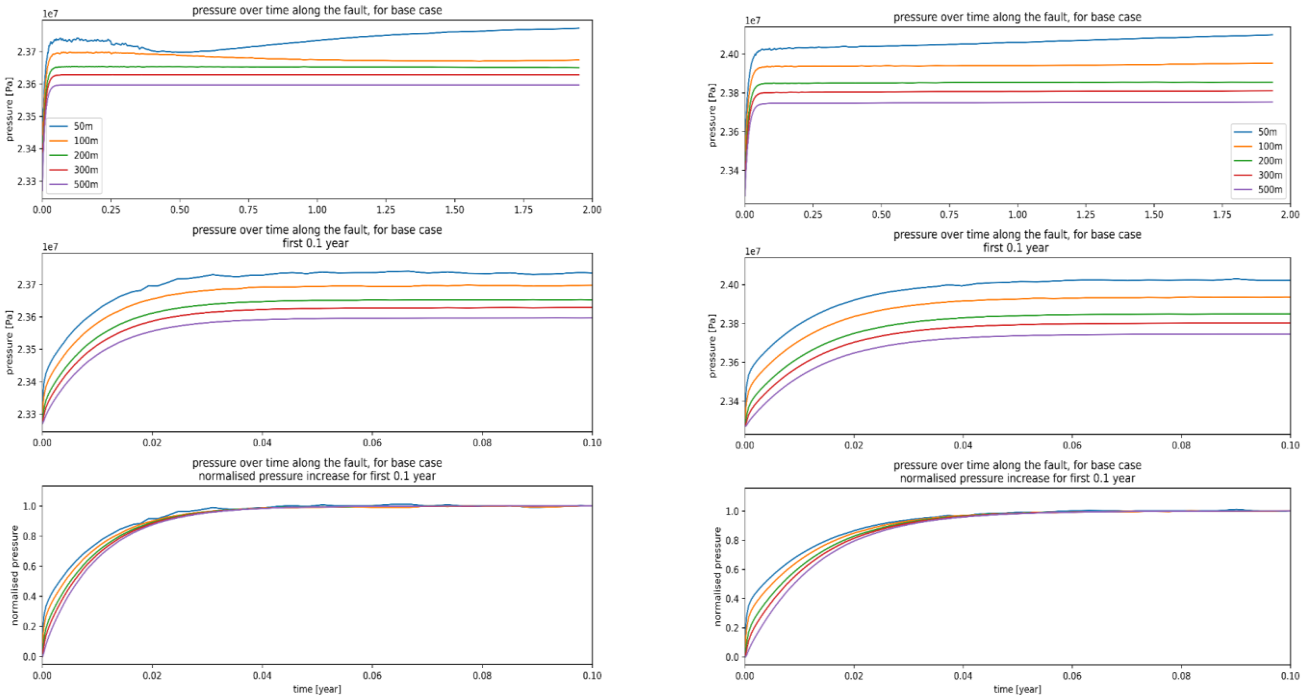

Figure 39. Comparison of the 0% SGR (base case) and 60% SGR, both with no damage zone on the pressure over time along the fault for the positions 50 m, 100 m, 200 m, 300 m and 500 m far from the injector (first line). Also, visible the pressure over time along the fault for the first 0.1 year (second line) and the normalized results of this graphs (third line).

5 Discussion

In this chapter will be discussed the results and the overall study and the challenges its conduction. An overall discussion of the tectonic evolution of the area (5.1.) will be followed by the temperature, pressure and stresses distribution results' discussion (5.2.). The limitations and simplifications that occurred will be discussed in the subchapter 5.3.

5.1 The tectonic evolution

The interpretation of the time thickness maps led the tectonic evolution reconstruction. The thickness maps gave the opportunity of an overall review of the stratigraphy and tectonic evolution. The existence of structural elements, though variations, exist in terms of precise locations, outlines, and structural interpretations. The complex burial history, which coexists with the structural evolution, stands challenging for the interpretation of the interval thicknesses.

Based on the age of the reservoir's sediments, the tectonic structures are normal faults as the faults moved as normal in the syn – rift period of Late Jurassic. The thickness changes from NW to SE are not controlled by grabens. The normal faults of NW – SE direction cut the surface of Delft Sandstone Mb. causing the tectonic complexity of the reservoir and confirm the importance of this study.

The main observations on the Early Jurassic thickness map (Fig. 17) are the normal faults of NW – SE direction. On the thickness map of Late Jurassic (Fig. 18 & 19), the visible normal faults on the map are the continuation of the previously seen normal faults that were active until the end of the rift. It is normal that they have different appearance from the previous map, while the faults can slightly change orientation, especially in this case where sedimentation occurs, while they have similar topographic changes/ thickness differences. This observation leads to the interpretation of the age and movement of the faults. The Early Jurassic's faults are characterized by NW – SE direction of normal faults which corresponds to the start of the rift while the Late Jurassic's normal faults correspond to a syn – rift phase where the direction of the faults slightly change. As it can be seen on the time thickness map of Delft Sandstone Member and the Alblasserdam Member (Fig. 18), the closest to the west side of the map and on the middle of the map, thicker horizons are next to normal faults that were re-activated as reverse faults later by the inversion. This outcome arises from the interpretation of their kinematic history and the thickness of the sediments around them, which thickness is also visible on the thickness map (Fig. 18). This supports the assumption that compression occurred after the syn – rift phase, caused by the inversion

of Late Cretaceous. However, on the time thickness map the faults are interpreted as normal faults while they were created as normal faults on the syn – rift phase. The rest of the interpreted faults were generated as normal faults and buried after the end of the Jurassic's rift. As the last sedimentation of the syn – rift phase of the Late Jurassic was identified the Rodenrijs Claystone Member (Fig. 19). Some of the Rodenrijs Claystone Member's faults that are not visible in the thickness map were buried during the sedimentation of the Claystone Member.

During the post – rift phase, the Early Cretaceous' sedimentation occurs. Normal faults can be observed in Figure 20 & 21. The Early Cretaceous sedimentation and tectonic history correspond to post – rift phase. The post – rift phase in a chronical sequence is before the reverse tectonic phase which means that the main "reverse" faults of the Figure 20 & 21's are normal faults of Early Cretaceous which were reactivated as reverse faults. Comparing the Early part of Early Cretaceous (Vlieland Formation, Fig. 20) to the Late part of Early Cretaceous (Upper and Lower Holland Formations, Fig. 21), the direction of the formed faults on Early part of Early Cretaceous continues in the later age of Holland Formations, giving, however, a more linear impression (Fig. 21). This observation leads to the interpretation that the multiple faults of less linear impression of the Early part of the Early Cretaceous were merged into less faults on the Later age. Another option could be that the faults of the Early part were buried until the later part of Early Cretaceous. Many faults from the earlier part of the Early Cretaceous (Vlieland formation/ Fig. 20) disappear in the late part of Early Cretaceous (Upper and Lower Holland Formations/ Fig. 21). The late part of the post – rift Early Cretaceous' tectonic stage leads to the conclusion that with the evolution of time and going closer to the end of Early Cretaceous, the tectonic complexity is becoming simpler.

During the Late Cretaceous, the observed faults interpreted as reversed. The inversion reactivated the normal faults of the Holland Formations (as they are visible in the thickness map of the Late part of Early Cretaceous, Fig. 21), while they were observed inversed and slightly altered or combined in the thickness map of Late Cretaceous (Fig. 22). This is the main reason why they interpreted as reversed faults in the thickness map of the Late part of Early Cretaceous, even if they are originally normal (as referred already).

Diving deeper on the seismic cross – section analysis (Fig. 23b), the idea of the normal faults that reactivated as reversed is confirmed. The analyzed horizons and the image of the previously existed normal faults are all of them clearly affected by the Late Cretaceous' inversion. The anticlines (uplifts) and synclines are strong indicators of the inversion.

For the better understanding of the reader, the already interpretation's data combined in an easier way to correlate the ages, and the time thickness maps with the tectonic evolution. Important information about the tectonic events were obtained while analyzing the seismic cross – section (Fig. 23b), which helped to the reconstruction of the tectonic events' sequence. Focusing on the ages between Jurassic and until Cenozoic, a conceptual sketch (Fig. 40) presents the estimated tectonic evolution of the area of interest in the WNB, in which are summarized the basic structures, formations and sediment horizons. In Figure 40, can be observed step by step, in a geological time frame, the details of the already analyzed events by the literature and the seismic interpretation.

The tectonic evolution's sketch from Late Jurassic until after Late Cretaceous was created based on the seismic cross – section that gave most of the data that were analyzed for the aim of this study. It is, also, visible in the position of the well of the geothermal doublet as a reference point for the evolution of the area.

The Lower Cretaceous sedimentation is characterized by a marine depositional environment, co – existing with the post – rift's phase normal faults (see chapter 2.2.) Based on this, the accommodation space was proper for the basin infill, which completed in later ages and before the inversion. The sedimentation closer chronically to the inversion (Chalk Group) is visible on the seismic cross – section of Figure 24 as onlaps which indicate transgression, giving information about the post – rift depositional environment before the inversion phase.

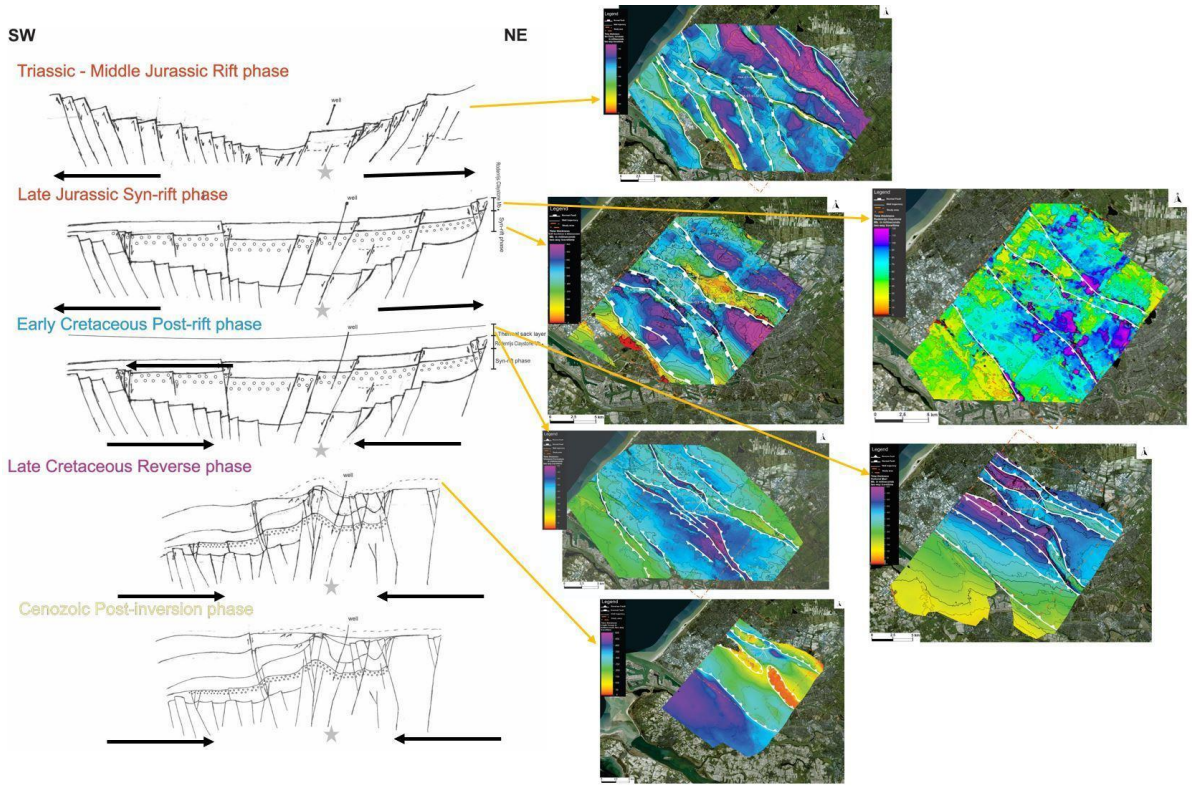

Figure 40. a) Tectonic evolution from Triassic-Middle Jurassic Rift phase until after Late Cretaceous. The colours of the titles correspond to the colours of the faults in the interpreted seismic line, connecting their kinematic and genesis to the age of the tectonic events. b) The corresponding to its ages and tectonic events time thickness maps of the Stratigraphic Groups and Members. Marked with starts are the faults on both sides of the well for better navigation between the images. The brown – yellow star's fault will be used for the model later (FOI).

The model was based on a fault which cuts and offsets the Delft Sandstone Member reservoir, and it is visible close to the well on the time surface map of the reservoir (Fault A, Fig. 16).

The expansion index ratio of the fault of interest (FOI) never becomes zero (0) which leads to the conclusion that the fault was active during all the sedimentation in Early Cretaceous (post – rift phase) until it was completely buried. However, in comparison with the faults that were reactivated multiple times, the FOI is a relatively simple one.

Concerning the impact of the SGR% in more complex (normal who became reverse) reactivated faults with larger throws, further research should be conducted. Shale distribution changes in comparison to a normal fault while the primarily throw's gouge disperses differently due to reactivation and inversed movement. Damage zone scaling factors should increase while inversion's damage should deteriorate the primarily rift's damage. Ultimately permeability values would extremely increase or decrease, creating a scopus for a new research question in order to answer these uncertainties.

5.2 Distribution of pressure, temperature and stresses

It is important to discuss that the damage zone in the models that exist is modelled as inner damage zone (change in base case's permeability by a factor of 10) and outer damage zone (changes in base case's permeability by a factor of 3). Damage zone's separation was based on the idea that formations cannot be equally deformed in a damage zone as warding off from the fault. Therefore, the width of the damage zone was decided after the geology interpretation and calculations of the shale – gouge ratio.

Pore pressure's spatial distribution reveals that the fault core with high SGR can lead to high risk of the reservoir. The high percentage of SGR (60% shale gouge ratio case, Fig. 32) leads on pressure compartmentalization. The high concentration of pore pressure could be crucial for the geothermal activities while the reservoir's caprock could collapse. For the damage zone cases, the permeability-decreasing damage zone burdens the impact of SGR% and results to stronger pressure compartmentalization (Fig. 33), threatening the caprock more than the 60% SGR case (without damage zone, Fig. 32) and increase the seismicity risks. However, a permeability-increasing damage zone mitigates the effect of a high SGR% (Fig. 33).

The results of the distribution along the fault reveal that, comparing the temperature distribution with the pore pressure results, temperature and pore pressure are highly depended on each other as they have the same spatial trend. For the 0% SGR permeability changes (Fig. 35), the pressure changes lead to temperature changes. The stress distribution along the fault follows the pattern of the temperature and pore pressure.

The stress ratio of shear/normal stress seems to be higher where the temperature difference starts (end of cool plume) with this difference to increasing the stress. The pore pressure follows similar pattern, leading to the results that both temperature and pore pressure have effect to the stress ratio but also are highly depended on each other. The 60% SGR and the 0% SGR with damage zones model scenarios (Fig. 36 & 37) follows the same trend on temperature, pore pressure and stress ratio with the difference that the 60% SGR model scenario gives more extreme results of the 0% SGR model scenario's observations.

The effect of the SGR% in a defined fault core should attract more attention as the increasing percentage of shale increases the isolation of the temperature change on the one side of the fault. The shale isolates the advection, and the diffusion of pressure and temperature are remaining to the side of the injector. Since pore pressure gives stress to the system, it is considered as a link with the stress distribution.

Diffusion of cold fluid creates advection of cold water in a hot reservoir. The pore pressure increases to this contact while the convection circulation since the material shrinking from cold, creating increase of stress in the borders of the plume.

A model with Delft Sandstone's specifically heat conductivity and specific heat capacity (also derived from Delft Sandstone's properties) would give an insight about the stress distribution around the plume and an opportunity to further research.

For the model scenarios without damage zone, in the 60% SGR case (Fig. 35) the temperature change is distributed over a large area along the fault, compared to the 0% case, while the shale acts as a barrier to fluid flow and consequently blocks the temperature distribution, as already seen the fault as a barrier in 3D spatial distribution (Fig. 30). However, the stress ratio change is concentrated closer to the injector.

The decreased permeability damage zones (Fig. 36 & 37) seem to concentrate the temperature and pressure changes close to the injector which lead on a stress build up close to the injector and the fault. On the other hand, on the increased permeability damage zones the temperature, pressure and stress ratio changes are distributed along the fault (Fig. 36 & 37).

Regarding the temperature changes over time (Fig. 38), on the y = 200 m position seems that the decreased permeability damage zone model scenario remains stable and the base case too, while the increased permeability damage zone model scenario gets cooler faster, due to the easiest dispersion.

As explained before, the difference of temperature around the cold plume is the key to the increased stresses on the reservoir and the isolation of the temperature and stresses on the injector's side which leads stress distribution on the faults' plane/ barrier.

5.3 Limitations and simplifications that occurred

Challenges followed the conduction of this study due to the complexity of the subject and its multidisciplinary nature.

For the calculations of the Shale Gouge Ratio the challenges lead to simplifications that it was impossible to not be made such as:

- Some simplifications made the model more efficient and faster, without that meaning that the model's concept deviates from its main purpose.
- The seismic interpretation by definition is a simplification of the seismic transect and that leads to the discussion that for the needs of FLAC3D – ToughREACT were used already simplified data.

However, The seismic line and the seismic dataset outstand the approximations while it is as detailed as possible.

- The resolution of the seismic data (approximately 30 m) blocks the detail interpretation of the tectonic and geological features but the geometry of the model focus on a small part of the fault with assumptions such as the increase or decrease of the permeability, trying to predict the effect of the damage zone that is not visible. The different scenarios were modelled to give the opportunity for future comparison with data from reality (e.g. porosity and permeability of the damage zone).
- The FLAC3D – ToughREACT model required simplifications such as the complete isolation of the reservoir from the underburden and overburden layers which leads to the complete flow isolation of the simulated reservoir (no flow on the underburden and overburden layers). In reality, this kind of isolation cannot be possible but the comparison on the model scenarios' changes could be quantified successfully for this thesis.
- Damage factors' estimations for the damage zone of Delft sandstones could vary since it depends on rocks properties. Further research on the Delft sandstones would provide a better insight into the appropriate rock properties for the model for accurate results. The behaviour of the Delft sandstone during deformation will define which of the model results, presented in this thesis, are the more accurate (decreased or increased permeability in damage zone).

The lack of visual control on subsurface features below seismic resolution poses a clear technical and commercial risk (Rotevatn & Fossen, 2011). This risk can be mitigated through an understanding of fault growth processes and the application of technology.

However, the results obtained from the geological data sets significantly improve the setting-up of the FLAC3D-ToughREACT model.

6 Conclusion

Concluding this study, tectonic analysis, calculations of shale gouge inside fault, exploring various scenarios of SGR% inside the fault core, the effect of damage zone width, the impact of these different fault properties and its damage zone on fluid flow and temperature and stress distributions were defined.

The complex tectonic history of WNB was confirmed by the extend analysis of the stratigraphic layers of different ages. The Alblasserdam Member and the Delft Sandstone Member concluded as syn – rift formations. Genetically normal faults reactivated as reverse faults which followed by decreasing tectonic activity through time.

Shale gouge ratio results affect strongly the pressure and temperature distribution. The high but realistic shale gouge ratio results strongly affect the pressure compartmentalization. The different results on the models by changing even 10% the SGR% and its permeability input values, gives a clear impression about how important the further research on detailed definition of the SGR inside the fault core and the huge influence is that the shale has inside a fault core. A high shale gouge ratio is exacerbated (or has similar effects) by a permeability-increasing damage zone, but a permeability-decreasing damage zone mitigates its impacts. This emphasizes how important it is to comprehend how permeability evolves in fault damage zones.

The time evolution analysis reveals that the temperature has a higher influence along the fault and on the reservoir during time, while pressure remains stable after the first half month. However, a more detailed analysis shows that the pore pressure is the key to the stress distribution, while the diffusion of cold fluid increases the pressure due to convection circulation since the material shrinking from cold, creating rise of stress where the cold plume contacts the warm reservoir.

Yet, the general trend in damage zones in the literature was found mostly in research about granites as it was described previously. The need for detailed study about the effect of the rock composition of the damage zone is essential while the presence or absence of damage zone and the increase or decrease of permeability inside leads to impressively different results, even with occurred simplifications. The effect of the damage zone in permeability is important to be defined in the future, for the area of the WNB or in sandstones in general.

Considering the flow isolation of the reservoir (no flow on the underburden and overburden layers), this simplification is the strongest influence in the FLAC3D – ToughREACT model. However, it is a great opportunity for further research with a creation of a more complex layered model.

Overall, the geological insights with advanced modelling can manage and enlighten the induced seismicity problem and prediction as also to enhance and improve the reservoir performance in geothermal projects.

7 References

Abbink, O.A., Mijnlieff, H.F., Munsterman, D.K. & Verreussel, R.M.C.H., 2006. New stratigraphic insights in the 'Late Jurassic' of the Southern Central Sea Graben and Terschelling Basin (Dutch offshore) and related exploration potential. Netherlands Journal of Geosciences / Geologie en Mijnbouw 85: 221–238.

Al-Masgari, A.A.-S., Elsaadany, M., Abdul Latiff, A.H., Hermana, M., Hamzah, U.B., Babikir, I., Adeleke, T., Sohail Imran, Q., Al-Bared, M.A.M., 2021. Seismic Sequence Stratigraphic Sub-Division Using Well Logs and Seismic Data of Taranaki Basin, New Zealand. Appl. Sci. 11: 1226.

Bodenhausen, J.W.A. & Ott, W.F., 1981. Habitat of the Rijswijk oil province, onshore, The Netherlands. In: Illing, L.V., & Hobson, G.D. (eds): Petroleum geology of the Continental Shelf of North-West Europe. Institute of Petroleum (London): 301–309.

Bossennec, C., Géraud, Y., Moretti, I., Mattioni, L., Stemmelen, D., 2018. Pore network properties of sandstones in a fault damage zone. Journal of Structural Geology 110: 24-44.

Bouroullec, R., Verreussel, R.M.C.H., Geel, C.R., de Bruin, G., Zijp, M.H.A.A., Kőrösi, D., Munsterman, D.K., Janssen, N.M.M. & Kerstholt-Boegehold, S.J., 2018. Tectonostratigraphy of a rift basin affected by salt tectonics: synrift Middle Jurassic–Lower Cretaceous Dutch Central Graben, Terschelling Basin and neighbouring platforms, Dutch offshore. Geological Society of London, Special Publication 469: 269–303.

Crawford, B. R., Faulkner, D.R., Rutter, E. H., 2008. Strength, porosity, and permeability development during hydrostatic and shear loading of synthetic quartz-clay fault gouge, J. Geophys. Res. 113: B03207.

Crider, J.G., Peacock, D.C., 2004. Initiation of brittle faults in the upper crust: a review of field observations. J. Struct. Geol. 26: 691–707.

Choi, J.-H., 2016. Definition and classification of fault damage zones: a review and a new methodological approach, Earth Sci. Rev. 152: 70-87.

Christie-Blick, N., 1991. Onlap, offlap, and the origin of unconformity-bounded depositional sequences. Marine Geology 97: 35-56.

Cowie, P.A., Scholz, C.H., 1992. Growth of faults by accumulation of seismic slip. J. Geophys. Res. 97 (11), 085-011,095.

Crooijmans, R. A., Willems, C. J. L., Nick, H. M., Bruhn, D., 2016. The influence of facies heterogeneity on the doublet performance in low-enthalpy geothermal sedimentary reservoirs. - Geothermics 64: 209—219.

De Jager, J., 2003. Inverted basins in the Netherlands, similarities and differences. Netherlands Journal of Geosciences / Geologie en Mijnbouw 82: 339-349.

Den Hartog Jager, D.G., 1996. Fluviomarine sequences in the Lower Cretaceous of the West Netherlands Basin. In: Rondeel, H.E., Batjes, D.A.J. & Nieuwenhuijs, W.H. (eds): Geology of gas and oil under the Netherlands. Springer (Dordrecht): 229–241.

Dengfa, H., 2018. Basic types and geologic significances of “truncation and onlap” unconformities. Petroleum Exploration and Development 45(6): 1061–1074.

DINOloket stratigraphic nomenclature by TNO Geological Survey of The Netherlands (https://www.dinoloket.nl/en/stratigraphic-nomenclature)

Devault, B. & Jeremiah, J.M., 2002. Tectonostratigraphy of the Nieuwerkerk Formation (Delfland Subgroup), West Netherlands Basin. AAPG Bulletin 10: 1679–1707.

Donselaar, M.E., Groenenberg, R.M. & Gilding, D.T., 2015. Reservoir geology and geothermal potential of the Delft Sandstone Member in the West Netherlands Basin. World Geothermal Congress, 19–25 April 2015, Melbourne, Australia. Conference proceedings.

Dufour, F.C., 1984. Resultaten voorbereiding proefproject Delfland. In: Mot, E. (ed.): Verslag van het nationaal on- derzoekprogramma aardwarmte en warmteopslag 1979–1984 (NOA I). Project Bureau Energieonderzoek (Apeldoorn): 32–50.

Duin, E.J.T., Doornenbal, J.C., Rijkers, R.H.B., Verbeek, J.W. & Wong, T.E., 2006. Subsurface structure of the Netherlands: results of recent onshore and offshore mapping. Netherlands Journal of Geosciences / Geologie en Mijnbouw 85: 245–276.

Evans, J.P., Forster, C.B., Goddard, J.V., 1997. Permeability of fault-related rocks, and implications for hydraulic structure of fault zones. Journal of Structural Geology 19: 1393-1404.

Faulkner, D.R., Mitchell, T.M., Jensen, E., Cembrano Perasso, J., 2011. Scaling of fault damage zones with displacement and the implications for fault growth processes. Journal of Geophysical Research: Solid Earth. 116.

Fossen, H., 2016. *Structural Geology* (2nd ed.). Cambridge: Cambridge University Press.

Gardner, G.H.F., Gardner, L.W., & Gregory, A.R., 1974. Formation velocity and density -- the diagnostic basics for stratigraphic traps. *Geophysics* **39**: 770–780.

Grady, D.E., and Kipp, M.E., 1987. Dynamic rock fragmentation, in Fracture Mechanics of Rock, edited by B. K. Atkinson, Academic, San Diego, Calif. 429–475

Hamzah, U., 2016. Sequence stratigraphy of Paleocene – Holocene sedimentary deposits in Kupe field, Taranaki Basin, New Zealand. ARPN Journal of Engineering and Applied Sciences. 11: 1876-1890.

Herbert A. McKinstry, 1965. Thermal expansion of clay minerals. American Mineralogist 50: 212–222.

Herngreen, G.F.W. & Wong, T.E., 2007. Cretaceous. In: Wong, T.E., Batjes, D.A.J. & de Jager, J. (eds): Geology of the Netherlands. Royal Netherlands Academy of Arts and Sciences (Amsterdam): 127–150.

Jeremiah, J.M., Duxbury, S. & Rawson, P., 2010. Lower Cretaceous of the southern North Sea Basins: reservoir distribution within a sequence stratigraphic framework. Netherlands Journal of Geosciences / Geologie en Mijnbouw 89: 203–237.

Jordán, M.M., Meseguer, S., Pardo, F., Montero, M.A., 2015, Properties and possible ceramic uses of clays from lignite mine spoils of NW Spain - Applied Clay Science 118: 158–161.

Johri, M., Zoback, M.D., Hennings, P., 2014. A scaling law to characterize fault-damage zones at reservoir depthsFault Damage Zones at Depth. AAPG (Am. Assoc. Pet. Geol.) Bull. 98: 2057–2079.

Kahrobaei, S., Fonseca, R & Willems, Cees & Wilschut, Frank & Van Wees, J., 2019. Regional Scale Geothermal Field Development Optimization under Geological Uncertainties.

Katahara, K., 1995. Gamma Ray Log Response in Shaly Sands. The Log Analyst 36 (4): 50

KEM-15 A3: Geological review Study Risk of Seismicity due to Cooling Effects in Geothermal Systems 172146_REP02_MEZK21_Geol 01 | 16 March 2021 Ministerie van Economische Zaken en Klimaat

Kim, Y.-S., Andrews, J.R., Sanderson, D.J., 2000. Damage zones around strike-slip fault systems and strike-slip fault evolution, Crackington Haven, southwest England. Geosci. J. 4: 53–72.

Kim, Y.-S., Peacock, D., Sanderson, D.J., 2003. Mesoscale strike-slip faults and damage zones at Marsalforn, Gozo Island, Malta. J. Struct. Geol. 25: 793–812.

Kim, Y.-S., Peacock, D.C.P., Sanderson, D.J., 2004. Fault damage zones. J. Struct. Geol. 26: 503–517.

Knaap, W.A. & Coenen, M.J., 1987. Exploration for oil and natural gas. In: Visser, W.A., Zonneveld, J.I.S. & van Loon, A.J. (eds): Seventy-five years of geology and mining in the Netherlands 1912–1987. Kluwer (The Hague): 207–231.

Kombrink, H., Doornenbal, J.C., Duin, E.J.T., den Dulk, M., van Gessel, S.F., ten Veen, J.H., & Witmans, N., 2012. New insights into the geological structure of the Netherlands; results of a detailed mapping project - Netherlands Journal of Geosciences 91: 419 – 446.

Lokhorst, A., 2000. Aardwarmte in Nederland Verslag van het onderzoekprogramma 'Instandhouding Kennis Aardwarmte Exploratie en Exploitatie in Nederland (1997-2000)'. TNO report (Utrecht).

Meng, T., Li, E., Xue Y., Ma, J., Liu, W., Xufeng, L., 2021. Experimental study on permeability and porosity evolution of host rock with varying damage degrees in excavation damaged area under real-time ultra-high temperature and triaxial stress/seepage pressure condition" Bulletin of Engineering Geology and the Environment 80:8075–8097.

Merrifield, M., Holgate, S., Mitchum, G., Pérez, B., Rickards, L., Schöne, T., Woodworth, P., Wöppelmann, G., 2012. Global Sea-level Observing System (GLOSS) Implementation plan – 2012, UNESCO-IOC.

Mitchell, T.M., Faulkner, D.R. 2009. The nature and origin of off-fault damage surrounding strike-slip fault zones with a wide range of displacements: a field study from the Atacama fault system, northern Chile. J. Struct. Geol. 31: 802-816.

Mitchum Jr., R.M., 1977. Seismic stratigraphy and global changes of sea level. Part 11: glossary of terms used in seismic stratigraphy. In: Payton, C.E. (Ed.), Seismic stratigraphy—Applications to Hydrocarbon Exploration 26. A.A.P.G. Memoir, pp. 205–212.

Munsterman, D.K., 2012. De resultaten van het palynologische onderzoek naar de ouderdom van de Onder Krijt successie in boring Van den Bosch-04 (VDB-04), interval 925–2006 m. TNO report (Utrecht).

NAM & RGD, 1980. Stratigraphic nomenclature of the Netherlands. Verhandelingen van het Koninklijk Nederlands Geologisch Mijnbouwkundig Genootschap 32, 77.

Ostermeijer G.A., Mitchell, T. M., Aben. F. M., Dorsey, M. T., Browning, J., Rockwell, T. K., Fletcher, J. M., Ostermeijer, F., 2020. Damage zone heterogeneity on seismogenic faults in crystalline rock; a field study of the Borrego Fault, Baja California, Journal of Structural Geology 137: 104016.

Oxford Reference.

O'Hara, A.P., Jacobi, R.D., Sheets, H.D., 2017. Predicting the width and average fracture frequency of damage zones using a partial least squares statistical analysis: implications for fault zone development. J. Struct. Geol. 98: 38–52.

PanTerra Geoconsultants B.V., 2010, Geologisch onderzoek: Aardwarmte in het Westland, page 27-28.

PanTerra Geoconsultants B.V., 2019. Geological report Maasdijk – 1900011-00.

PanTerra Geoconsultants B.V., 2020. Geothermie Delft Doublet.

Peacock, D.C.P., Nixon, C.W., Rotevatn, A., Sanderson, D.J., Zuluaga, L.F., 2016. Glossary of fault and other fracture networks. J. Struct. Geol. 92: 12–29.

Peeters, S.H.J., 2016. Mesozoic strike-slip faults in the northern Dutch offshore; new insights from seismic- and analogue modelling data. University of Utrecht: MSc thesis.

Price, N.J., Cosgrove, J.W., 1990. Analysis of Geological Structures. Cambridge University Press.

Racero-Baena, A. & Drake, S.J., 1996. Structural style and reservoir development in the West Netherlands oil province. In: Rondeel, H. E., Anders, D., Batjes, J. & Nieuwenhuijs, W.H. (eds): Geology of gas and oil under the Netherlands. Springer (Dordrecht): 211–227.

Ramaekers, J., Geel, K., Lokhorst, A. & Simmelink, H.J., 2006. Nader onderzoek naar mogelijkheden van aardwarmtewinning voor de vleestomaatkwekerij van Fa A&G van den Bosch BV te Bleiswijk. TNO report (Utrecht).

Reiter, K., Heidbach, O., and Ziegler, M. O., 2024. Impact of faults on the remote stress state, Solid Earth, 15: 305–327.

Reuver, F. de, 1992. FINAL REPORT VOLUME II Sedimentology, Petrology and Reservoir properties of Lower Cretaceous Delfland Deposits in cores 1 from wells BRAKEL-1 and ANDEL-6, Report No. G63B-1.

Rotevatn, A., Fossen, H., 2011. Simulating the effect of subseismic fault tails and process zones in a siliciclastic reservoir analogue: Implications for aquifer support and trap definition, Marine and Petroleum Geology 28: 1648-1662.

Russell, W.L., 1944. The total gamma ray activity of sedimentary rocks as indicated by Geiger counter determinations. Geophysics 9 (2): 180-216.

Savage, H. M., and Brodsky, E. E., 2011. Collateral damage: Evolution with displacement of fracture distribution and secondary fault strands in fault damage zones, J. Geophys. Res., 116: B03405

Schmatz, J., Vrolijk, P. J., Urai, J. L., 2010. Clay smear in normal fault zones – The effect of multilayers and clay cementation in water-saturated model experiments, Journal of Structural Geology 32: 1834-1849.

Scholz, C. H., N. H. Dawers, J. Z. Yu, M. H. Anders, and P. Cowie (1993), Fault growth and fault scaling laws: Preliminary results, J. Geophys. Res. 98(B12), 21,951–21,961.

Scholz, C. H., 2002. The Mechanics of Earthquake Faulting (2nd ed.). Cambridge: Cambridge University Press.

Sheriff, R.E., Geldart, L.P., 1995. *Exploration Seismology*. 2nd ed. Cambridge University Press

Soustelle, V., ter Heege, J., Buijze, L., Wassing, B., 2022. WarmingUP: Thermomechanical parameters of geothermal analogue reservoir sandstones in the West Netherlands Basin (Final Report)

Supandi, S., Zufialdi, Z., Sukiyah, Emi, S., and Adjat, S., 2019. The Influence of Kaolinite - Illite toward mechanical properties of Claystone. *Open Geosciences*, 11: 440-446.

Szklarz, S.P., Barros, E.G.D., Khoshnevis Gargar, N., Peeters, S.H.J., Wees, J.D.A.M. van, Pul- Verboom, V. van 2022. Geothermal Field Development Optimization Application to Maasdijk Reservoir: Delft and Alblasserdam Stacked Formations.

Taron, J., Elsworth, D., 2009. Thermal–hydrologic–mechanical–chemical processes in the evolution of engineered geothermal reservoirs. International Journal of Rock Mechanics and Mining Sciences 46: 855-864.

Van Adrichem Boogaert, H.A. & Kouwe, W.F.P., 1993. Stratigraphic nomenclature of the Netherlands, revision and update by Rijks Geologische Dienst (RGD) and Netherlands Oil and Gas Exploration and Production Association (NOGEPA). Mededelingen Rijks Geologische Dienst 50: 180 pp.

Van Adrichem Boogaert, H.A. & Kouwe, W.F.P., 1997. Stratigraphic nomenclature of the Netherlands, revision and update by RGD and NOGEPA, Section A. In: Mededelingen Rijks Geologische Dienst 50 (Haarlem): 1–40.

Van Amerom, H.W.J., Herngreen, G.F.W., and Romein, B.J., 1976. Palaeobotanical and palynological investigation with notes on the microfauna of some core samples from the Lower Cretaceous of the West Netherlands Basin, Mededelingen Rijks Geologische Dienst NS, 27: 41-79.

Van Wijhe, D.H., 1987. Structural evolution of inverted basins in the Dutch offshore. Tectonophysics 137: 171–219.

Vejbbæk, O.V., Andersen, C., Dusar, M., Herngreen, G.F.W., Krabbe, H., Leszczynski, K., Lott, G.K., Mutterlose, J. & Van der Molen, A.S., 2010. Cretaceous. In: Doornenbal, J.C. & Stevenson, A.G. (eds): Petroleum geological atlas of the Southern Permian Basin area. EAGE Publications b.v. (Houten): 195–209.

Verreussel, R.M.C.H., Bouroullec, R., Munsterman, D.K., Dybkjær, K., Geel, C.R., Houben, A.J.P., Johannessen, P.N. & Kerstholt-Boegehold, S.J., 2018. Stepwise basin evolution of the Middle Jurassic–Early Cretaceous rift phase in the Central Graben area of Denmark, Germany and the Netherlands. Geological Society of London, Special Publication 469: 305–340.

Verreussel, R., Peeters, S., 2024. Syn-rift depositional patterns of the Nieuwerkerk Formation in the central part of the West Netherlands Basin. TNO internal report R12341

Vermilye, J. M., and C. H. Scholz 1998, The process zone: A microstructural view of fault growth, J. Geophys. Res., 103(B6), 12,223–12,237, doi:10.1029/98JB00957.

Verweij, J.M., Boxem, T.A.P., Nelskamp, S., 2016. 3D spatial variation in vertical stress in on- and offshore Netherlands; integration of density log measurements and basin modeling results, Marine and Petroleum Geology 78, 870-882.

Vis, G.J., Van Gessel, S.F., Mijnlieff, H.F., Pluymaekers, M.P.D., Hettelaar, D.P.M. & Stegers, D.P.M., 2010. Lower Cretaceous Rijnland Group aquifers in the West Netherlands Basin: suitability for geothermal energy. TNO report (Utrecht).

Vondrak, A.G., Donselaar, M.E. & Munsterman, D.K., 2018. Reservoir architecture model of the Nieuwerkerk Formation (Early Cretaceous, West Netherlands Basin): diachronous development of sand-prone fluvial deposits. Geological Society of London, Special Publication 469: 423–434.

Wassing B.B.T., Candela T., Osinga S., Peters E., Buijze L., Fokker P.A., Van Wees J.D., 2021. Time-dependent Seismic Footprint of Thermal Loading for Geothermal Activities in Fractured Carbonate Reservoirs, Frontiers in Earth Science 9

Willems, C.J.L., Vondrak, A.G., Munsterman, D.K., Donselaar, M.E. & Mijnlieff, H.F., 2017. Regional geothermal aquifer architecture of the fluvial Lower Cretaceous Nieuwerkerk Formation: a palynological analysis. Netherlands Journal of Geosciences / Geologie en Mijnbouw 96: 319–330.

Willems, C.J.L., Nick, H.M., 2019. Towards optimisation of geothermal heat recovery: An example from the West Netherlands Basin, Applied Energy 247: 582-593

Willems, C.J.L., Vondrak, A.G., Mijnlieff, H., Donselaar, M.E., van Kempen, B.M.M., 2020. Geology of the Upper Jurassic to Lower Cretaceous geothermal aquifers in the West Netherlands Basin – an overview. Netherlands Journal of Geosciences 99: e1.

Wong, T.E., 2007. Jurassic. In: Wong, T.E., Batjes, D.A.J. & Jager, J. de (eds): Geology of the Netherlands. Royal Netherlands Academy of Arts and Sciences (Amsterdam): 107–125.

Yielding, G., 2002. Shale gouge ratio—Calibration by geohistory. Norwegian Petroleum Society Special Publications, Elsevier. 11: 1-15.

Zang, A., Wagner, F. C., Stanchits, S., Janssen, C., and Dresen, G., 2000. Fracture process zone in granite, J. Geophys. Res. 105(B10), 23,651–23,661.

Ziegler, P.A, 1990. Geological atlas of western and central Europe, part 2, Geological Society Publishing House (Bath), 239.

8 Appendix

8.1. Temperature for FLAC3D model

The geothermal gradient for the area is 3.15 °C/100m (Fig. 41; Geologische evaluatie t.b.v. Geothermie Delft Doublet, 2020)

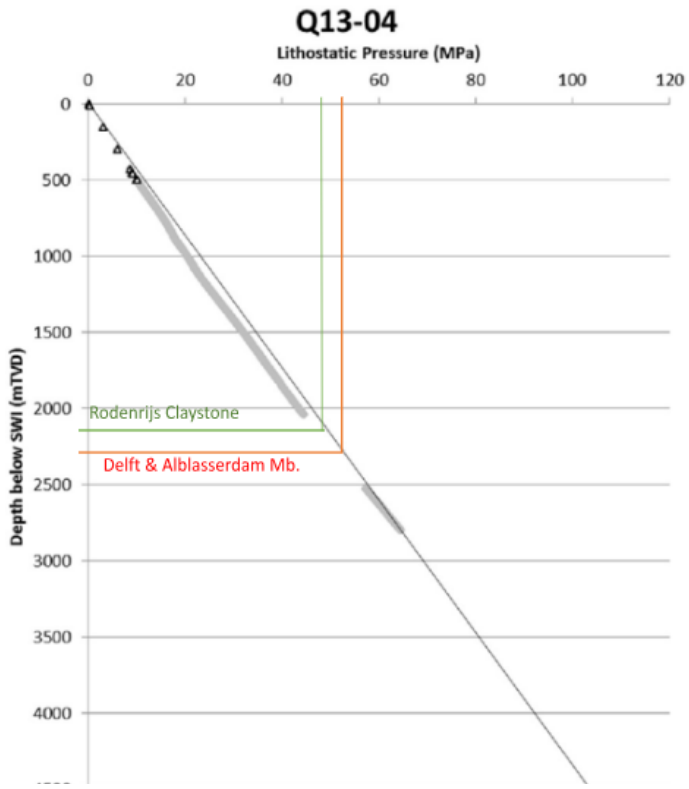

Figure 41. Cross plot of lithostratigraphic pressure versus depth in the inverted WNB (Verweij et al. 2016).

For the Delft Sandstone (defined as Reservoir 2, R2) and Alblasserdam Mb. (defined as reservoir 1, R1) the reservoirs temperature is: 2259,6 m * 0,0315 °C/m = 71 °C.

For the effective pressure of Delft Sandstone Mb. (R1) & Alblasserdam Mb. (R2) of the model (as they have the same depth) in depth equal to 2259,6 m, the lithostatic pressure is 54 MPa. Based on the previous, the pore pressure (hydrostatic) is calculated by (1000 * 2300 * 10)/1e^6 = 23MPa and the effective pressure by (overburden pressure - pore pressure) = 54 – 23 = 31 MPa.

8.2. Solid Density of the reservoirs

The used density is 2650 kg/m^3. The solid density that was used found in the study of Willems and Nick (2019). For both reservoir the solid density that was used is the same (see Appendix tables).

The reason that was used the same solid density is based on the observation that Alblasserdam Mb., on the sand/clay ratio from the log's gamma ray data is not very different from the Delft Sandstone.

8.3. Thermal expansion

The graph that was used for the interpolation of the reservoirs' thermal expansion was found in the WarmingUp report by Soustelle et al. (2022) (Fig. 42). The values were extracted from the graph by using the maximum temperature for the rock type samples similar to the reservoirs' rock types.

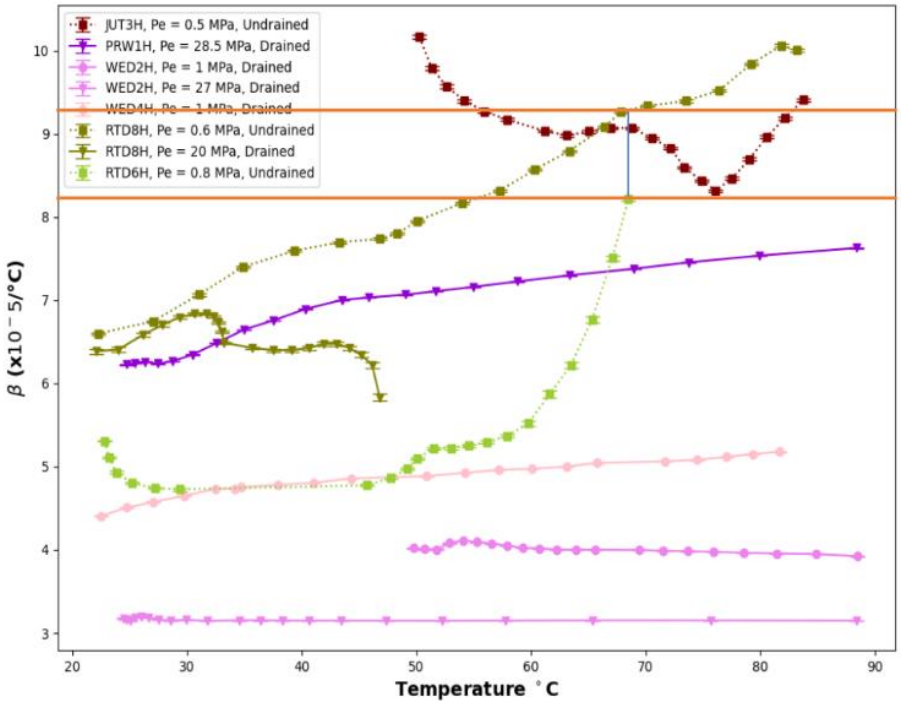

Figure 42. Graph from Soustelle et al. (Warming Up, 2022), which *used for finding the thermal expansion values based on the rock types in the maximum possible Temperature of the experiments of this study.*

The values that were used are 8,2 x 10^{-5} °C for Alblasserdam Mb and 9,3 x 10^{-5} °C for Delft Sandstone Mb..

8.4. Elastic Moduli

From the experimental study of Soustelle et al. (WarmingUp, 2022), the samples similar to the rock types of the reservoirs of this study were used for the values of the Elastic moduli (Fig. 43). For the bulk modulus, the values that were used are 3,7 GPa for Alblasserdam Mb. and 6 GPa for Delft Sandstone Mb. For Poisson's ratio values were used 0,187 for Alblasserdam Mb. and 0,154 for Delft Sandstone Mb.

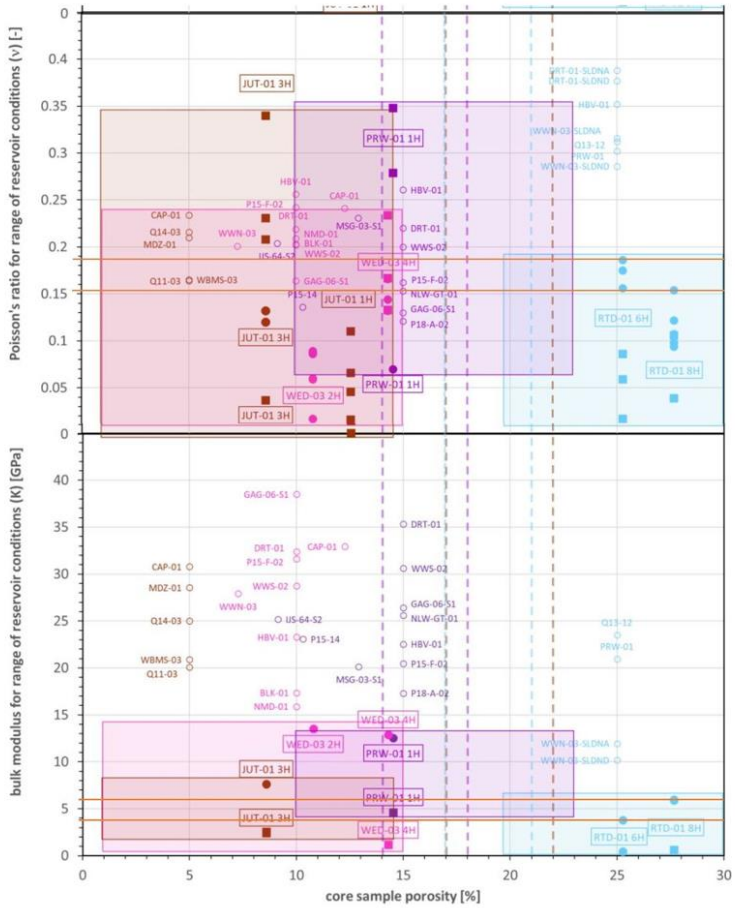

Figure 43. Graphs from Soustelle et al., *(Warming Up, 2022), where were used for the estimation of the Bulk modulus and Poisson's ratio for the Alblasserdam and Delft Members.*

8.5. Tables of the different scenario models

Table 8. Table with the values of 0% SGR in the fault core scenario model with the increased and decreased permeability values.

	Reservoir 2 b (Delft SSt Mb.)	Reservoir 1 a (Alblasserdam Mb.)	Damage zone b-2 outer	Damage zone b-2 inner	Damage zone a-1 outer	Damage zone a-1 inner	Fault
Initial Pore Pressure	23 MPa						
Initial Temperature	71 °C						
Bulk modulus	6 GPa	3,7 GPa	6 GPa	6 GPa	3,7 GPa	3,7 GPa	5 GPa
Poisson ratio	0,154	0,187	0,154	0,154	0,187	0,187	0,165
Solid density	2.650 kg/m^3	2.650 kg/m^3	2.650 kg/m^3	2.650 kg/m^3	2.650 kg/m^3	2.650 kg/m^3	2650 kg/m^3
Thermal expansion	9,3 x 10^{-5} °C	8,2 x 10^{-5} °C	9,3 x 10^{-5} °C	9,3 x 10^{-5} °C	8,2 x 10^{-5} °C	8,2 x 10^{-5} °C	8,75 x 10^{-5} °C
Heat conductivity	4,5 Wm−1 K−1 (3)	4,5 Wm−1 K−1 (3)	4,5 Wm−1 K−1 (3)	4,5 Wm−1 K−1 (3)	4,5 Wm−1 K−1 (3)	4,5 Wm−1 K−1 (3)	4,5 W m−1 K−1
Specific Heat	730 J kg^{-1} K^{-1} (3)	730 J kg^{-1} K^{-1} (3)	730 J kg^{-1} K^{-1} (3)	730 J kg^{-1} K^{-1} (3)	730 J kg^{-1} K^{-1} (3)	730 J kg^{-1} K^{-1} (3)	730 J kg−1 K−1 (3)
Initial Permeability (decrease)	7.00 x 10^{-13} m^2 6.00 x 10-13 m2 1.80 x 10-13 m2	1.49 x 10^{-13} m^2 2.96 x 10-13 m2 0.39 x 10-13 m2	2.33 x 10^{-13} m^2 2.00 x 10-13 m2 0.60 x 10-13 m2 /3	7.00 x 10^{-14} m^2 6.00 x 10-14 m2 1.80 x 10-14 m2 /10	4.97 x 10^{-14} m^2 9.87 x 10-14 m2 0.13 x 10-13 m2	1.49 x 10^{-14} m^2 2.96 x 10-14 m2 0.39 x 10-14 m2	5.00 x 10^{-14} m^2 3.75 x 10^{-14} m^2 1.00 x 10^{-14} m^2
Initial Permeability (increase)	7,00 x 10^{-13} m^2 6,00 x 10-13 m2 1,80 x 10-13 m2	1,49 x 10^{-13} m^2 2,96 x 10-13 m2 0,39 x 10-13 m2	2,10 x 10^{-12} m^2 1,80 x 10-12 m2 5,40 x 10-13 m2 *3	7,00 x 10^{-12} m^2 6,00 x 10-12 m2 1,80 x 10-12 m2 *10	4,47 x 10^{-13} m^2 8,88 x 10-13 m2 1,17 x 10-13 m2 *3	1,49 x 10^{-12} m^2 2,96 x 10-12 m2 0,39 x 10-12 m2	5,00 x 10^{-12} m^2 3,75 x 10^{-12} m^2 1,00 x 10^{-12} m^2

Table 9. Table with the values of 50% SGR in the fault core scenario model with initial permeability values.

	Reservoir 2 (Delft SSt Mb.)	Reservoir 1 (Alblasserdam Mb.)	Damage zone 2	Damage zone 1	Fault
Initial Pore Pressure	23 MPa				
Initial Temperature	71 °C				
Bulk modulus	6 GPa	3,7 GPa	6 GPa	3,7 GPa	5 GPa
Poisson ratio	0,154	0,187	0,154	0,187	0,165
Solid density	2.650 kg/m^3	2.650 kg/m^3	2.650 kg/m^3	2.650 kg/m^3	2650 kg/m^3
Thermal expansion	9,3 x 10^{-5} °C	8,2 x 10^{-5} °C	9,3 x 10^{-5} °C	8,2 x 10^{-5} °C	5 x 10^{-6} °C
Heat conductivity	4,5 Wm−1 K−1 (3)	4,5 Wm−1 K−1 (3)	4,5 Wm−1 K−1 (3)	4,5 Wm−1 K−1 (3)	2.5 W m−1 K−1
Specific Heat	730 J kg^{-1} K^{-1} (3)	730 J kg^{-1} K^{-1} (3)	730 J kg^{-1} K^{-1} (3)	730 J kg^{-1} K^{-1} (3)	950 J kg−1 K−1 (3) (9,5)
Initial Permeability	7.00 x 10^{-13} m^2 6.00 x 10-13 m2 1.80 x 10-13 m2	1.49 x 10^{-13} m^2 2.96 x 10-13 m2 0,39 x 10-13 m2	7.00 x 10^{-13} m^2 6.00 x 10-13 m2 1.80 x 10-13 m2	1.49 x 10^{-13} m^2 2.96 x 10-13 m2 0,39 x 10-13 m2	xx 1,3 x 10^{-15} yy 1,3 x 10-19 zz 1,3 x 10-19

For the 60% SGR Model case:

Table 10. Table with the values of 60% SGR in the fault core scenario model with initial permeability values.

	Reservoir 2 (Delft SSt Mb.)	Reservoir 1 (Alblasserdam Mb.)	Damage zone 2	Damage zone 1	Fault
Initial Pore Pressure	23 MPa				
Initial Temperatute	71 °C				
Bulk modulus	6 GPa	3,7 GPa	6 GPa	3,7 GPa	5 GPa
Poisson ratio	0,154	0,187	0,154	0,187	0,165
Solid density	2.650 kg/m^3	2.650 kg/m^3	2.650 kg/m^3	2.650 kg/m^3	2650 kg/m^3
Thermal expansion	9,3 x 10^{-5} °C	8,2 x 10^{-5} °C	9,3 x 10^{-5} °C	8,2 x 10^{-5} °C	5 x 10^{-6} °C
Heat conductivity	4,5 Wm−1 K−1 (3)	4,5 Wm−1 K−1 (3)	4,5 Wm−1 K−1 (3)	4,5 Wm−1 K−1 (3)	2.5 W m−1 K−1
Specific Heat	730 J kg^{-1} K^{-1} (3)	730 J kg^{-1} K^{-1} (3)	730 J kg^{-1} K^{-1} (3)	730 J kg^{-1} K^{-1} (3)	950 J kg−1 K−1 (3) (9,5)
Initial Permeability	7.00 x 10^{-13} m^2 6.00 x 10-13 m2 1.80 x 10-13 m2	1.49 x 10^{-13} m^2 2.96 x 10-13 m2 0,39 x 10-13 m2	7.00 x 10^{-13} m^2 6.00 x 10-13 m2 1.80 x 10-13 m2	1.49 x 10^{-13} m^2 2.96 x 10-13 m2 0,39 x 10-13 m2	xx 1,3 x 10^{-15} yy 1,3 x 10-19 zz 1,3 x 10-19

Table 11. Table with the values of 40% SGR in the fault core scenario model with the increased and decreased permeability values.

	Reservoir 2 (Delft SSt Mb.)	Reservoir 1 (Alblasserdam Mb.)	Damage zone b-2 outer	Damage zone b-1 inner	Damage zone a-2 outer	Damage zone a-1 inner	Fault
Initial Pore Pressure	23 MPa						
Initial Temperatute	71 °C						
Bulk modulus	6 GPa	3,7 GPa	6 GPa	6 GPa	3,7 GPa	3,7 GPa	5 GPa
Poisson ratio	0,154	0,187	0,154	0,154	0,187	0,187	0,165
Solid density	2.650 kg/m^3	2.650 kg/m^3	2.650 kg/m^3	2.650 kg/m^3	2.650 kg/m^3	2.650 kg/m^3	2650 kg/m^3
Thermal expansion	9,3 x 10^{-5} °C	8,2 x 10^{-5} °C	9,3 x 10^{-5} °C	9,3 x 10^{-5} °C	8,2 x 10^{-5} °C	8,2 x 10^{-5} °C	5 x 10^{-6} °C
Heat conductivity	4,5 $Wm{-}1\ K{-}1$ (3)	4,5 $Wm{-}1\ K{-}1$ (3)	4,5 $Wm{-}1\ K{-}1$ (3)	4,5 $Wm{-}1\ K{-}1$ (3)	4,5 $Wm{-}1\ K{-}1$ (3)	4,5 $Wm{-}1\ K{-}1$ (3)	2.5 $W\ m{-}1\ K{-}1$
Specific Heat	730 $J\ kg^{-1}\ K^{-1}$ (3)	730 $J\ kg^{-1}\ K^{-1}$ (3)	730 $J\ kg^{-1}\ K^{-1}$ (3)	730 $J\ kg^{-1}\ K^{-1}$ (3)	730 $J\ kg^{-1}\ K^{-1}$ (3)	730 $J\ kg^{-1}\ K^{-1}$ (3)	950 $J\ kg{-}1\ K{-}1$ (3) (9,5)
Initial Permeability Decrease	7.00 x 10^{-13} m^2 6.00 x 10-13 m2 1.80 x 10-13 m2	1.49 x 10^{-13} m^2 2.96 x 10-13 m2 0,39 x 10-13 m2	2.33 x 10^{-13} m^2 2.00 x 10-13 m2 0.60 x 10-13 m2 /3	7.00 x 10^{-14} m^2 6.00 x 10-14 m2 1.80 x 10-14 m2 /10	4.97 x 10^{-14} m^2 9.87 x 10-14 m2 0,13 x 10-13 m2	1.49 x 10^{-14} m^2 2.96 x 10-14 m2 0,39 x 10-14 m2	1,90 x 10^{-16} m^2 1,90 x 10-20 m2 1,90 x 10-20 m2
Initial Permeability Increase	7,00 x 10^{-13} m^2 6,00 x 10-13 m2 1,80 x 10-13 m2	1,49 x 10^{-13} m^2 2,96 x 10-13 m2 0,39 x 10-13 m2	2,10 x 10^{-12} m^2 1,80 x 10-12 m2 5,40 x 10-13 m2 *3	7,00 x 10^{-12} m^2 6,00 x 10-12 m2 1,80 x 10-12 m2 *10	4,47 x 10^{-13} m^2 8,88 x 10-13 m2 1,17 x 10-13 m2 *3	1,49 x 10^{-12} m^2 2,96 x 10-12 m2 0,39 x 10-12 m2	1,90 x 10^{-14} m^2 1,90 x 10-18 m2 1,90 x 10-18 m2

Table 12. Table with the values of 50% SGR in the fault core scenario model with the increased and decreased permeability values.

	Reservoir 2 (Delft SSt Mb.)	Reservoir 1 (Alblasserdam Mb.)	Damage zone b-2 outer	Damage zone b-1 inner	Damage zone a-2 outer	Damage zone a-1 inner	Fault
Initial Pore Pressure	23 MPa						
Initial Temperatute	71 °C						
Bulk modulus	6 GPa	3,7 GPa	6 GPa	6 GPa	3,7 GPa	3,7 GPa	5 GPa
Poisson ratio	0,154	0,187	0,154	0,154	0,187	0,187	0,165
Solid density	2.650 kg/m^3	2.650 kg/m^3	2.650 kg/m^3	2.650 kg/m^3	2.650 kg/m^3	2.650 kg/m^3	2650 kg/m^3
Thermal expansion	9,3 x 10^{-5} °C	8,2 x 10^{-5} °C	9,3 x 10^{-5} °C	9,3 x 10^{-5} °C	8,2 x 10^{-5} °C	8,2 x 10^{-5} °C	5 x 10^{-6} °C
Heat conductivity	4,5 Wm−1 K−1 (3)	4,5 Wm−1 K−1 (3)	4,5 Wm−1 K−1 (3)	4,5 Wm−1 K−1 (3)	4,5 Wm−1 K−1 (3)	4,5 Wm−1 K−1 (3)	2.5 W m−1 K−1
Specific Heat	730 J kg^{-1} K^{-1} (3)	730 J kg^{-1} K^{-1} (3)	730 J kg^{-1} K^{-1} (3)	730 J kg^{-1} K^{-1} (3)	730 J kg^{-1} K^{-1} (3)	730 J kg^{-1} K^{-1} (3)	950 J kg−1 K−1 (3) (9,5)
Initial Permeability Decrease	7.00 x 10^{-13} m^2 6.00 x 10-13 m2 1.80 x 10-13 m2	1.49 x 10^{-13} m^2 2.96 x 10-13 m2 0,39 x 10-13 m2	2.33 x 10^{-13} m^2 2.00 x 10-13 m2 0.60 x 10-13 m2 /3	7.00 x 10^{-14} m^2 6.00 x 10-14 m2 1.80 x 10-14 m2 /10	4.97 x 10^{-14} m^2 9.87 x 10-14 m2 0,13 x 10-13 m2	1.49 x 10^{-14} m^2 2.96 x 10-14 m2 0,39 x 10-14 m2	1,30 x 10^{-16} m^2 1,30 x 10-20 m2 1,30 x 10-20 m2
Initial Permeability Increase	7,00 x 10^{-13} m^2 6,00 x 10-13 m2 1,80 x 10-13 m2	1,49 x 10^{-13} m^2 2,96 x 10-13 m2 0,39 x 10-13 m2	2,10 x 10^{-12} m^2 1,80 x 10-12 m2 5,40 x 10-13 m2 *3	7,00 x 10^{-12} m^2 6,00 x 10-12 m2 1,80 x 10-12 m2 *10	4,47 x 10^{-13} m^2 8,88 x 10-13 m2 1,17 x 10-13 m2 *3	1,49 x 10^{-12} m^2 2,96 x 10-12 m2 0,39 x 10-12 m2	1,30 x 10^{-14} m^2 1,30 x 10-18 m2 1,30 x 10-18 m2

Table 13. Table with the values of 60% SGR in the fault core scenario model with the increased and decreased permeability values.

	Reservoir 2 (Delft SSt Mb.)	Reservoir 1 (Alblasserdam Mb.)	Damage zone b-2 outer	Damage zone b-1 inner	Damage zone a-2 outer	Damage zone a-1 inner	Fault
Initial Pore Pressure	23 MPa						
Initial Temperature	71 °C						
Bulk modulus	6 GPa	3,7 GPa	6 GPa	6 GPa	3,7 GPa	3,7 GPa	5 GPa
Poisson ratio	0,154	0,187	0,154	0,154	0,187	0,187	0,165
Solid density	2.650 kg/m^3	2.650 kg/m^3	2.650 kg/m^3	2.650 kg/m^3	2.650 kg/m^3	2.650 kg/m^3	2650 kg/m^3
Thermal expansion	$9,3 \times 10^{-5}$ °C	$8,2 \times 10^{-5}$ °C	$9,3 \times 10^{-5}$ °C	$9,3 \times 10^{-5}$ °C	$8,2 \times 10^{-5}$ °C	$8,2 \times 10^{-5}$ °C	5×10^{-6} °C
Heat conductivity	4,5 $Wm^{-1} K^{-1}$ (3)	4,5 $Wm^{-1} K^{-1}$ (3)	4,5 $Wm^{-1} K^{-1}$ (3)	4,5 $Wm^{-1} K^{-1}$ (3)	4,5 $Wm^{-1} K^{-1}$ (3)	4,5 $Wm^{-1} K^{-1}$ (3)	2.5 $W m^{-1} K^{-1}$
Specific Heat	730 $J kg^{-1} K^{-1}$ (3)	730 $J kg^{-1} K^{-1}$ (3)	730 $J kg^{-1} K^{-1}$ (3)	730 $J kg^{-1} K^{-1}$ (3)	730 $J kg^{-1} K^{-1}$ (3)	730 $J kg^{-1} K^{-1}$ (3)	950 $J kg^{-1} K^{-1}$ (3) (9,5)
Initial Permeability Decrease	7.00×10^{-13} m^2 6.00 x 10-13 m2 1.80 x 10-13 m2	1.49×10^{-13} m^2 2.96 x 10-13 m2 0,39 x 10-13 m2	2.33×10^{-13} m^2 2.00 x 10-13 m2 0.60 x 10-13 m2 /3	7.00×10^{-14} m^2 6.00 x 10-14 m2 1.80 x 10-14 m2 /10	4.97×10^{-14} m^2 9.87 x 10-14 m2 0,13 x 10-13 m2	1.49×10^{-14} m^2 2.96 x 10-14 m2 0,39 x 10-14 m2	$7,00 \times 10^{-17}$ m^2 7,00 x 10-21 m2 7,00 x 10-21 m2
Initial Permeability Increase	$7,00 \times 10^{-13}$ m^2 6,00 x 10-13 m2 1,80 x 10-13 m2	$1,49 \times 10^{-13}$ m^2 2,96 x 10-13 m2 0,39 x 10-13 m2	$2,10 \times 10^{-12}$ m^2 1,80 x 10-12 m2 5,40 x 10-13 m2 *3	$7,00 \times 10^{-12}$ m^2 6,00 x 10-12 m2 1,80 x 10-12 m2 *10	$4,47 \times 10^{-13}$ m^2 8,88 x 10-13 m2 1,17 x 10-13 m2 *3	$1,49 \times 10^{-12}$ m^2 2,96 x 10-12 m2 0,39 x 10-12 m2	$7,00 \times 10^{-15}$ m^2 7,00 x 10-19 m2 7,00 x 10-19 m2

8.6. Results of FLAC3D – ToughREACT

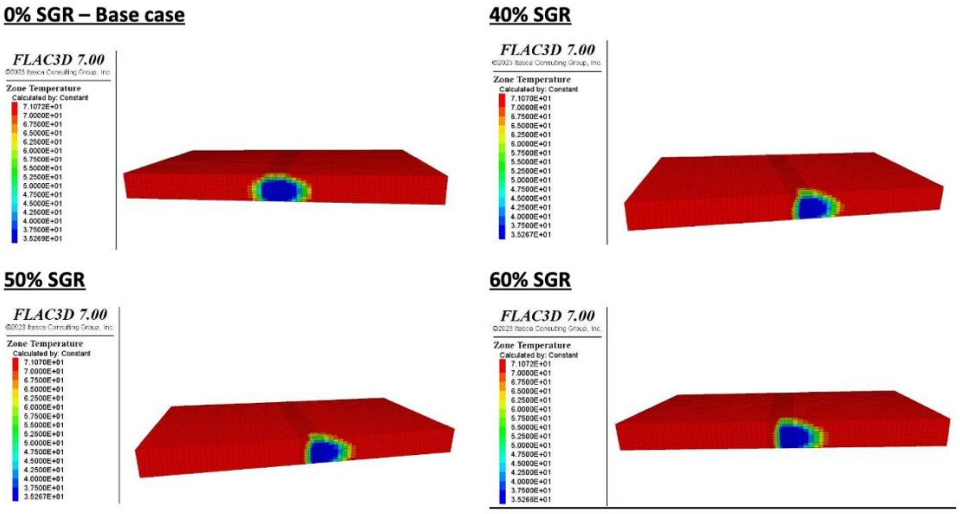

Figure 44. FLAC3D model results which compare the effect on the temperature of the reservoir on the base case (0% SGR, no width zone) with the 40%, 50% and 60% SGR model scenarios without damage zone.

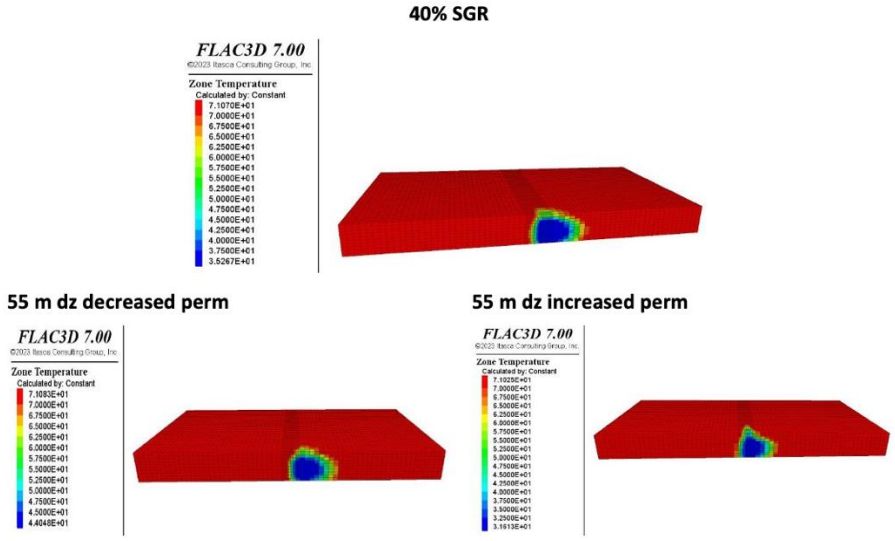

Figure 45. FLAC3D model results which compare the effect on the temperature of the reservoir on the 40% SGR model scenario with decreasing and decreasing permeability in the damage zone.

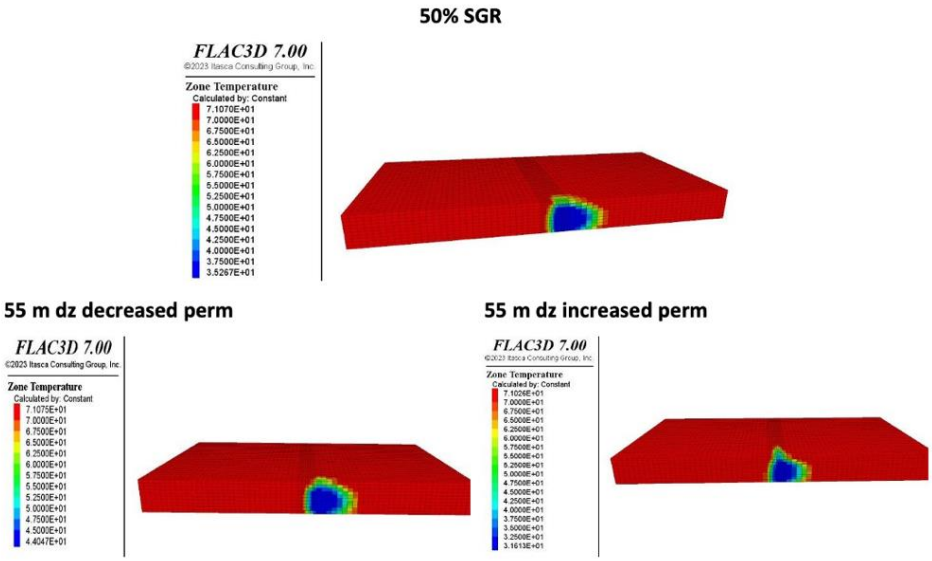

Figure 46. FLAC3D model results which compare the effect on the temperature of the reservoir on the 50% SGR model scenario with decreasing and decreasing permeability in the damage zone.

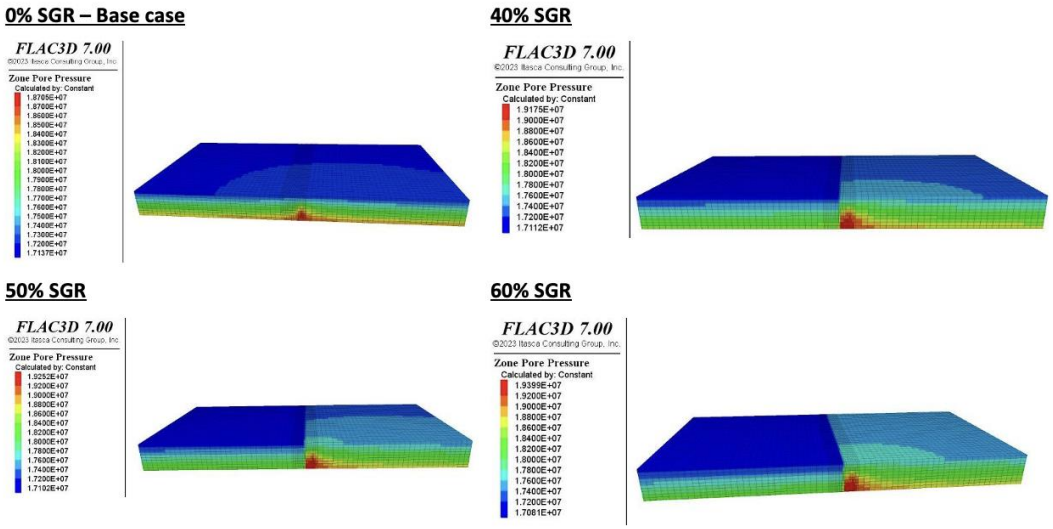

Figure 47. FLAC3D model results which compare the effect on the pore pressure of the reservoir on the base case (0% SGR, no width zone) with the 40%, 50% and 60% SGR model scenarios without damage zone.

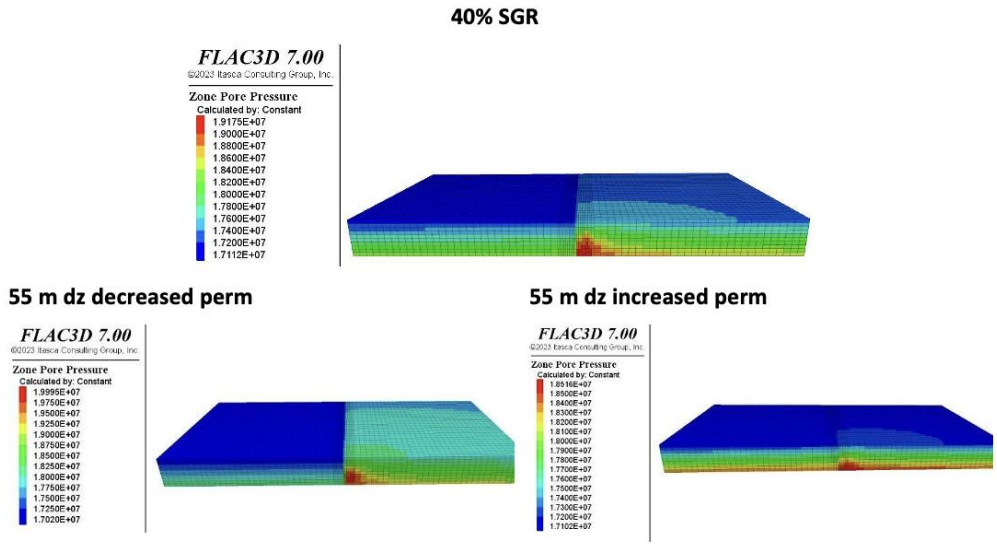

Figure 48. FLAC3D model results which compare the effect on the pore pressure of the reservoir on the 40% SGR model scenario with decreasing and decreasing permeability in the damage zone.

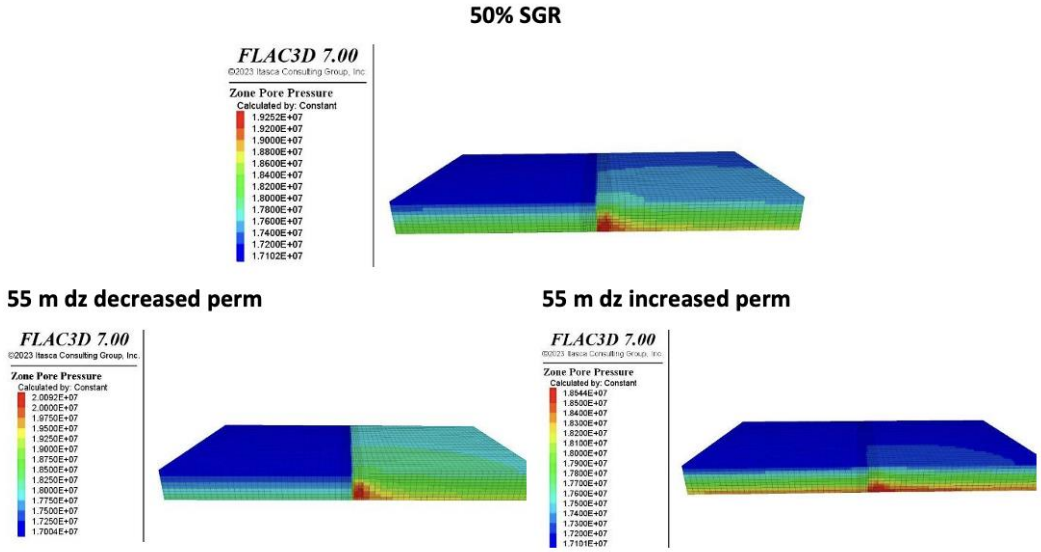

Figure 49. FLAC3D model results which compare the effect on the pore pressure of the reservoir on the 50% SGR model scenario with decreasing and decreasing permeability in the damage zone.

For the post – processing results of the FLAC3D – ToughREACT model software the results were analyzed in two planes (Fig. 50), x=0 and y=0.

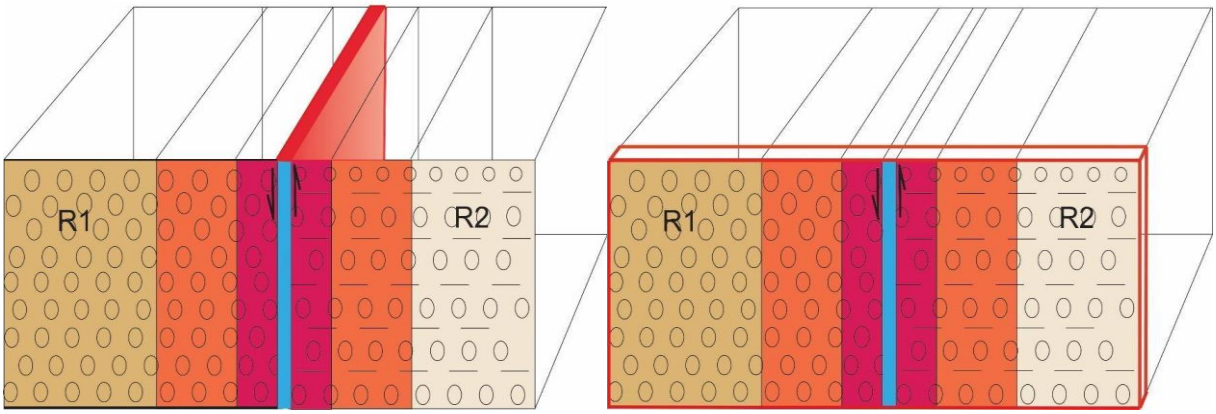

Figure 50. The planes that the post – process results of the FLAC3D – ToughREACT model were analyzed, x=0 for along the fault in the left-hand image and y=0 for the results that correspond to cross – section for the right-hand image.

Base case (no damage zone width)

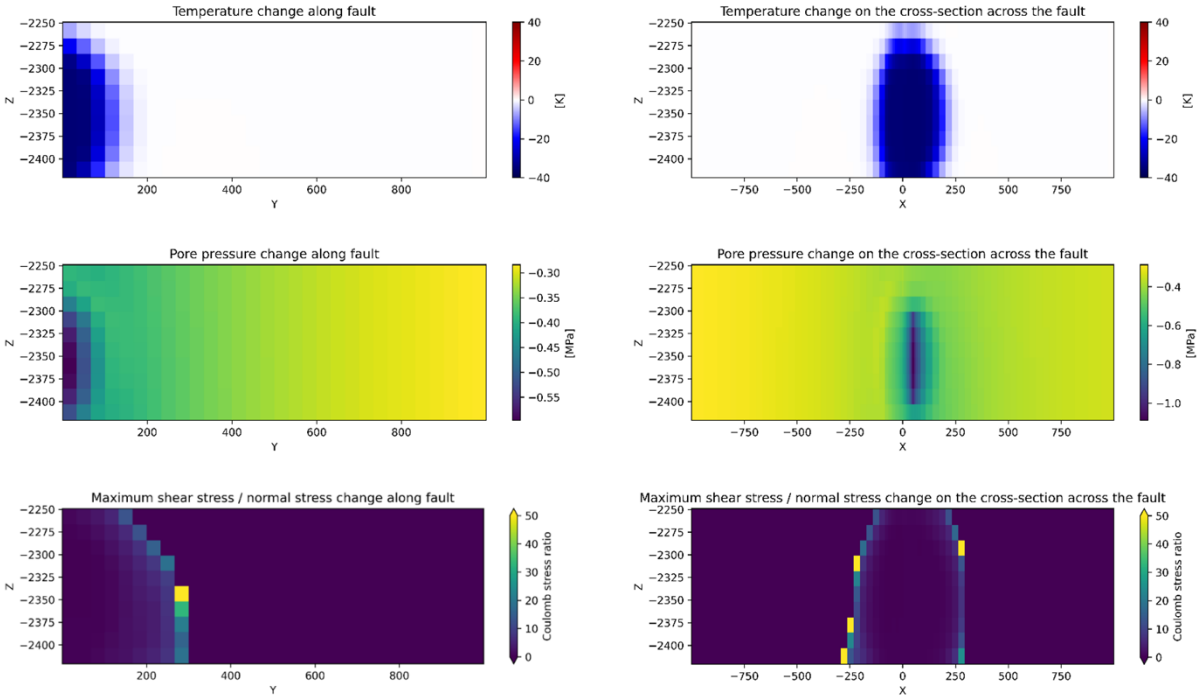

Figure 51. Base case results (0% SGR in the fault core and no damage zone width) on temperature, pore pressure and stress distribution along the fault (x=0) and in cross – section (y=0).

0% SGR 55m dz decreased perm

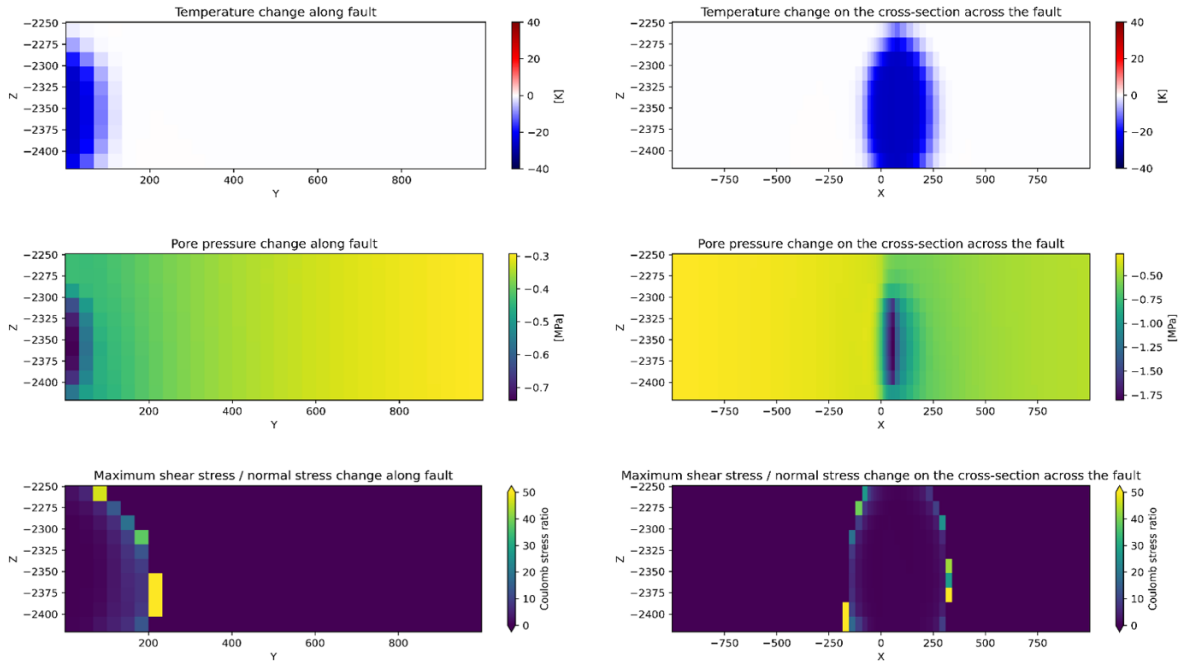

Figure 52. Results for 0% SGR in the fault core with decreased permeability within the damage zone on temperature, pore pressure and stress distribution along the fault (x=0) and in cross – section (y=0).

0% SGR 55m dz increased perm

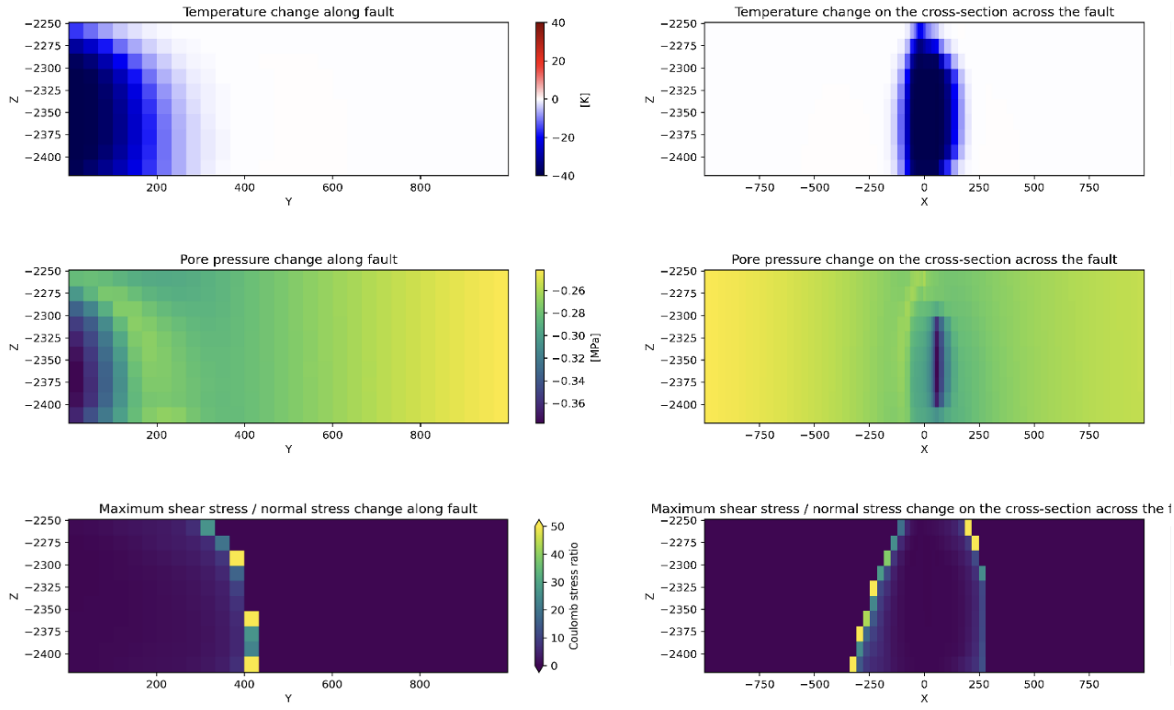

Figure 53. Results for 0% SGR in the fault core with increased permeability within the damage zone on temperature, pore pressure and stress distribution along the fault (x=0) and in cross – section (y=0).

40% SGR no width zone

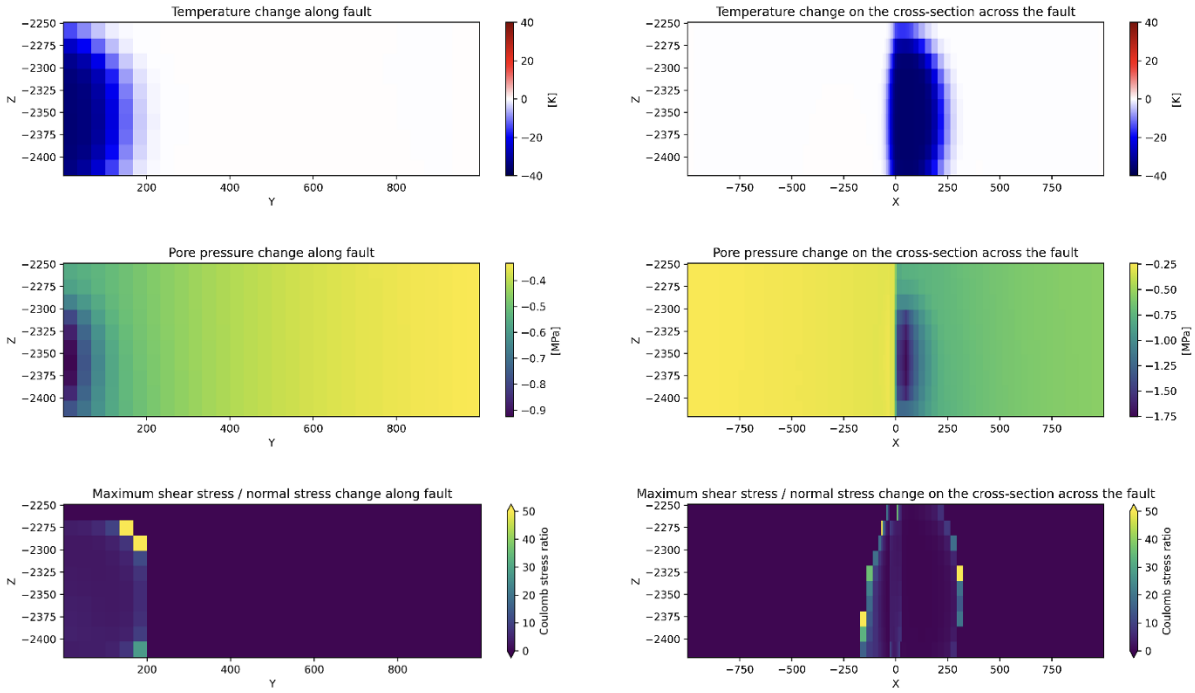

Figure 54. Results for 40% SGR in the fault core and no damage zone width on temperature, pore pressure and stress distribution along the fault (x=0) and in cross – section (y=0). (x=0) and in cross – section (y=0).

40% SGR 55m dz decreased perm

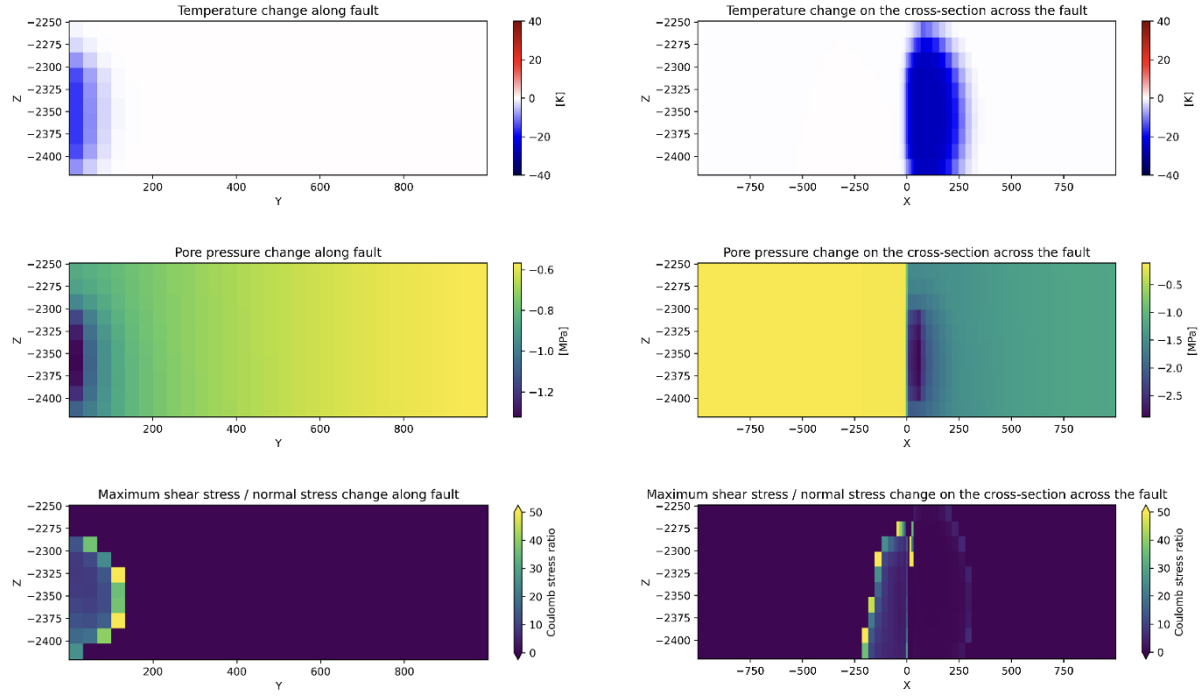

Figure 55. Results for 40% SGR in the fault core with decreased permeability within the damage zone on temperature, pore pressure and stress distribution along the fault (x=0) and in cross – section (y=0).

40% SGR 55m dz increased perm

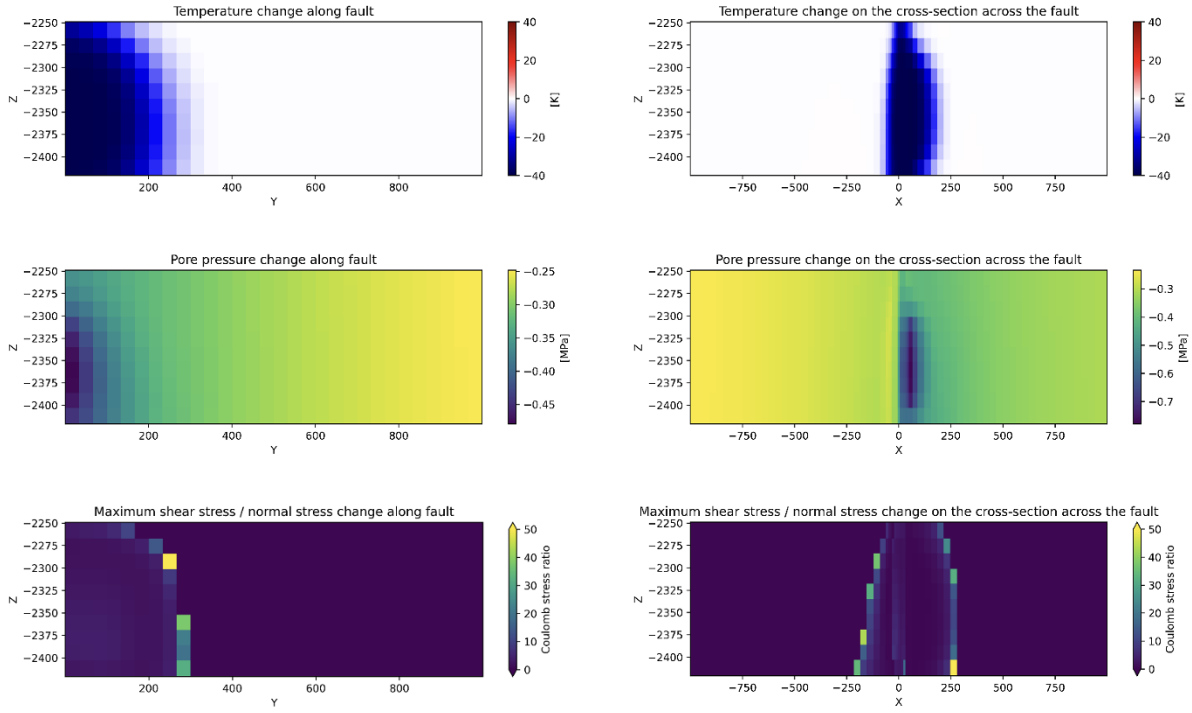

Figure 56. Results for 0% SGR in the fault core with increased permeability within the damage zone on temperature, pore pressure and stress distribution along the fault (x=0) and in cross – section (y=0).

50% SGR no width zone

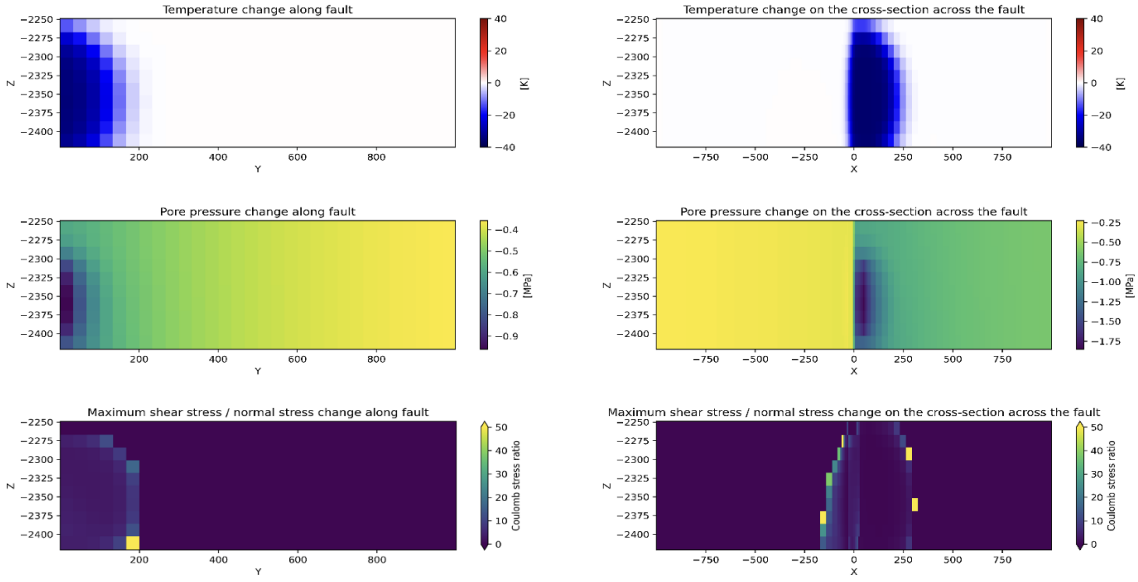

Figure 57. Results for 50% SGR in the fault core and no damage zone width on temperature, pore pressure and stress distribution along the fault (x=0) and in cross – section (y=0). (x=0) and in cross – section (y=0).

50% SGR 55m dz decreased perm

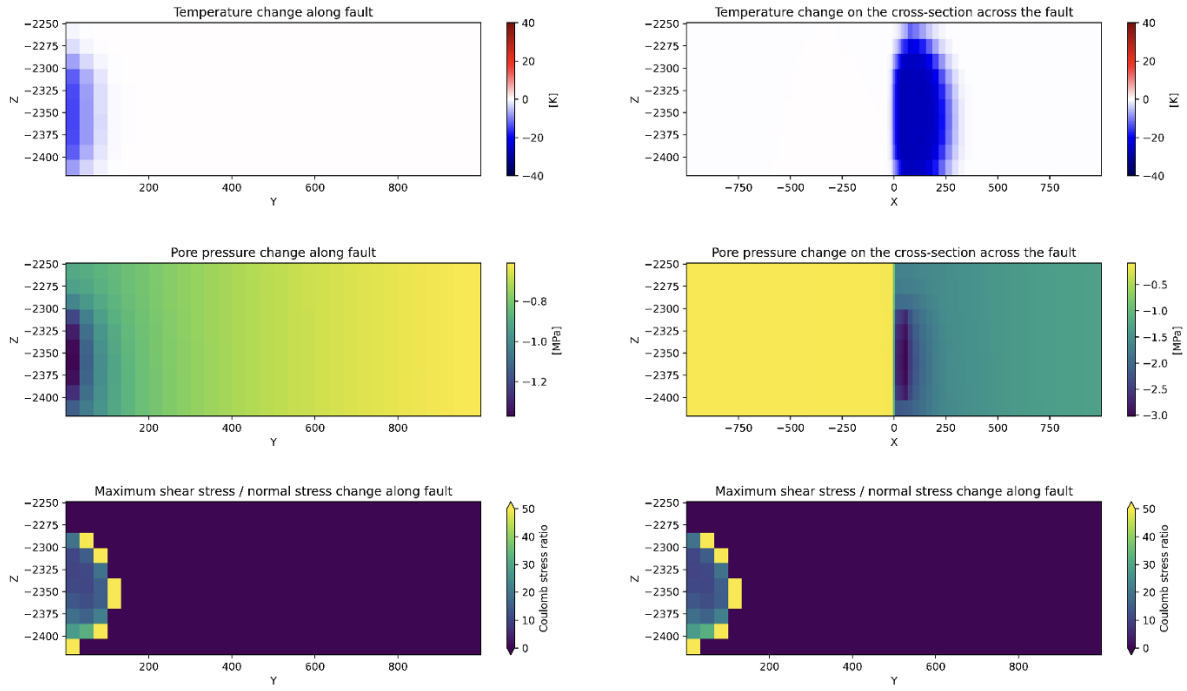

Figure 58. Results for 50% SGR in the fault core with decreased permeability within the damage zone on temperature, pore pressure and stress distribution along the fault (x=0) and in cross – section (y=0).

50% SGR 55m dz increased perm

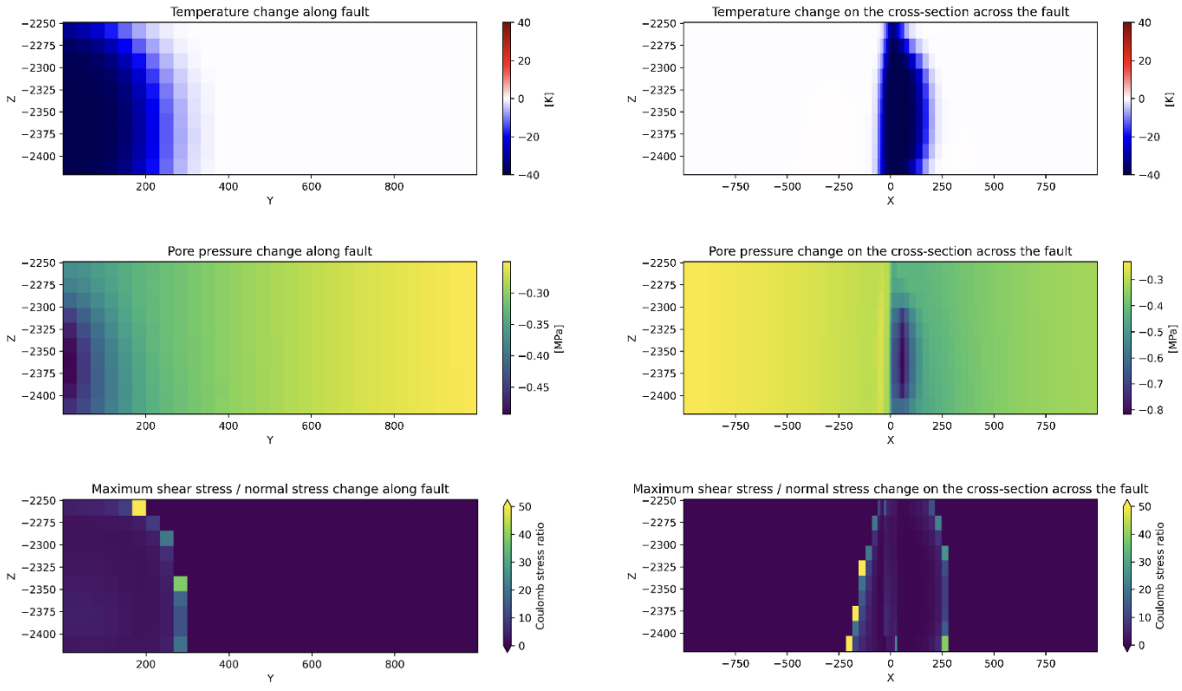

Figure 59. Results for 50% SGR in the fault core with increased permeability within the damage zone on temperature, pore pressure and stress distribution along the fault (x=0) and in cross – section (y=0).

60% SGR no width zone

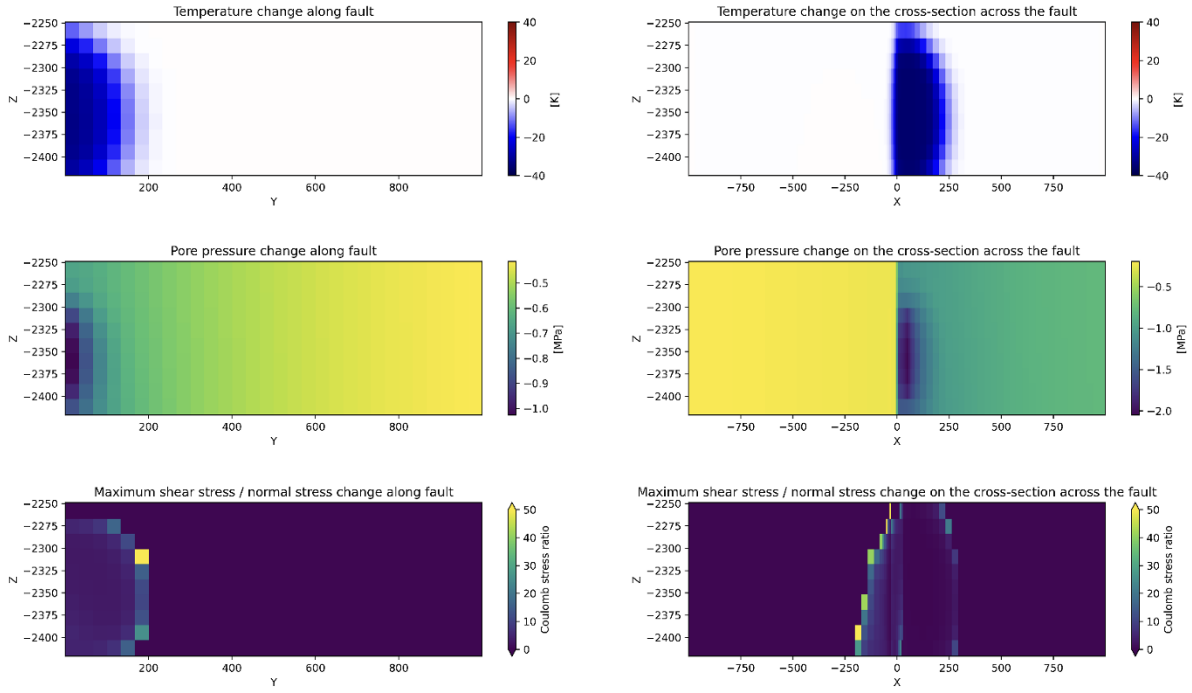

Figure 60. Results for 60% SGR in the fault core and no damage zone width on temperature, pore pressure and stress distribution along the fault (x=0) and in cross – section (y=0). (x=0) and in cross – section (y=0).

60% SGR 55m dz decreased perm

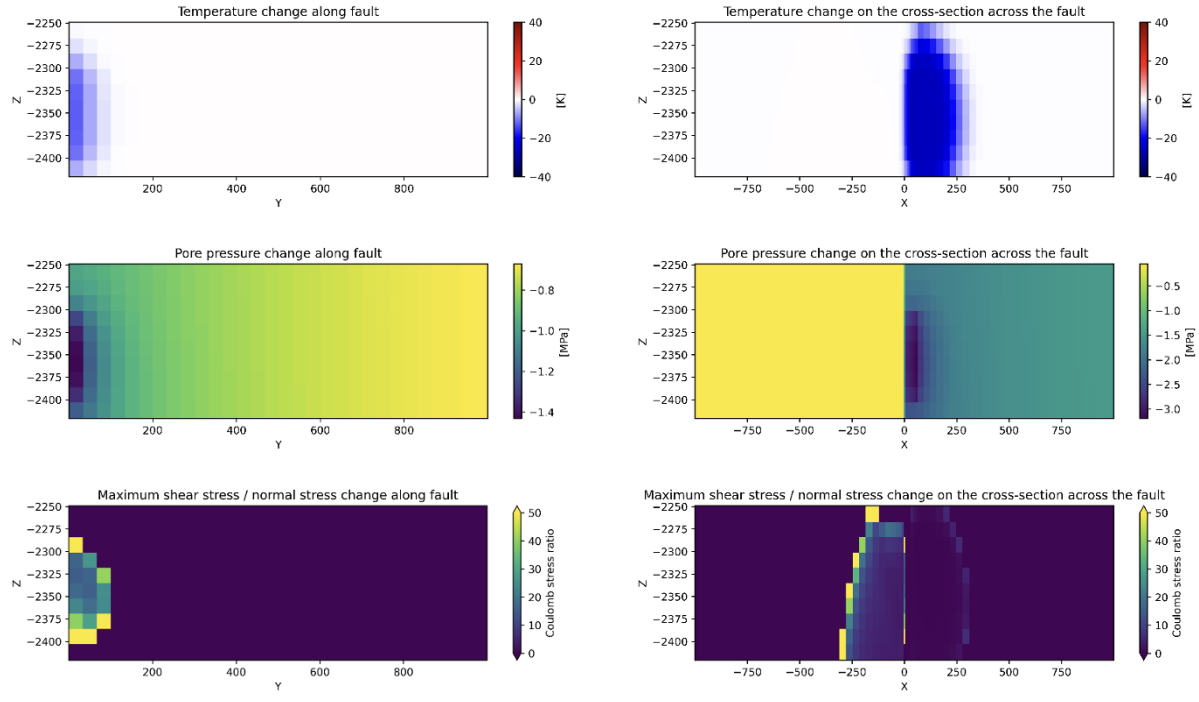

Figure 61. Results for 60% SGR in the fault core with decreased permeability within the damage zone on temperature, pore pressure and stress distribution along the fault (x=0) and in cross – section (y=0).

60% SGR 55m dz increased perm

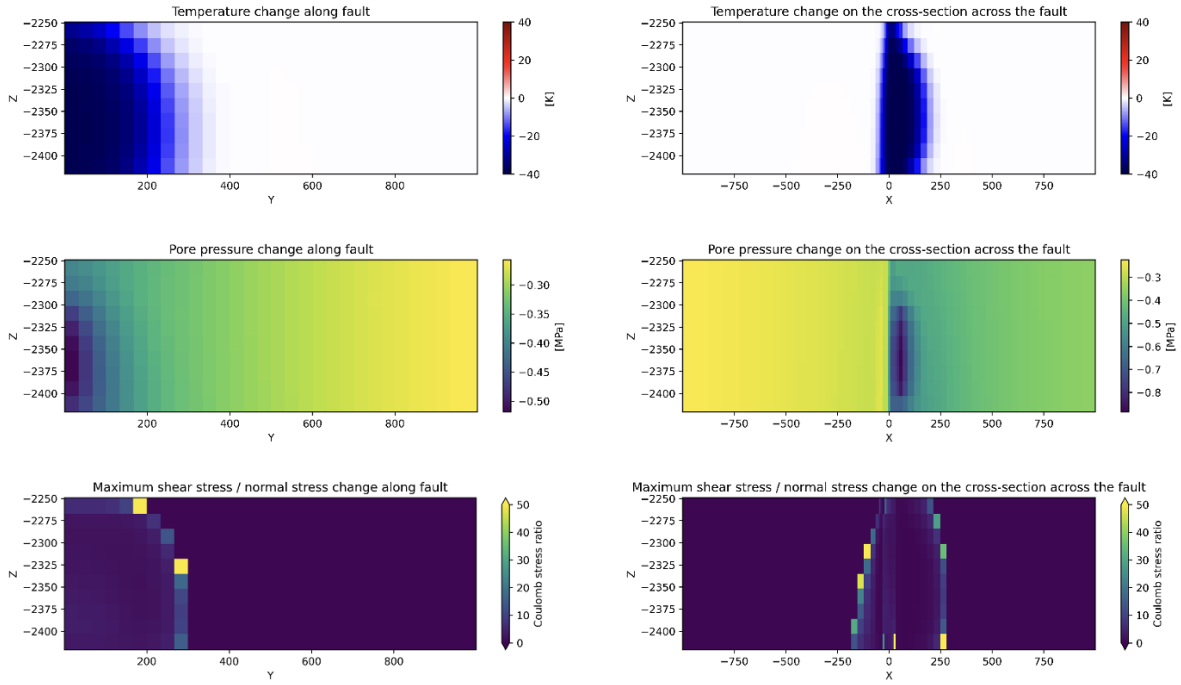

Figure 62. Results for 60% SGR in the fault core with increased permeability within the damage zone on temperature, pore pressure and stress distribution along the fault (x=0) and in cross – section (y=0).